Final Technical Report

Numerical Modeling of Oil Containment by a Boom/Barrier System : Phase II

Submitted to :

U.S. Department of Transportation
Attn : John Putukian
Volpe National Transportation Systems Center
55 Broadway, Cambridge, MA 02142-1093
DOT Grant No. DTRS57-95-G-00065

July 15, 1995-December 31, 1996

Submitted by :
S. T. Grilli, Z. Hu, M.L. Spaulding, and D. Liang

Department of Ocean Engineering
University of Rhode Island Narragansett Bay Campus
Narragansett, RI 02882

March 31, 1997

Contents

Abstract

This report presents results obtained at the University of Rhode Island, Department of Ocean Engineering, as part of a research project entitled : "Numerical Modeling of Oil Containment by a Boom/Barrier System : Phase II". This project was supported by Grant No. DTRS57-95-G-00065 of the Department of Transportation (DOT) (United States Coast Guards District (USCG) No. 1) FY 1995 Oil Pollution Research Grant Program. A 50% budget match was provided by the University of Rhode Island.

This project started on July 15, 1995, originally for a period of one year, but was subsequently extended until December 31, 1996. The Phase II project is a second year continuation of a Phase I project entitled : "A hydrodynamic model of oil containment by a boom", which was supported by DOT-USCG Grant No. DTRS-5794-G-00076 of the Department of Transportation FY 1994 Oil Pollution Research Grant Program. A third year continuation grant for Phase III of this project has been awarded as of January 1, 1997, under funding from the Minerals Management Service (MMS). The present report only covers developments and computations carried out during Phase II of the project, using a numerical model hereafter referred to as the *Phase II model*.

The long term goal of these studies is to develop computer models that will help both gain fundamental insight into oil containment failure mechanisms and outline strategies and methods for limiting the occurrence and/or the intensity of these failures, in actual field situations.

Following initial studies and model developments reported for Phase I studies (Grilli *et al.* [16]), model developments in Phase II studies have focused on three major aspects : (i) improving and complementing the models developed in Phase I, namely both periodic and non-periodic Piecewise Constant Vortex Sheet (PCVS) models; (ii) provide a better representation of hydrodynamic instabilities in the oil containment problem by developing and implementing a more accurate model based on Continuous Vortex Sheets (CVS); and (iii) both implementing and validating a numerical method for calculating the quasi-steady equilibrium shape of an oil-slick including the effects of interfacial friction, and developing a formalism to include interfacial friction effects in the Vortex Sheets (VS) time updating equations (which were ignored in Phase I model).

As a result of such model development/improvements, model applications carried out during Phase II provide more quantitative analyses and predictions than the qualitative descriptions of the oil containment behavior achieved during Phase I.

More specifically, in Chapter 1, we present an overview of the project as of the end of Phase II and, in Chapter 2, we present the PCVS models equations and applications. Looking at Figs. 2.13, 2.14, and 2.15, for instance, it can be seen that both entrainment and critical accumulation failure modes have been well qualitatively modeled using the PCVS approach. In Chapter 3, we present development and application of the new CVS model. Looking at Fig. 3.3, for instance, it can be seen that the periodic Kelvin-Helmholtz instability at an oil-water interface, and the subsequent roll-up of Vortex Sheets, have been very accurately modeled, and for a much longer time, than using the PCVS model. In

Chapter 4, we present a model and applications for calculating the quasi-steady-state initial shape of a contained oil slick. Looking at Fig. 4.3, for instance, it can be seen that the initial stable shape of an oil slick, measured by Milgram and Van Houten [29] in their laboratory experiments, was correctly recalculated using the PCVS model. Finally, in Chapter 5, we give the modified vorticity updating equations (5.20) and (5.21), including the effects of interfacial friction. These equations will be implemented and tested during Phase III studies.

Chapter 1

Introduction and project overview

1.1 Introduction

This report presents results obtained at the University of Rhode Island, Department of Ocean Engineering, as part of a research project entitled : *Numerical Modeling of Oil Containment by a Boom/Barrier System : Phase II*, which was funded by the U.S. Coast Guard (USCG) as part of the FY95 budget of the "Oil Pollution Research Grant Program" The present project is a continuation of a Phase I project : *A hydrodynamic model of oil containment by a boom : Phase I*, which was also funded by the U.S. Coast Guard (USCG), as part of the FY94 budget of the same program.

The Phase I project was aimed at developing a two-dimensional hydrodynamic model of *oil containment* by booms, to be used to investigate oil containment failure (Figs. 1.1 and 1.2). It was envisioned that this numerical model and its future improvements would help us both gain fundamental insight into oil containment failure mechanisms and outline strategies and methods for limiting the occurrence or the intensity of these failures, in actual field situations. Due to its more catastrophic nature, the failure mode referred to as *critical accumulation* was the main object of the study (Figs. 1.2, 1.3). Three main technical tasks were initially proposed : (i) numerical model selection and design; (ii) model testing and validation; and (iii) application to oil containment failure. Extensive literature review and analysis of the physical, theoretical, and numerical problems relative to oil containment were conducted as part of task (i) (Grilli *et al.* [16]). Based on this review, an initial modeling strategy was selected (hereafter referred to as the *Phase I model*). The Phase I model was implemented and validated, and used to predict oil containment failure, as part of tasks (ii) and (iii). In all cases, model results qualitatively showed the expected failure modes and the correct sensitivity to changes in physical parameters (e.g., Fig. 1.4). Details of the Phase I model development, implementation, and results can be found in Grilli *et al.* [16, 17].

The Phase II project involved various improvements of the Phase I model, hereafter referred to as the *Phase II models*, at both the level of the modeled physics (e.g., inclusion of friction effects at the oil-water interface) and the numerical methods used (e.g., higher-

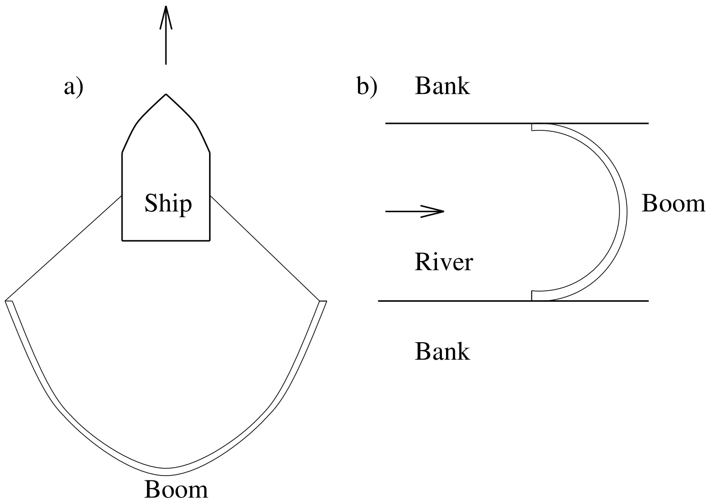

Figure 1.1: Planview of typical set-up for oil containment by : (a) a towed boom (ocean); or (b) a static boom (river). Arrows mark the direction and magnitude of the relative velocity U between boom and water.

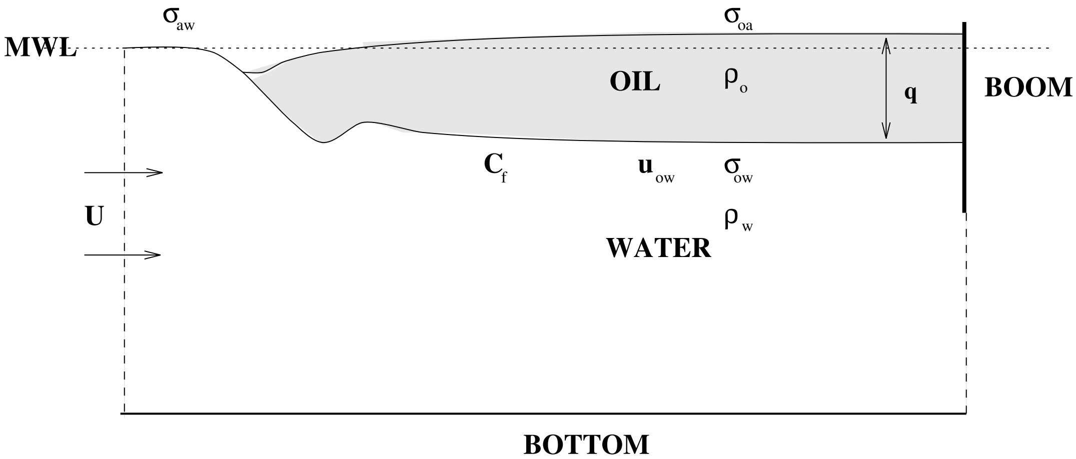

Figure 1.2: Sketch for initiation of oil containment failure by *critical accumulation*, with mention of important parameters : U, water-boom relative current velocity; $\mathbf{u}_{ow}$, oil-water relative velocity; ρ_o, ρ_w, oil and water density, respectively; σ_{ow}, σ_{oa}, σ_{aw}, interfacial tension coefficients for oil-water, oil-air, and air-water, respectively; C_f, oil-water interfacial friction coefficient; q, oil slick depth; MWL, Mean Water Level.

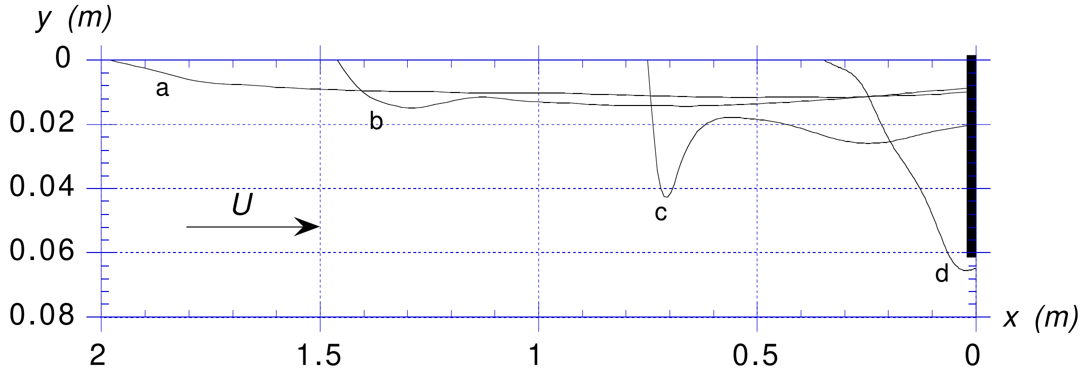

Figure 1.3: Experimental shapes of oil slicks measured in Delvigne's [9] experiments with Arabian light emulsion ($\nu_o = 2,300$ cs) for relative water-boom velocity U = a : 0.065; b : 0.095; c : 0.128; and d : 0.145 m/s. The figure shows the increase in size of the headwave and the shortening of the slick as U increases from curve a to c and, finally, the failure by *critical accumulation* with the oil slick draining under the boom in curve d.

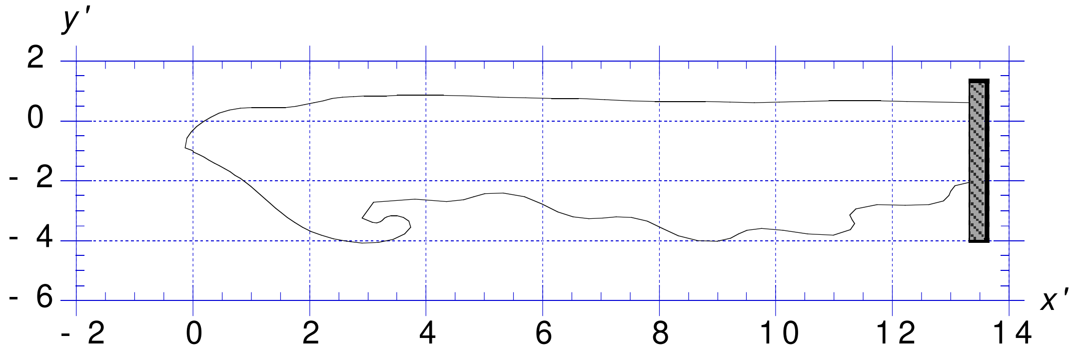

Figure 1.4: Illustration of (qualitative) computations with the Phase I model for an oil slick contained by a boom. In this case, both a headwave and interfacial instabilities develop simultaneously.

order discretization and time updating techniques). More specifically, model developments in Phase II studies focused on three major aspects :

(i) improving the Piecewise Constant Vortex Sheet (PCVS) models, both periodic and non-periodic, developed during Phase I studies; for the non-periodic PCVS model, in particular, improvements were aimed at better addressing problems with complex boundary geometries (as needed to correctly include booms in VS models);

(ii) developing and implementing a more accurate higher-order model, based on Continuous Vortex Sheets (CVS), which will ultimately provide a better representation of hydrodynamic instabilities in the oil containment problem; and

(iii) both implementing and validating a numerical method for calculating the quasi-steady equilibrium shape of an oil-slick including the effects of interfacial friction, and developing a formalism to include interfacial friction effects in the Vortex Sheets (VS) time updating equations. [These were ignored in Phase I model.]

As a result of such model development/improvements, Phase II model applications presented in this report provide more quantitative predictions of the oil behavior than the qualitative description achieved during Phase I studies. In particular, using the periodic PCVS (Phase II) model, a wide parametric study of periodic interfacial instability was conducted, where values of important parameters such as oil density, surface tension, and oil-water velocity, were varied (Section 2.5.2). The modeling of oil containment by a boom using the non-periodic PCVS (Phase II) model provided more physically sound results than obtained using the Phase I model (Section 2.5.2). Application of the new periodic CVS model to the KH instability problem predicted interface VS roll-up, much further in time than in any other earlier published numerical study of this problem (Section 3.3). Finally, the calculation of the equilibrium quasi-steady shape of an oil slick showed surprisingly good agreement with experimental measurements (Section 4.6).

Despite their accuracy and relevance, the main drawbacks of the numerical models developed so far, however, are that, except for the computation of the equilibrium quasi-steady shape of a slick, there has been no comparison (and thus calibration) of the time dependent models with experimental results and that the models have assumed no surface waves. Such experimental validation and calibration will be conducted as part of the ongoing Phase III of the project, by comparing model results with experimental data obtained in the University of New Hampshire's two-dimensional flume and three-dimensional data obtained at MMS's OHMSETT flume in New Jersey.

In Chapter 1 of this report, we present key elements of the oil containment modeling problem. In Chapter 2, we present equations and results for both periodic and non-periodic improved PCVS models and, in Chapter 3, we present the same for the new CVS periodic model. In Chapter 4, we present a model and applications for calculating the quasi steady-state shape of an oil slick, including interfacial friction effects; and in Chapter 5, we give the modified vorticity updating equations including the effects of interfacial friction.

1.2 Project Overview

Booms are one of the most commonly used techniques to collect and contain oil on the sea surface, or to protect specific areas against slick spreading by containment or diversion. In the collection mode, floating boom systems are deployed on the free surface, usually in U or V configurations, and towed towards the oil slick. In the diversion mode, they are used to direct oil to the shoreline or sheltered area.

The containment of oil by a boom is illustrated by the sketches in Fig. 1.1 which correspond to both an *ocean situation* in which a boom is towed by a boat at relative speed U over the water, and a *river situation* in which a fixed boom is placed across a river flow with current U. In both cases, oil accumulates inside the boom with the maximum accumulation occurring at the boom catenary's apex, where the maximum relative water velocity also occurs. Considering the location of accumulation and the small curvature of the boom geometry around the apex point, it is often acceptable (as a first approximation) to simplify this essentially three-dimensional problem to a *two-dimensional* one in the vertical plane intersecting the boom's apex (Fig. 1.2). It is also reasonable to assume that, for both cases in Fig. 1.1, the boom does not move and the water flows under the boom at a velocity U, equal to the relative boom-water velocity.

In order to collect as much oil as possible in the shortest possible time, it is desirable to have a relative velocity as large as possible. Various hydrodynamic instabilities at the oil–water interface, however, contribute to a fairly low practical limit for the relative velocity, on the order of 0.5 m/s. In fact, for the idealized problem sketched in Fig. 1.2, laboratory observations show that interfacial waves start developing at the oil–water interface for relative current speeds, $U \simeq 0.15$ m/s. For larger speeds, these waves grow unstable and, in most cases, lead to substantial or even total loss of oil under the boom (Agrawal and Hale [1], Lau and Kirchifer [27], Wicks [39], Wilkinson [40, 41]).

In the literature, such instabilities are referred to as *boom containment failure modes* and three main types (or modes) of containment failures have thus far been identified [1] :

- *drainage failure*, where an increase in relative water-boom velocity U leads to an increase in interfacial friction stresses, causing both a shortening and a thickening of the slick beyond the barrier draft d, leading to containment failure;
- *entrainment failure*, where, for high relative oil–water velocities and low viscosity oils ($\nu_o < 3,000$ cs), large interfacial stresses occur and induce shear instabilities at the oil-water interface characterized by the formation of small fast-moving interfacial waves (ripples); for sufficiently large U (on the order of 0.25 m/s), these waves may grow unstable and break, leading to subsequent entrainment of oil droplets in the underlying flow;

[1] Note that, in addition to these failure modes which occur in calm weather, the effectiveness of the boom in containing oil can be severely limited by the hydrodynamic behavior of both the boom and the slick under extreme weather conditions that may create high seas. Such factors have not been considered in the Phase I and II studies.

- *critical accumulation*, where, for oils with large viscosities ($\nu_o \geq 3,000$ cs) and velocity U usually lower than for the other two modes ($U_{cr} \simeq 0.15$ m/s), the interface develops slow-moving larger scale oscillations (headwave) which eventually cause all of the oil to escape under the barrier, *independent* of barrier draft d (Fig. 1.3).

Grilli *et al.* [16] conducted an exhaustive literature review of the oil containment problem and identified the key parameters and physical phenomena governing the three failure modes listed above. They showed, in particular, that *critical accumulation* is the dominant failure mode for high viscosity oils that are found in many real slicks [2] (Delvigne [9], Johnston *et al.* [22]). They also clearly showed that interfacial waves occurring during entrainment and critical accumulation failure modes are both initiated and sustained by *shear instability* at the oil-water interface, usually referred to as a *Kelvin-Helmholtz (KH) instability* (Benjamin [5], Drazin [11], Jones [23], Rangel and Sirignano [33]). Based on these findings, Grilli *et al.* focused on numerical modeling of KH instability (in the context of oil containment by a boom) as the main objective for Phases I and II of this project.

KH instabilities at the oil-water interface result from the interplay of the following physical processes and parameters (Fig. 1.2),

- the relative *water-boom velocity* U, which controls the magnitude of interfacial friction forces and triggers and sustains KH instability (see Section 2.5.2);
- the fluid *density difference* $\Delta\rho_{ow} = \rho_w - \rho_o$, which affects both slick thickness and spreading forces. [In applications, this parameter is often represented by the value of the oil/water density ration $\varphi = \rho_o/\rho_w = 1 - \Delta\rho_{ow}/\rho_w$.] (see Chapter 4);
- $\Delta\rho_{ow}$ and the *surface tension* coefficient at the oil water interface, σ_{ow}, which both affect the growth of interfacial KH waves (see Section 2.5.2);
- the interfacial *friction coefficient* C_f, which controls the magnitude of interfacial friction forces (and thus affects oil slick thickness) and is dependent on interfacial shape (including irregularities due to KH waves) (see Chapter 4);
- *oil viscosity* ν_o, which damps out short interfacial waves and limits the strength of internal circulation cells within the oil slick (hence justifying a quasi-hydrostatic assumption for highly viscous oil slicks; see Chapter 4).

Other parameters of lesser importance are σ_{aw} and σ_{oa}, the air-water and oil-air surface tension, respectively.

Many experimental and theoretical studies were pursued in the 1970's to understand the physics of oil containment by a boom and to identify the conditions leading to containment failure. More recently, there has been a renewed interest in studying this problem and attempts were made to use numerical modeling tools (Zalosh [42], Bai and Kim [2], Clavelle and Rowe [7], Ertekin and Sundararaghavan [13]). Among the existing models, however,

[2] Due to weathering effects, oil slick viscosity increases rapidly with time for many oils.

only the work by Zalosh [42] included the key parameters, listed above, affecting interfacial instability, whereas the other models [2, 7, 13] concentrated on representing fluid behavior in the bulk of the oil and water domains in front of and/or behind the boom, and totally ignored surface tension and KH waves on the oil–water interface.

In proposing the (FY94) Phase I project, considering the high degree of complexity of physical mechanisms involved, it was anticipated that the model would only be a first step towards a more comprehensive model of oil containment that could eventually provide practically useful results. In Phase I, we thus identified three major phases in model development, corresponding to successive improvements of the level of physical phenomena modeled and, hence, also of modeling accuracy (see Grilli *et al.* [16]). The approach selected for the initial model, *the Phase I model*, was based on Zalosh's model with both improved governing equations and numerical solution (see Grilli *et al.* [16]).

Development and implementation of the Phase II models took place as part of the FY95 project and are presented in this report. We will show that the Phase II models provide significant improvements of both the level of physics modeled and the numerical accuracy, compared to the Phase I model. In particular, we will present quantitative results showing the effects of the key factors listed above, on the growth rate of interfacial KH instabilities (Section 2.5.2). We will also give results of computations for the failure of a contained slick due to instabilities in the headwave (entrainment-type failures; Section 2.5.3). Finally, we will give quantitative predictions for the equilibrium steady-state shape of a contained slick, which compare favorably with experiments.

As a summary, Fig. 1.5 gives an overall flowchart for the model development procedures followed during Phase II, with the anticipated model experimental validation/calibration tasks to be carried out in the ongoing Phase III. As indicated in the figure, the major progress in Phase II models, as compared to the Phase I model, were made in the development of new numerical algorithms for the periodic (KH instability) and non-periodic (oil-slick with a boom) Piecewise Constant Vortex Sheet (PCVS) models, and in the establishment and implementation of a higher-order model (CVS) of the same problems. Numerical/qualitative validation of the newly developed models were carried out at all stages of model developments, using both convergence tests and lower-order theoretical solutions (e.g., the linearized KH instability problem by Lamb [26]). As indicated, both the PCVS and the CVS models and related algorithms were alternately tested for the KH instability case, which contains infinite vortex sheets with periodic disturbances, and for an oil-boom containment setting, similar to Fig. 1.2, which consists of multiple discretized vortex sheets and several infinite sheets.

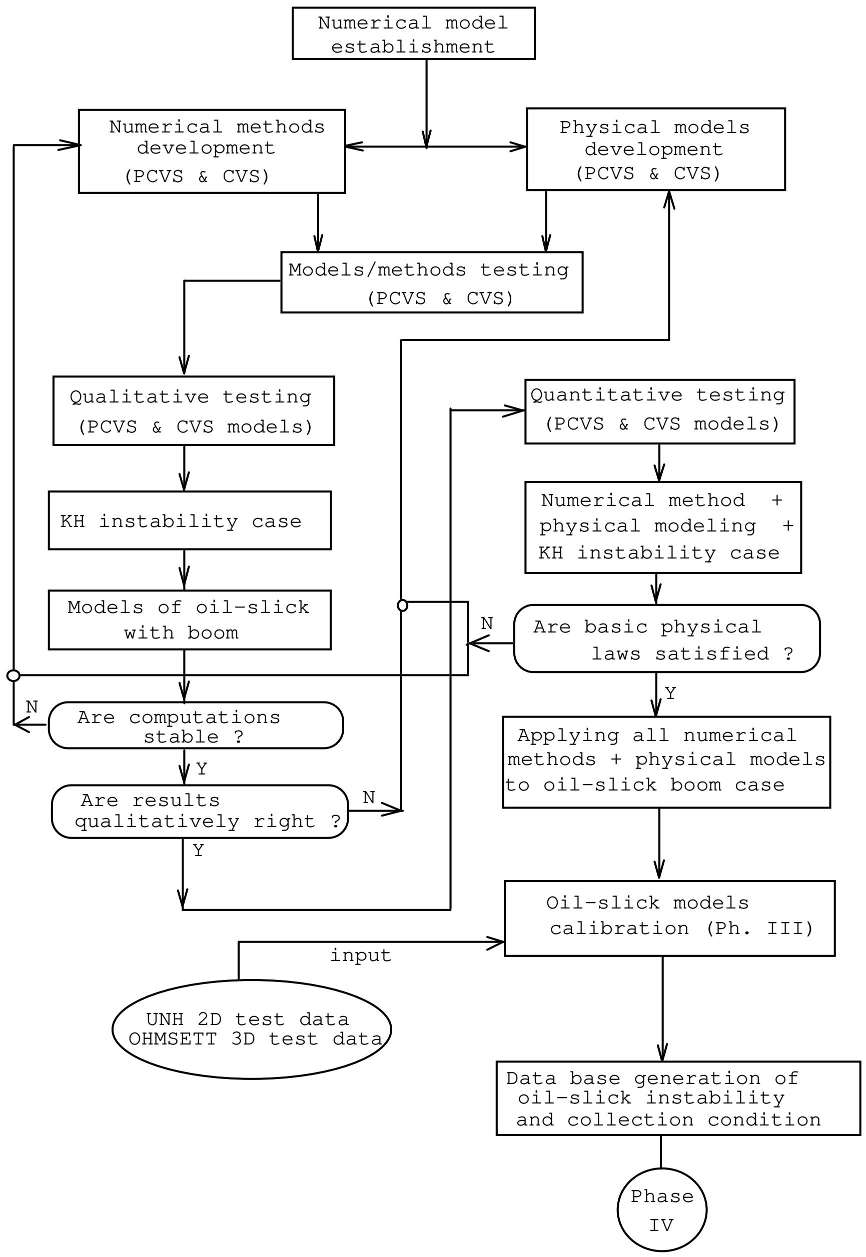

Figure 1.5: Flow chart of Phase II model development/validation procedure, with indication of Phase III validation/calibration tasks.

Chapter 2

Piecewise Constant Vortex Sheet (PCVS) model and applications

In the Phase I model developed for the containment of oil by a boom (e.g., Fig. 1.2), VS's were introduced to represent velocity discontinuity and geometry at fluid-fluid interfaces (air-water, air-oil, oil-water) and fluid-solid boundaries (boom, bottom). These VS's were discretized, along selected parts of the interfaces, using both piecewise-constant elements of vorticity (PCVS) and piecewise-polynomial geometry; semi-infinite parts of the interfaces were represented by semi-infinite VS's (Fig. 2.1).

This PCVS approach to the oil containment problem was further developed and refined during Phase II. In this Chapter, we first give a recapitulation of general VS dynamics equations (Section 2.1) and both old (Phase I) and newly developed (Phase II) improved numerical procedures (Section 2.2) used in all the models. We then review the governing equations for the periodic PCVS model (Section 2.3) and give applications of the Phase II improved numerical model (Section 2.5.2). In Section 2.4, we detail the specific improvements made during Phase II to the non-periodic PCVS model and give applications to oil containment by a boom in Section 2.5.3.

2.1 Recapitulation of VS dynamics equations

2.1.1 Velocities induced by VS's

For an inviscid fluid flow in a vertical plane (x, y), when vorticity can be assumed to be concentrated within two-dimensional *vortex sheets* (VS), Biot-Savart's law can be used to calculate the induced velocity field, $\boldsymbol{u} = (u, v)$ as (Batchelor [4] p527),

$$
\begin{aligned}
u(x, y) &= \frac{1}{2\pi} \int \frac{y - y'}{r^2} \gamma(s)\, ds \\
v(x, y) &= -\frac{1}{2\pi} \int \frac{x - x'}{r^2} \gamma(s)\, ds
\end{aligned}
\tag{2.1}
$$

where $\gamma(s)$ is the *clockwise* vortex sheet strength (i.e., minus the vorticity) and $s(x', y')$ is the curvilinear abscissa at points $\boldsymbol{x}' = (x', y')$ along the sheet.

When points $\boldsymbol{x} = (x, y)$ do not belong to the VS, integrals in (2.1) are non-singular. For points (x, y) on the VS, integrals in (2.1) are singular for vanishing r and must thus be calculated in a Cauchy Principal Value (CPV) sense. In this case, (2.1) also takes the form of a Boundary Integral Equation (BIE) for $\boldsymbol{u}(x, y)$ on the sheet.

In the various numerical models developed in this study, discretized expressions of (2.1) are used to calculate the sheet position as a function of time, according to the Lagrangian definition of velocities, as,

$$\frac{d\boldsymbol{x}}{dt}(t) = \boldsymbol{u}(x, y) \tag{2.2}$$

where the time derivative follows the motion of the sheet.

A standard simplifying assumption in numerical models of VS dynamics is to assume that the vorticity is either *piecewise constant* or is concentrated at *point vortices* along the sheets. Despite their similarity—and sometimes their confusion in the literature—, these two representations differ in the sense that point vortices do not have a self-induced velocity contribution to Eqs. (2.1) whereas piecewise constant distributions of vortices do have self-induced velocity at the center of each interval, due to CPV integral contributions in (2.1) (Fink and Soh [14], Van de Vooren [37]).

In many studies, however, point vortices were found to only give a poor representation of continuous VS's as a function of time and often to quickly lead to inaccurate or even to unstable results. This occurs unless point vortices are continuously regridded to equal arc-length distance on the sheet (Fink and Soh [14]) and, even in this case, results cannot usually be accurately computed much beyond the initial instability and roll-up of the interface. The reason for this was discussed in Grilli *et al.* [16, 17] and various discretized equations and expressions for the CPV integrals needed for PCVS were given.

2.1.2 Rate of change of circulation on the VS's

For a vortex sheet representing the interface between two fluids moving with velocity $\boldsymbol{u}_o$ and $\boldsymbol{u}_1$, respectively, the VS strength (i.e., vorticity density) is given by [42, 43, 37, 33],

$$\gamma(s) = \Delta u_s = u_{os} - u_{1s} \tag{2.3}$$

in which,

$$u_{os} = \boldsymbol{u}_o \cdot \boldsymbol{s} \quad ; \quad u_{1s} = \boldsymbol{u}_1 \cdot \boldsymbol{s} \tag{2.4}$$

are tangential velocities on both sides of the VS, with $\boldsymbol{s} = [\cos\beta, \sin\beta]$, the tangential vector along the sheet and $\beta(s)$ the angle between the tangent to the sheet and the x-axis.

Using (2.3), the circulation (i.e., vorticity) associated with a small vortex element i of length Δs_i, over which constant velocity and smoothly varying geometry are assumed, is given by,

$$\Gamma(s_i) \equiv \Gamma_i = \int_{s_i - \Delta s_i/2}^{s_i + \Delta s_i/2} \gamma(s)\, ds \simeq (\, u_{os} - u_{1s}\,)_i\, \Delta s_i = \gamma_i \Delta s_i \tag{2.5}$$

For a uniform, incompressible, inviscid fluid with conservative forces, Kelvin's theorem states that the rate of change of circulation around a closed material contour moving with the fluid is zero (e.g., Batchelor [4]),

$$\frac{D\,\Gamma}{D\,t} = 0 \qquad \text{with} \qquad \frac{D}{D\,t} \equiv \frac{\partial}{\partial t} + \boldsymbol{u} \cdot \boldsymbol{\nabla} \tag{2.6}$$

where D/Dt denotes the material derivative. For a vortex sheet at the interface between two regions of different velocity within the same fluid, however, Van de Vooren [37] showed that Kelvin's theorem, as stated in (2.6), is not applicable but may only be applied for a contour moving with the sheet reference velocity equal to the mean between velocities on both sides of the sheet, $\boldsymbol{u} = \frac{1}{2}(\boldsymbol{u}_o + \boldsymbol{u}_1)$. This reference velocity is defined as the *sheet velocity* and will be used whenever calculating material time derivatives with respect to the sheet motion, referred to as d/dt.

For an interface between two different fluids with density ρ_o and ρ_1, subjected to gravity and non-zero interfacial tension σ_{o1}, the fluid is non-uniform and forces are non-conservatives. Hence the rate of change of circulation around a material contour crossing the interface is non-zero and an evolution equation must be developed to predict its behavior. Zaroodny and Greenberg [45] first derived an equation for the rate of change of circulation for a continuous vortex sheet without surface tension. Zalosh [42, 43] developed a similar equation, including surface tension effects, for a sheet discretized with point vortices but made an error when he failed to consider the difference mentioned above between the time derivatives D/Dt, following fluid particles on either side of the sheet, and d/dt, following the sheet motion. This was later pointed out by Rangel and Sirignano [33] who derived the correct evolution equation, but without including gravitational effects.

Grilli *et al.* [16, 17] derived the expression for the rate of change of circulation, including gravity, density difference, and surface tension effects at the interface between two fluids. For a vortex sheet with piecewise constant vorticity elements Δs_i's, it reads,

$$\frac{D\,\Gamma_i}{D\,t} = 2\Delta s_i \left(\kappa \left[\frac{du_{si}}{dt} + g\,\sin\beta_i + \frac{1}{4}\gamma_i \frac{\partial \gamma_i}{\partial s} \right] - \frac{\sigma'_{o1}}{1+\varphi}\,\frac{\partial^2 \beta_i}{\partial s^2} \right) \tag{2.7}$$

where $\sigma'_{o1} = \sigma_{o1}/\rho_1$, $\varphi = \rho_o/\rho_1 \leq 1$, $\kappa = (1-\varphi)/(1+\varphi)$ is the Atwood number and, by (2.4),

$$\frac{du_{si}}{dt} = \frac{du_i}{dt}\cos\beta_i + \frac{dv_i}{dt}\sin\beta_i \tag{2.8}$$

is the tangential acceleration at point i.

In computations, a characteristic length scale is defined as λ and a characteristic time scale as $\lambda/\Delta U$, in which ΔU denotes a characteristic velocity jump at the interface. Based on these, the following nondimensional variables are introduced for coordinates of vortex element centers, their arc-length, and the time, as,

$$\xi_i = \frac{x_i}{\lambda} \quad ; \quad \eta_i = \frac{y_i}{\lambda} \quad ; \quad \Delta \mathrm{s}_i = \frac{\Delta s_i}{\lambda} \quad ; \quad \tau = t\frac{\Delta U}{\lambda} \tag{2.9}$$

respectively, for the curvature at vortex element centers, as,

$$\mathrm{c}_i = \lambda \frac{\partial \beta}{\partial s} \tag{2.10}$$

for velocities at vortex elements centers, as,

$$\mathrm{u}_i = \frac{u_i}{\Delta U} \qquad ; \quad \mathrm{v}_i = \frac{v_i}{\Delta U} \tag{2.11}$$

and for the vorticity of vortex elements, as,

$$\mathrm{g}_i = \frac{\Gamma_i}{\lambda \Delta U} \tag{2.12}$$

With these non-dimensional variables, the rate of change of vorticity of vortex elements can be expressed as,

$$\frac{d\,\mathrm{g}_i}{d\tau} = 2\Delta \mathrm{s}_i \left(\kappa \, [\, \frac{d\,\mathrm{u}_{is}}{d\tau} \, + \, \frac{\mathrm{g}_i}{4(\Delta \mathrm{s}_i)^2} \frac{\partial \mathrm{g}_i}{\partial \mathrm{s}} \,] \, + \, \mathbf{Fr}^{-2} \, \sin \beta_i \, - \, \mathbf{We}^{-1} \, \frac{\partial \mathrm{c}_i}{\partial \mathrm{s}} \right) \tag{2.13}$$

where **Fr** denotes the Froude number,

$$\mathbf{Fr} = \frac{\Delta U}{\sqrt{g \kappa \lambda}} \tag{2.14}$$

and **We** denotes the Weber number,

$$\mathbf{We} = \frac{\lambda \, (1 + \varphi) \, (\Delta U)^2}{\sigma'_{o1}} \tag{2.15}$$

The non-dimensional tangential acceleration at the interface in (2.13) is found as ($i = 1, ..., N$),

$$\frac{d\,\mathrm{u}_{is}}{d\tau} \; = \; \frac{d\,\mathrm{u}_i}{d\tau} \cos \beta_i + \frac{d\,\mathrm{v}_i}{d\tau} \sin \beta_i \tag{2.16}$$

Details can be found in Grilli *et al.* [16].

2.1.3 Semi-infinite vortex sheets

As in Zalosh [42], horizontal semi-infinite vortex sheets will be used in the (non-periodic) computations of oil slick containment by a boom, to represent regions of the water domain with constant uniform horizontal velocity U. In Fig. 2.1, for instance, this corresponds to free surface and bottom regions both in front of the slick (e.g., from $x = -\infty$ to $x = x_\ell$) and behind the boom (e.g., from $x = x_r$ to $x = +\infty$).

Assuming no air velocity and no flow through the bottom, these semi-infinite sheets have a tangential velocity jump $\Delta u_s = \pm U$, with the negative sign being taken on the free surface and the positive sign on the bottom.

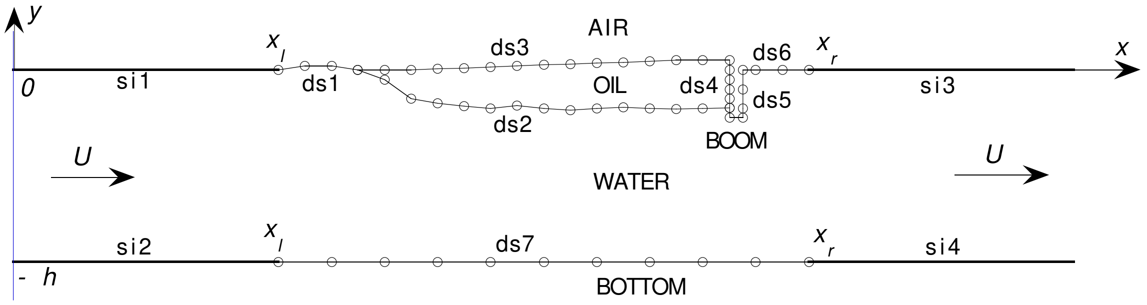

Figure 2.1: Sketch of computational domain for the oil containment by a boom, with definition of main parameters : U = flow velocity; si1-si4 = semi-infinite vortex sheets; ds1-ds7 = piecewise-constant discretized vortex sheets; $\circ$ = centers of discretized vortex elements.

When parts of the fluid domain are discretized with VS elements, such semi-infinite vortex sheets provide contributions to the discretized form of Biot-Savart's Eqs. (2.1) for the sheet velocity, and also to the VS's accelerations. These contributions were calculated by Grilli *et al.* [16]. For instance, if the unperturbed free surface is at $y = 0$ and the horizontal bottom is at $y = -h$, the total contribution to the velocity of four semi-infinite vortex sheets located at $(x_\ell, 0)$ and $(x_r, 0)$, with strength $-U$, and at $(x_\ell, -h)$ and $(x_r, -h)$, with strength $+U$ is calculated as,

$$
\begin{aligned}
u_{\ell r} &= \frac{U}{2\pi}\{2\pi + \arctan(\frac{x - x_\ell}{y}) - \arctan(\frac{x - x_\ell}{y + h}) - \arctan(\frac{x - x_r}{y}) \\
&\quad + \arctan(\frac{x - x_r}{y + h})\} \\
v_{\ell r} &= \frac{U}{4\pi} \log \frac{[(x - x_r)^2 + y^2]\,[(x - x_\ell)^2 + (y + h)^2]}{[(x - x_\ell)^2 + y^2]\,[(x - x_r)^2 + (y + h)^2]} \qquad (2.17)
\end{aligned}
$$

As a verification, if we take $x_\ell = x_r$ in Eq. (2.17), thus assuming a uniform flow represented by two infinite vortex sheets, we see that (2.17) indeed reduces to, $u_{\ell r} = U$ and $v_{\ell r} = 0$.

For the accelerations it could be shown, similarly, that all contributions from the four sheets, as expected for a uniform flow, cancel each other and we get, $du_{\ell r}/dt = dv_{\ell r}/dt = 0$.

2.2 General numerical procedures for PCVS model

Numerical methods were developed in Phase I model for the integration of Eqs. (2.1) and (2.2). These were essentially a numerical integration of the BS equations and a time stepping procedure for the time marching. The basis of these methods have been kept in the Phase II model.

The differential equation (2.2) is solved using an explicit time stepping method in which both the geometry and the circulation on the VS's are calculated at time $\tau + \Delta\tau$, from the known geometry and vorticity at time τ, using a truncated Taylor series as ($i = 1, ..., N$),

$$\begin{aligned}
\xi_i(\tau + \Delta\tau) &= \xi_i(\tau) + \Delta\tau\, \mathrm{u}_i(\tau) + \frac{(\Delta\tau)^2}{2}\frac{d\mathrm{u}_i}{d\tau}(\tau) + \mathcal{O}[(\Delta\tau)^3] \\
\eta_i(\tau + \Delta\tau) &= \eta_i(\tau) + \Delta\tau\, \mathrm{v}_i(\tau) + \frac{(\Delta\tau)^2}{2}\frac{d\mathrm{v}_i}{d\tau}(\tau) + \mathcal{O}[(\Delta\tau)^3] \\
\mathrm{g}_i(\tau + \Delta\tau) &= \mathrm{g}_i(\tau) + \Delta\tau\frac{d\mathrm{g}_i}{d\tau}(\tau) + \frac{(\Delta\tau)^2}{2}\frac{d^2\mathrm{g}_i}{d\tau^2}(\tau) + \mathcal{O}[(\Delta\tau)^3] \qquad (2.18)
\end{aligned}$$

where $\Delta\tau$ denotes the nondimensional time step. Thus, starting with the VS's initial geometry and circulation, the induced velocity components u_i and v_i are calculated along the sheets using BS equations (2.1), discretized using PCVS elements. [The discretized BS equations for both periodic and non-periodic PCVS models are given in Sections 2.3.2 and 2.4.2.] Corresponding accelerations $(d\mathrm{u}_i/d\tau, d\mathrm{v}_i/d\tau)$ are calculated by finite backward differentiation. Time rates of change of circulation, $d\mathrm{g}_i/d\tau$, are then calculated using Eqs. (2.13)-(2.16), and $d^2\mathrm{g}_i/d\tau^2$ is calculated by finite backward differentiation (see Grilli *et al.* [16, 17] for details). Using these physical variables, Eq. (2.18) is used for the time updating and the whole process is repeated to calculate the solution at a later time.

Models developed during Phase I of this project, despite providing a good qualitative representation of the modeled phenomena, were not sufficiently accurate to allow good quantitative prediction. Furthermore, they were not usually stable enough to calculate interfacial evolution for a sufficiently long time. In the course of Phase II studies significant improvements were made to the models' numerical procedures to make computations both more accurate and stable. These improvements dealt with the following aspects of the computations :

- *Higher-order modeling of the geometry :* In Phase I model, higher-order sliding polynomial interpolation of the VS geometry was used. When using this method to compute interfacial evolution beyond the initial stages of instability (interfacial roll-up), however, it was observed that tangential derivatives became very irregular in regions of large curvature. This, in turn, through the effects of curvature and surface tension in the vorticity updating Eq. (2.13), caused the numerical results to rapidly become unreliable. The source of these irregularities was identified during Phase II studies as resulting from the isoparametric element mapping used in the sliding interpolation. A new interpolation/mapping method was developed that eliminated these irregularities. This method is referred to as *parity mapping* method.

  To our knowledge, the origin of such irregularity problems has never been identified in earlier published studies of interfacial instabilities and may be responsible for some of the unstable results obtained by some authors, and referred to as *numerical chaos*, when using PCVS or point vortex methods to compute the roll-up of interfaces.

  The parity mapping method is detailed in a following section.

- *End point periodicity and compatibility :* In the periodic KH problem (see below), the exact mathematical transformation of the infinite interface into a periodic interface in the model both requires that the wavelength λ of periodicity be maintained closely constant and that numerical results be strictly periodic for each extremity of the discretized sheet. In the PCVS method, however, the use of the centers of constant segments as discretization points requires that both the first and last such segments be extended by half their length to represent a full wavelength. All geometrical quantities and their derivatives must also satisfy this periodicity. Although partly enforced in the Phase I model, these requirements were not all fully satisfied in the equations. Results were thus slightly less accurate for the end nodes of the interface which, through time stepping, could lead to significant errors and sometimes to the termination of computations, due to numerical sawtooth instability, before roll-up could be completed. Extended periodicity conditions have been implemented in the Phase II model for the periodic KH problem, and no irregular behavior is now observed at end nodes of the interface.

For the non-periodic oil-containment problem, VS's intersect each other at a number of locations (e.g., oil-water interface and boom, air-water interface and oil-water interface, etc...; see Fig. 2.1). At such multiple VS intersection points, components of the sheets' velocity calculated on different sheets must be compatible with each other, if the motion of the intersection point is to be uniquely defined, thus making computations stable. In the Phase I model, no particular attention was given to this problem and computations proved very unstable close to these "multiple points" which, in turn, had to be artificially maintained in their correct position. In the Phase II model, extended velocity/geometry compatibility conditions were implemented to ensure "multiple points" behaved correctly.

More details relative to "multiple points" modeling are given in a separate section.

- *Adaptive node regridding :* Regridding is a method where, through a re-interpolation of results on the interface between two fluids, nodes are redistributed according to some pre-established criterion. The simplest such redistribution (used in this model) is based on maintaining a (more or less) constant arc-length distance between nodes (i.e., segment length), throughout the computations. As the instability develops in time on the interface, VS roll-up occurs and the length of the interface increases significantly. Hence, to maintain the distance between nodes close to its original value, nodes are gradually added thereby improving the resolution of computations.

  In the Phase I model, regridding was implemented but did not achieve full success. Indeed, a gradual loss of accuracy of results was observed as regridding occurred. It was understood during Phase II that this loss of accuracy resulted from small errors in the re-interpolation, of the same nature as those discussed above for modeling of the geometry. After implementing the parity mapping method for the interpolation and using it in combination with regridding procedures, it was found that these errors were mostly eliminated.

  In the applications presented in Section 2.5.2, we compute the instability of a periodic interface in both conservative and non-conservative cases. In the former case, two identical fluids are used which requires that the circulation be conserved along the interface. If no regridding occurs, this requirement is automatically satisfied in the model equations. With regridding, however, total circulation can be re-calculated at each time step and compared to the initial circulation. Doing so, it was observed that a slight change in total circulation occurred before and after regridding which could be attributed to the slightly different geometry of the interface in the two discretizations. Through time stepping, it was further observed that total circulation drifted from its initial value. Hence, a method was implemented in the model to correct the circulation of individual vortex elements and ensure that total circulation remained constant through regridding, for a given time step.

The adaptive regridding method is detailed in a following section.

2.2.1 Element parity mapping

As mentioned before, in most earlier models based on point vortices, investigators reported that, as time increased, computations became gradually unstable and, eventually, led to irregular motion of discretization points (e.g., Moore [31]; Zalosh [43]; Meiron *et al.* [30]). Such instabilities are particularly strong when surface tension effects are included (Rangel and Sirignano [33]). In most of the previously reported work, after experiencing such problems, it was concluded that numerical instabilities were likely due to improper calculation/representation of VS's motion in the models. In some work, reduction in numerical instabilities were attempted, but with little success, by improving singular integration calculations.

A detailed analysis of this problem was done during Phase II which showed that irregular motions of vortex elements are always associated with an increasingly poor accuracy of the VS geometric representation and, particularly, of tangential s-derivatives. When KH instabilities develop, intense roll-up of VS's indeed occurs (e.g., Fig. 2.3), leading to large curvature of the interface and to enhanced surface tension effects. Hence, even if a lower-order representation may be acceptable for the circulation, a higher-order representation of the geometry is needed to ensure continuity of inter-element slope and curvature. This was also concluded by Grilli and Svendsen [21], who used cubic splines, and by Grilli and Subramanya [18, 20], who introduced a fourth-order sliding polynomial interpolation of the geometry, independent of the Boundary Element (BEM) shape functions, to calculate s-derivatives in their computations of overturning surface waves.

In the Phase I model, following Grilli and Subramanya, a five-node sliding interpolation of the geometry was first tested (i.e., 4th-order isoparametric boundary element in which geometric characteristics are calculated for the middle node of the element). Slope angle and tangential derivatives were calculated by direct differentiation in the sliding element, using a BEM representation in which the geometry of each element is represented by a set of $m = 5$ locally continuous polynomial shape functions $N_j(\mu)$, analytically defined on a reference *isoparametric element* using m discretization points (nodes) (parametric mapping in Fig. 2.2). Hence,

$$x(\mu) = \sum_{j=1}^{m} N_j(\mu) x_j \quad ; \quad y(\mu) = \sum_{j=1}^{m} N_j(\mu) y_j \quad ; \quad \gamma(\mu) = \sum_{j=1}^{m} N_j(\mu) \gamma_j \tag{2.19}$$

where x_j, y_j, and γ_j are coordinates and circulation for the element nodes, respectively. Derivatives with respect to the intrinsic coordinate (denoted by μ indices) are easily obtained from Eq. (2.19), using derivatives of shape functions. Key flow parameters of VS's evolution are functions of tangential s-derivatives of the interfacial slope angle β and curvature $\partial\beta/\partial s$. For each boundary element, these can be expressed as,

$$\cos\beta = \frac{x_\mu}{s_\mu} \quad ; \quad \sin\beta = \frac{y_\mu}{s_\mu} \quad ; \quad s_\mu = \{x_\mu^2 + y_\mu^2\}^{1/2} \tag{2.20}$$

$$\begin{aligned} \frac{\partial\beta}{\partial s} &= \frac{y_{\mu\mu}\cos\beta - x_{\mu\mu}\sin\beta}{s_\mu^2} \\ \frac{\partial^2\beta}{\partial s^2} &= \frac{y_{\mu\mu\mu}\cos\beta - x_{\mu\mu\mu}\sin\beta}{s_\mu^3} - \frac{3}{2\,s_\mu^4}\left[\,2\,x_{\mu\mu}y_{\mu\mu}\cos 2\beta - (x_{\mu\mu}^2 - y_{\mu\mu}^2)\,\sin 2\beta\,\right] \end{aligned} \tag{2.21}$$

which can easily be calculated using derivatives of Eq. (2.19). Hence, the geometry $(x(\mu), y(\mu))$, circulation $\gamma(\mu)$, and the Jacobian s_μ^k, of each VS element k, can be calculated with Eqs. (2.19) and (2.20) and substituted into the discretized BS integrals and, similarly, these and $\partial^2\beta/\partial s^2$ calculated with Eq. (2.21) can be substituted into the vorticity updating Eqs. (2.7) or (2.13). To calculate characteristics for the next node along the VS, the sliding element was moved forward by one node. The element was kept identical for the first 3 nodes and for the last 3 nodes on the sheet.

When using this sliding element for the KH problem, however, after providing the initial trend of VS roll-up, computations rapidly failed and led to irregular motion of nodes, independent of flow conditions and physical properties. A repetition of these calculations using cubic splines did not improve results. To better identify the nature of instabilities, in Phase II, both the sliding and spline element methods were used to calculate tangential derivatives for a simple sinusoidal interface. It was found that :

- the accuracy of tangential derivatives calculated in the reference element is a function of the location of nodes on the original interface, especially if the order of derivatives is high;
- the numerical instability or irregular motion of nodes is first triggered by inaccuracies in the higher-order s-derivatives, mostly at locations where a fairly non-uniform distribution of nodes occurs within one element.

These findings explain why, for the periodic KH problem, instabilities were first observed at the extremity nodes and in roll-up regions of the interface, where the periodic boundary condition is enforced and interface node spacing is most changed, respectively.

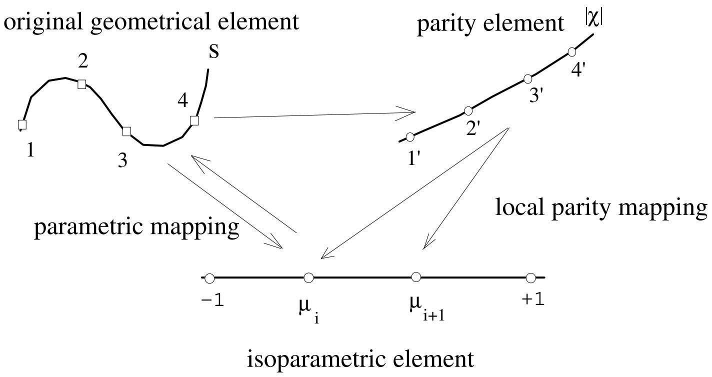

Figure 2.2: The Parity Mapping scheme for local isoparametric element

A careful analysis of these and similar results showed that the mapping of geometric elements, with irregular node spacing, to a reference element, with constant node spacing, is at the origin of small numerical inaccuracies in higher-order s-derivatives which, through time updating and enhanced surface tension effects in the roll-up regions, rapidly propagate and lead to sawtooth instabilities of the interface geometry. A new method, referred to as *parity mapping*, was thus designed to provide s-derivatives less dependent on discretization node density. Bases for this method are indicated in Fig. 2.2. In standard isoparametric element transformation, the distance between nodes in the reference element is constant. In Fig. 2.2, for instance, with a four-node element, it is equal to two-third. In the parity mapping method, a new (monotonous) mapping variable χ is defined, in between the transformation from s to μ, to create an element, with node density similar to the geometric element. The parity element is then mapped onto a reference element with intrinsic coordinate μ varying between [-1,+1] and irregular node spacing. Results show that this method eliminates (or at least greatly reduces) fluctuations induced in tangential derivatives due to irregular node spacing.

The (monotonous) parity coordinate χ is defined for element nodes i such as to carry the basic geometrical information from the original node distribution, as,

$$\chi_i = \chi_{i-1} + \sqrt{\mid x_i \mid + \mid y_i \mid} \quad ; \; i = 2, ..., m \tag{2.22}$$

for a m-node isoparametric element ($m \geq 4$ and even), with $\chi_1 = 0$, and the middle interval in the element starting at node $m/2$. The mapping interval in the reference element is, $\Delta\mu = \mu_m - \mu_1 = 2$, and the corresponding interval for the parity mapping element is,

$$\Delta\chi = \chi_m - \chi_1 = \sum_{j=1}^{m-1} \Delta\chi_j \quad \text{with} \quad \Delta\chi_j = \chi_{j+1} - \chi_j \tag{2.23}$$

The basic relationship for the parity mapping transformation expresses a geometric similarity between χ and μ, as,

$$\Delta\mu_i = \Delta\chi_i \frac{\Delta\mu}{\Delta\chi} \quad ; \; i = 1, ..., m-1 \tag{2.24}$$

For the 4-node element in Fig. 2, using Eq. (2.24), we thus have for the intermediate node coordinates ($m/2 = 2$),

$$\begin{aligned} \mu_2 &= \Delta\chi_2 \frac{2}{\Delta\chi} - 1 \\ \mu_3 &= \frac{2}{\Delta\chi}(\Delta\chi_2 + \Delta\chi_3) - 1 \end{aligned} \tag{2.25}$$

with $\Delta\chi$, $\Delta\chi_2$, and $\Delta\chi_3$ being given by Eqs. (2.22),(2.23), for the corresponding element nodal coordinates (x_i, y_i).

In the applications, the parity mapping method is used to calculate s-derivatives, based on 4-node cubic elements (as in Fig. 2.2). In this case, corresponding shape functions $N_j(\mu)$ are analytically recalculated for each element, depending on the μ_i values at intermediate nodes (i.e., here, μ_2 and μ_3 from Eq. (2.25), with $\mu_1 = -1$ and $\mu_4 = 1$ for the element extremity nodes), to satisfy the property $N_j(\mu_i) = \delta_{ij}$, as,

$$\begin{aligned} N_1(\mu) &= \frac{(\mu - \mu_2)(\mu - \mu_3)(1 - \mu)}{2(1 + \mu_2)(1 + \mu_3)} \\ N_2(\mu) &= \frac{(\mu + 1)(\mu - \mu_3)(\mu - 1)}{(1 + \mu_2)(\mu_2 - \mu_3)(\mu_2 - 1)} \\ N_3(\mu) &= \frac{(\mu + 1)(\mu - \mu_2)(\mu - 1)}{(1 + \mu_3)(\mu_3 - \mu_2)(\mu_3 - 1)} \\ N_4(\mu) &= \frac{(\mu + 1)(\mu - \mu_2)(\mu - \mu_3)}{2(1 - \mu_2)(1 - \mu_3)} \end{aligned} \tag{2.26}$$

Other geometric variables needed for the BS integrals are discretized using 4-node cubic isoparametric sliding boundary elements (i.e., with shape functions $N_j(\mu)$ given by Eq. (2.26), with $\mu_2 = -1/3$ and $\mu_3 = 1/3$), in which the middle interval only is used to interpolate between two nodes (*mid-interval interpolation*; Grilli and Subramanya [20]).

2.2.2 Adaptive regridding method

When VS's roll-up on the oil-water interface, some regions of the interface become significantly stretched, which leads to a reduced density of nodes and VS elements that may affect computational accuracy. In other regions of the interface, on the other hand, nodes will tend to concentrate which may lead to quasi-singular situations, particularly when point-vortices are used. In earlier work, node regridding methods were introduced to prevent point vortices from excessively concentrating in roll-up regions of the interface (e.g., by Rangel and Sirignano [33]) : nodes were adaptively added and regridded to equal arc-length spacing, according to the increased length of the interface with time, in order to satisfy a minimum

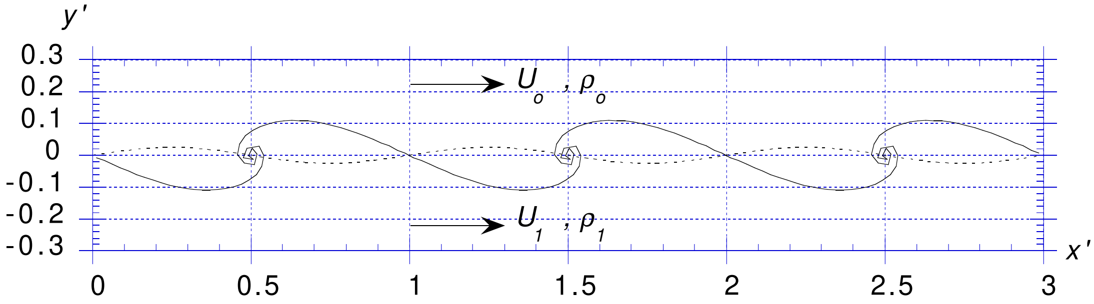

Figure 2.3: Sketch of computational set-up for periodic Kelvin-Helmholtz instability with wavelength λ (with, $x' = x/\lambda$, $y' = y/\lambda$). U_o, U_1 are uniform velocities and ρ_o, ρ_1 are densities, of fluid 0 and 1, respectively. Curve (- - - -) is the initial sinusoidal perturbation on the interface between fluid 0 and 1 and (——-) is the unstable interface computed at a later time.

spatial resolution requirement. In the applications of Section 2.5, for instance, nodes were added when the PCVS element average length increased or decreased by more than 1.5% over one time step.

In the present model, a similar node regridding technique is used, based on the method developed by Grilli and Subramanya [20] to study breaking surface waves. This method combines cubic spline elements and the new parity mapping interpolation method presented above. For the PCVS model, the circulation interpolation is performed at time step t^k, at the location of the regridded nodes, using the circulation densities calculated as,

$$\gamma_i^k = \frac{\Gamma_i^k}{\Delta s_i^k} \tag{2.27}$$

where i corresponds to the old node locations.

In addition, as mentioned before, a correction of the vortex elements circulation is performed in order to maintain a constant total circulation on the VS, through regridding at a given time step.

2.3 Periodic KH instability and equations for PCVS periodic model

2.3.1 KH instability problem

In this idealized problem, we consider a vertically stratified, statically stable system, made of two homogeneous immiscible inviscid fluids, of density ρ_1 (lower fluid) and $\rho_o \leq \rho_1$ (upper fluid), interfacial tension σ_{o1}, and infinite extension in the x direction, moving with uniform horizontal velocities U_1 and U_o, respectively (Fig. 2.3). We wish to calculate the evolution of the interface between the two fluids, as a function of time, under the action of *gravity, density difference, inertial*, and *interfacial tension* forces, when the interface is initially perturbed by a small periodic disturbance[1].

Hence, in the computations both an initial sinusoidal disturbance of wavelength λ and (small) amplitude a (i.e., $\propto a \sin 2\pi x/\lambda$), and a velocity jump, $\Delta U = \mid U_1 - U_o \mid$, are prescribed on the interface between both fluids. According to Lamb [26], the initial vorticity distribution $\gamma(x)$ corresponding to the specified geometry and velocity jump is,

$$\gamma(x) = \Delta U \left(1 \; + \; 2\pi\varepsilon \, \{ \, \kappa \sin (2\pi \frac{x}{\lambda}) - 2 \frac{\sqrt{\varphi \, (1 - W)}}{(1 + \varphi)} \, \cos (2\pi \frac{x}{\lambda}) \, \} \right) \tag{2.28}$$

with,

$$W = \{ \, (1 - \varphi) \frac{g}{k} + \sigma_{o1} \frac{k}{\rho_1} \, \} \, \frac{1 + \varphi}{\varphi (\Delta U)^2} \tag{2.29}$$

where $\varepsilon = a/\lambda$, $k = 2\pi/\lambda$ is the wavenumber, g is the acceleration of gravity, $\varphi = \rho_o/\rho_1$ is the density ratio, and $\kappa = (1 - \varphi)/(1 + \varphi)$ is the Atwood number.

This problem was solved by Lamb [26] in a linear framework (see p. 373 and p. 461). He found that a periodic disturbance would always be unstable and grow exponentially with time as $\propto \exp \omega t$, if,

$$\Delta U \; > \; \Delta U_{cr} \; = \; \frac{1 + \varphi}{\sqrt{\varphi}} \, c_o \tag{2.30}$$

with,

$$c_o = \left(\kappa \, \frac{g}{k} \; + \; \sigma'_{o1} \frac{k}{(1 + \varphi)} \right)^{1/2} \tag{2.31}$$

the speed of propagation of interfacial waves, $\sigma'_{o1} = \sigma_{o1}/\rho_1$, and,

$$\omega = k \, \Delta U \frac{\sqrt{\varphi \, (1 - W)}}{(1 + \varphi)} \tag{2.32}$$

Combining Eqs. (2.29) to (2.32), one sees that the instability criterion (2.30) also corresponds to $W < 1$.

According to Eq. (2.30), the growth of the instability will be maximum for a minimum value of c_o. Hence, calculating the critical wavelength λ^{min} leading to this minimum value and replacing it in Eqs. (2.30) and (2.31), we obtain the minimum critical velocity jump causing instability (i.e., the one for which $\omega = 0$ or $W = 1$) as,

$$\Delta U_{cr}^{min} = \left(2 \frac{1 + \varphi}{\varphi} \, \sqrt{\sigma'_{o1} \, g \, (1 - \varphi)} \right)^{1/2} \tag{2.33}$$

with,

$$\lambda^{min} = 2\pi \left(\frac{\sigma'_{o1}}{g \, (1 - \varphi)} \right)^{1/2} \tag{2.34}$$

[1] When the low density fluid is above, the interface is statically stable unless the superposition of a velocity across the perturbed interface can generate inertially induced Kelvin-Helmholtz (KH) instability (Kelvin [25]).

Lamb's solution assumes that the height of interfacial waves is infinitesimal. This is only an approximation, particularly if the instability is free to develop for a long enough time. As a first approximation, however, Lamb's solution can be used both to predict the threshold velocity likely to cause initial instability of interfacial waves, and the initial stages of growth of instability in the linear regime. Moreover, despite their limitations, as we will see, Lamb's equations contain the correct physical parameters influencing interfacial instability (i.e., fluid density ratio, interfacial tension, and gravity) that will be used in the numerically exact solution presented hereafter.

2.3.2 Governing equations for PCVS periodic model

In the periodic PCVS model, full nonlinearity of geometry and flow equations is kept by representing the interface as an inviscid vortex sheet (VS) whose motion is given by the Biot-Savart integral equation (2.1) (Batchelor [4]). Hence, for the infinite interface between both fluids, the complex motion $z(s,t)$ is given by,

$$\frac{dz}{dt}(s,t) = u(s,t) - i\,v(s,t) = \frac{i}{2\pi}\int_{-\infty}^{+\infty} \frac{\gamma(s')}{z(s,t)-z(s',t)}\,ds' \tag{2.35}$$

where, $i = \sqrt{-1}$, $z = x + iy$, and s is the curvilinear coordinate along the VS. The integral in Eq. (2.35) must be understood in a Cauchy Principal Value (CPV) sense and $\gamma(s)$ is the vortex sheet strength (i.e., circulation), satisfying conservative or non-conservative evolution equations, depending on the problem treated (see next section).

Due to spatial periodicity of the KH problem, Eq. (2.35) can be transformed into (Van de Vooren, [37]),

$$\begin{aligned} \mathrm{u}(\xi,\eta) &= \frac{d\xi}{d\tau} = \frac{1}{2}\int_0^{\mathrm{S}(\lambda)} \frac{\sinh 2\pi(\eta-\eta')}{\cosh 2\pi(\eta-\eta') - \cos 2\pi(\xi-\xi')}\,d\mathrm{g}' \\ \mathrm{v}(\xi,\eta) &= \frac{d\eta}{d\tau} = -\frac{1}{2}\int_0^{\mathrm{S}(\lambda)} \frac{\sin 2\pi(\xi-\xi')}{\cosh 2\pi(\eta-\eta') - \cos 2\pi(\xi-\xi')}\,d\mathrm{g}' \end{aligned} \tag{2.36}$$

where dimensionless variables introduced in Eqs. (2.9)-(2.12) have been used, and dashes denote variables calculated at point s' of the VS. The VS's nondimensional velocity field (u,v) and motion (ξ,η) induced by a known vorticity distribution can thus be obtained by solving Eq. (2.36). Due to the nonlinearity in the equations, this can only be performed numerically.

When the VS representing the infinite periodic interface between two fluids is discretized using Piecewise Constant Vortex Sheets (PCVS) elements, Grilli *et al.* [16] showed that Biot-Savart equations (2.36) reduce to,

$$\begin{aligned} \mathrm{u}_i &= \frac{1}{2}\sum_{j\neq i} \mathrm{g}_j \frac{\sinh 2\pi(\eta_i-\eta_j)}{\cosh 2\pi(\eta_i-\eta_j) - \cos 2\pi(\xi_i-\xi_j)} + \tilde{\mathrm{u}}_i \\ \mathrm{v}_i &= -\frac{1}{2}\sum_{j\neq i} \mathrm{g}_j \frac{\sin 2\pi(\xi_i-\xi_j)}{\cosh 2\pi(\eta_i-\eta_j) - \cos 2\pi(\xi_i-\xi_j)} + \tilde{\mathrm{v}}_i \end{aligned} \tag{2.37}$$

for $(i, j = 1, ..., N)$, with the indices denoting center points of PCVS elements.

In Eq. (2.37), the interface has been assumed to be discretized by N segments of length Δs_j (nondimensional length $\Delta \mathrm{s}_j$), with piecewise-constant vorticity density γ_j or $\Gamma_j = \gamma_j \Delta s_j$ (nondimensional value g_j). Velocities $\tilde{\mathrm{u}}_i$ and $\tilde{\mathrm{v}}_i$ denote nondimensional velocity contributions resulting from CPV integrals due to singularities occurring when the source point (x_i, y_i) or (ξ_i, η_i) coincides with the integration point (x_j, y_j) or (ξ_j, η_j) (i.e., self-induced velocity contributions). To our knowledge, since most existing models use (less accurate) point vortices, these periodic CPV integrals have never been exactly calculated in the literature. Only Van de Vooren [37] provided a first-order approximation for these, based on a Taylor series expansion of the singularities. Full analytical expressions for $\tilde{\mathrm{u}}_i$ and $\tilde{\mathrm{v}}_i$ can be found in Grilli *et al.* [16] (their Eqs. 4.14 to 4.16). More accurate expressions of CPV velocities for continuous vortex sheets are given in Section 3.1.

The general numerical procedures used in the periodic PCVS model are those presented in Section 2.2.

2.4 Oil/boom containment problem and equations for the non-periodic PCVS model

2.4.1 Oil/boom containment problem

This problem physically corresponds to Figs. 1.2 to 1.4 and, for the numerical PCVS model, is illustrated by Fig. 2.1 where one can see that various interfaces between fluids and fluid or solid boundaries (air-water, oil-water, oil-boom, water-boom) are represented by semi-infinite VS's or discretized PCVS. Governing equations are the Biot-Savart Eqs. (2.1), for calculating the velocity field induced by vorticity distributions on the VS's, Eq. (2.2), for calculating the VS's movements as a function of time, and Eqs. (2.7) or (2.13), for calculating the time rate of change of vorticity along the VS's.

During Phase I studies, a simplified oil/boom containment problem was solved, following the methodology proposed by Zalosh [42], in which a semi-infinite oil slick was modeled (i.e., without a boom), and the headwave instability of the contained oil slick was calculated. Hence, to model this problem, two discretized PCVS were used, for the oil-water and the oil-air interfaces, together with three semi-infinite VS's. Computational results for this problem showed that, for sufficiently large flow velocity, the expected VS roll-up occurred in the front of the slick (see also [17] for numerical results).

During Phase II studies, the computations of instabilities in oil/boom containment systems were extended to more realistic cases including a finite slick and a solid boom. In such cases, the water-air interface in front of the slick was also discretized as a PCVS to account for the dip of the free surface observed in experiments at the slick leading edge. Doing so, 5 discretized PCVS and 3 semi-infinite or infinite VS's were used in the model (Fig. 2.4), which made it necessary to address problems of velocity and displacement compatibility at multiple intersection points between sheets.

In the following, governing equations for a PCVS multiple sheet system are first presented. Then, numerical methods specific to this problem, such as the initial conditions are presented and the treatment of multiple intersection points.

2.4.2 Governing equations for PCVS non-periodic model

For a one sheet system, discretized with N PCVS elements, Biot-Savart equations (2.1) transform into [16] (for $i = 1, ..., N$),

$$\begin{aligned} u_i &= \frac{1}{2\pi} \sum_{j \neq i} \frac{y_i - y_j}{r_{ij}^2} \Gamma_j + \tilde{u}_i \\ v_i &= -\frac{1}{2\pi} \sum_{j \neq i} \frac{x_i - x_j}{r_{ij}^2} \Gamma_j + \tilde{v}_i \end{aligned} \tag{2.38}$$

with $\Gamma_i = \gamma_i \Delta s_i$, the vorticity attributed to each PCVS element i, r_{ij}, the distance between the centers of elements i and j of coordinates (x_i, y_i) and (x_j, y_j), and $(\tilde{u}_i, \tilde{v}_i)$ the CPV's contributions to the velocity field (u_i, v_i) given by,

$$\begin{aligned} \tilde{u}_i &= -\frac{1}{2\pi} \frac{\Gamma_i}{\Delta s_i} \sin\beta_i \log \frac{r_{i+1/2}}{r_{i-1/2}} \\ \tilde{v}_i &= +\frac{1}{2\pi} \frac{\Gamma_i}{\Delta s_i} \cos\beta_i \log \frac{r_{i+1/2}}{r_{i-1/2}} \end{aligned} \tag{2.39}$$

where β_i is the angle between the x-axis and segment i, and $[r_{i-1/2}, r_{i+1/2}]$ denote distances from both extremities to the mid-point of element i.

When M PCVS's and some semi-infinite sheets are used (as in Fig. 2.4), using nondimensional variables (2.9) to (2.12), Eq. (2.39) is generalized as an equation for the velocity at point i of sheet l as (for $i = 1, ..., N_l$; $l = 1, ..., M$),

$$\begin{aligned} \mathrm{u}_i^l &= \sum_{k=1}^{M} \left(\frac{1}{2\pi} \sum_{j \neq i = 1}^{N_k} \frac{\eta_i^l - \eta_j^k}{(\mathrm{r}_{ij}^{kl})^2} \mathrm{g}_j^k + \tilde{\mathrm{u}}_i^k \right) + \mathrm{u}_{\ell r} \\ \mathrm{v}_i^l &= \sum_{k=1}^{M} \left(-\frac{1}{2\pi} \sum_{j \neq i = 1}^{N_k} \frac{\xi_i^l - \xi_j^k}{(\mathrm{r}_{ij}^{kl})^2} \mathrm{g}_j^k + \tilde{\mathrm{v}}_i^k \right) + \mathrm{v}_{\ell r} \end{aligned} \tag{2.40}$$

where indices k and l denote the PCVS number, r_{ij}^{kl} denotes the nondimensional distance between point i on sheet l and point j on sheet k (k and $l = 1, ..., M$), calculated as,

$$\mathrm{r}_{ij}^{kl} = \sqrt{(\xi_i^l - \xi_j^k)^2 + (\eta_i^l - \eta_j^k)^2} \tag{2.41}$$

and $(\mathrm{u}_{\ell r}, \mathrm{v}_{\ell r})$ denote nondimensional velocities induced by semi-infinite vortex sheets, calculated as in Eq. (2.17) and divided by ΔU, the reference velocity jump, and, using Eq.

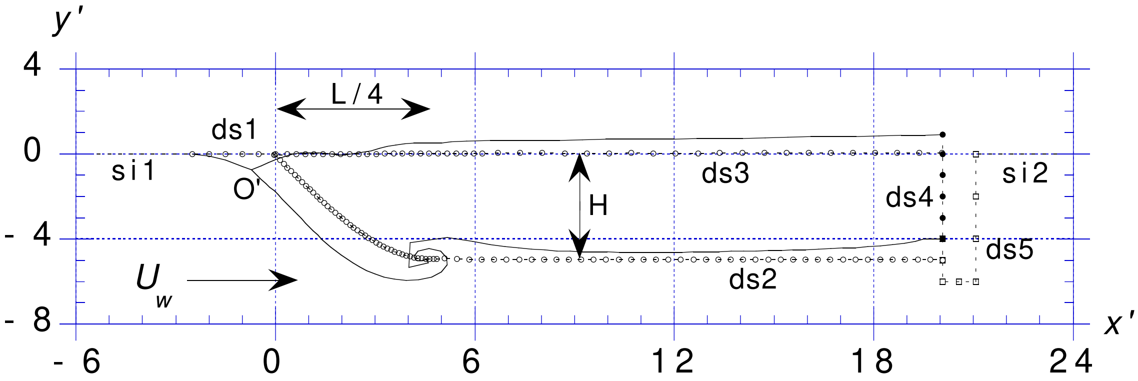

Figure 2.4: Sketch of computational domain for headwave instability of a contained oil slick, with definition of main parameters : U_w = water velocity with respect to slick ($U_o = 0$ in slick); air velocity can be set to U_a and interfacial tensions are σ_{oa} and σ_{ow}; fluid densities are $\rho_a = 0$, ρ_o and ρ_w; si1 and si2 = two semi-infinite vortex sheets on the air-water interface (an infinite sheet si3 (not shown) represents the bottom); ds1 to ds5 = five discretized PCVS; ○, ●, and □ = centers of discretized vortex elements. (- - - - -) initial shape of the slick based on Zalosh [42] (Eqs. (2.43), (2.44)); (———-) unstable shape computed at a later time.

(2.39), $(\tilde{u}_i^k, \tilde{v}_i^k)$ denote the nondimensional CPV self-induced velocity contributions given, for points i on sheet k, as,

$$\begin{aligned} \tilde{u}_i^k &= -\frac{1}{2\pi}\frac{g_i^k}{\Delta s_i^k}\sin\beta_i^k \log\frac{r_{i+1/2}^k}{r_{i-1/2}^k} \\ \tilde{v}_i^k &= +\frac{1}{2\pi}\frac{g_i^k}{\Delta s_i^k}\cos\beta_i^k \log\frac{r_{i+1/2}^k}{r_{i-1/2}^k} \end{aligned} \tag{2.42}$$

The general numerical procedures used in the non-periodic PCVS model are identical to those presented in Section 2.2. Numerical methods specific to the oil/boom problem are presented hereafter.

2.4.3 Numerical procedures specific to the oil/boom problem

Initial conditions

To solve Eq. (2.2), together with Eqs. (2.40)-(2.42) and (2.13)-(2.16), an explicit time stepping algorithm is used (as described in [16, 17]) for which initial conditions for the VS's geometry and circulation must be provided. Since several discretized VS's are included in the computational domain, the initial flow conditions on each sheet have to be estimated depending on their initial shape (Figs. 2.1, 2.4). In the present studies, however, since no frictional effects are yet included in the vorticity updating equations, the initial shape of the slick cannot yet be assumed to be the quasi-steady state shape of the slick, as calculated using the method of Section 4. This will be done during Phase III studies. Instead, in the present case, in order to validate the non-periodic PCVS model for the oil/boom containment problem, the initial shape of the oil-water interface (ds2) was assumed to be the semi-empirical shape proposed by Zalosh [42], based on the observation of various experimental results, to represent the headwave region of a slick, i.e. (Figs. 2.1, 2.4),

$$\begin{aligned} \eta(x) &= H \sin(2\pi\, x/L) \qquad && \text{for } 0 \leq x \leq L/4 \\ \eta(x) &= H && \text{for } L/4 \leq x \leq L \end{aligned} \tag{2.43}$$

where H and L are the initial depth and length of the slick headwave, respectively (Fig. 2.4). Assuming flat air-water and air-oil interfaces at $y = 0$ (ds1,ds3) and quasi-hydrostatic equilibrium in the oil slick, we obtain, using Bernoulli's equation between the front and the back of the slick,

$$H = \frac{U_w^2}{2g\,(1-\varphi)} \tag{2.44}$$

where U_w is the free stream water velocity. Following the work by Von Karman [38] for density intrusions along solid boundaries, Zalosh assumed a 60° value for the angle of the headwave at the leading edge. With this angle, Eq. (2.43) yields $L = 3.63H$. As pointed out by Zalosh, experimental results usually show smaller angles at the leading edge, which results in increased values of L (see, e.g., Milgram and Van Houten [29]).

According to Eq. (2.3), the initial circulation along VS's is equal to the velocity jump at the sheets. Assuming a steady-state flow and a mildly sloping oil-water interface, pending the use of the initialization method of Section 4, the initial tangential velocity along the slick is estimated as the projection of the free stream velocity in the tangential direction. Hence, according to Eqs. (2.3)-(2.5), the initial circulation of PCVS elements on the VS ds2 is given by,

$$\Gamma_i^2 = \Delta s_i^2\, U_w\, \cos\beta_i^2 \tag{2.45}$$

The same equation is applied to estimate the initial circulation Γ_i^5 on the water-boom sheet ds5. For still air and oil, the initial circulation on the oil-water sheet ds3 is selected as zero, i.e., $\Gamma_i^3 = 0$. For the oil-boom sheet ds4, however, despite the assumption of no initial flow in the oil slick, to ensure numerical stability, it was found necessary to linearly vary the initial circulation Γ_i^4 along ds4, from the value on the last segment of sheet ds2 on the boom, to 0, when moving upward along the sheet. Otherwise, the initial circulation jump from sheet ds2 to ds4 was found to cause irregular motions of PCVS elements on the oil-water interface and, eventually, to cause numerical instability of the computations. This is because, as numerical results show, as time increases, a slow but non-zero (inviscid) flow is induced in the oil slick, as a result of the velocity jump at the oil-water interface; hence, initial conditions must account for this flow.

Multiple sheet intersection points

At *Multiple Sheet Intersection Points* (MSIP), such as O' in Fig. 2.4, the flow velocity must be continuous and the circulation must also satisfy Kelvin's theorem. Compatibility

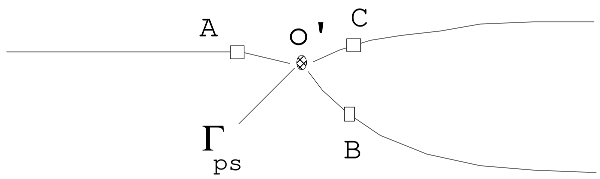

Figure 2.5: Sketch of triple (fluid) sheet intersection point at the oil slick leading edge, in the non-periodic discretized PCVS model. (□) denote last PCVS element centers on sheets ds1, ds2, and ds3.

conditions have been developed to enforce these physical requirements in the discretized PCVS model equations.

As seen in Fig. 2.4, MSIP's occur on the boom solid boundary (ds2-ds4, ds3-ds4) and at the slick leading edge O' (ds1-ds2-ds3). As an additional difficulty, point O' is a moving triple MSIP and the ds2-ds4 and ds3-ds4 MSIP's can move up and down along the boom surface. The motion of these MSIP's is not correctly predicted by the Biot-Savart equations, when discretized for PCVS elements located on separate VS's. Hence, additional compatibility equations are required to correctly describe the behavior of MSIP's.

The triple MSIP O' at the slick leading edge is sketched in Fig. 2.5 as the geometric intersection of sheets ds1-ds2-ds3. Theoretically, this intersection node is free to move in an arbitrary direction. This direction, however, must physically be related to the instantaneous motion of neighboring nodes A, B, C, on sheets ds1, ds2, ds3, respectively. For the analysis of the motion of point O', let us assume that there is a point vortex of strength Γ_{ps} located at O' (no discretization node is actually located at O' in the discretized PCVS model, since computational nodes are located at the middle of VS elements; Fig. 2.5). The assumption of a moving point vortex at O' requires that the circulation Γ_{ps} be such as to balance the average accumulation of circulation at nodes A, B, and C, i.e.,

$$\Gamma_{ps} = \frac{\alpha_{ps}}{m} \sum_{k=1}^{m} \Gamma_{\ell}^{k} \tag{2.46}$$

where α_{ps} is a constant to be numerically determined in the [0,1] range, m is the number of connecting sheets at point O' (i.e., $m = 3$ for the slick leading edge), and index ℓ denotes the last PCVS element on sheet k (i.e., points A, B, and C in Fig. 2.5). Computations would normally begin with $\alpha_{ps} = 1.0$ and the additional contribution of the circulation Γ_{ps} to the computation of the (nondimensional) velocity field, at point i on sheet l, using Eq. (2.40), is given by,

$$\begin{aligned} \mathrm{u}_{i,ps}^{l} &= \frac{\mathrm{g}_{ps}\,(\eta_i^l - \eta_{o'})}{2\pi\,(\mathrm{r}_{i,o'}^{l})^2}\,[1-\exp(-\frac{(\mathrm{r}_{i,o'}^{l})^2}{R_c^2})] \\ \mathrm{v}_{i,ps}^{l} &= -\frac{\mathrm{g}_{ps}\,(\xi_i^l - \xi_{o'})}{2\pi\,(\mathrm{r}_{i,o'}^{l})^2}[1-\exp(-\frac{(\mathrm{r}_{i,o'}^{l})^2}{R_c^2})] \end{aligned} \tag{2.47}$$

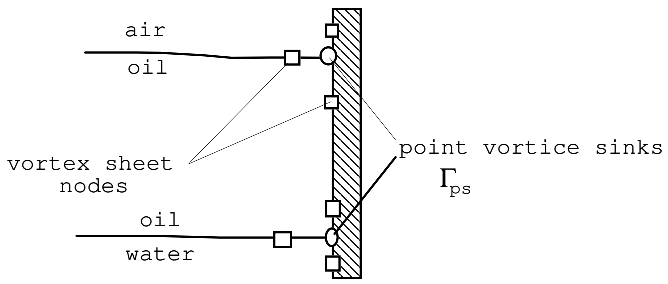

Figure 2.6: Sketch of double (fluid-solid) sheet intersection points along the boom, in the non-periodic discretized PCVS model.

with,

$$\mathrm{r}^{l}_{i,o'} = \sqrt{(\xi^{l}_{i} - \xi_{o'})^2 + (\eta^{l}_{i} - \eta_{o'})^2} \tag{2.48}$$

where $(\xi_{o'}, \eta_{o'})$ denote dimensionless coordinates of the MSIP O', and R_c is the nondimensional radius ($R_c < 1.0$) of a fictitious viscous core surrounding the point vortex Γ_{ps}. This viscous core method, introduced earlier by Zalosh [42], locally damps high frequency geometrical oscillations on the VS's and was found necessary in the present case to ensure the smooth behavior of numerical results at point O'. Finally, the motion of the triple MSIP O' is calculated in the model by assuming that the point moves with the average velocity of the adjacent nodes on the 3 intersecting sheets (i.e., A, B, C).

The other two MSIP's along the boom are intersections points ds2-ds4 and ds3-ds4 shown in Fig. 2.6. To satisfy the no-flow condition on the boom solid boundary, these two nodes are only allowed to move in the tangential direction at the boom surface (i.e., here, in the vertical direction). The numerical treatment of these nodes is similar to node O'. The circulation Γ_{ps} is first estimated ($t = 0$) at fictitious point vortices located at the geometric intersections of the VS's (Fig. 2.6), using Eq. (2.46) for $m = 2$, as the average value of the initial circulation at the extremity nodes of the intersecting sheets. As time progresses, however, small numerical errors occur at the boom which, in some cases, may make PCVS elements slightly penetrate the boom surface. In such cases, penetrated VS's sections are cut off from the discretized PCVS's, which results in a small loss/gain of circulation, say $\Delta\Gamma_{ps}$, at a given time t. To ensure that circulation is conserved, $\Delta\Gamma_{ps}$ is added to Γ_{ps} at each time step. As before, the contribution of Γ_{ps} to the induced velocity field is calculated with Eqs. (2.47) and (2.48).

2.5 Applications of PCVS models

2.5.1 Study of PCVS model convergence and stability

The numerical accuracy of the PCVS model solution depends on both the selected spatial discretization, i.e. number of *discretization nodes*, and temporal discretization, i.e. *time*

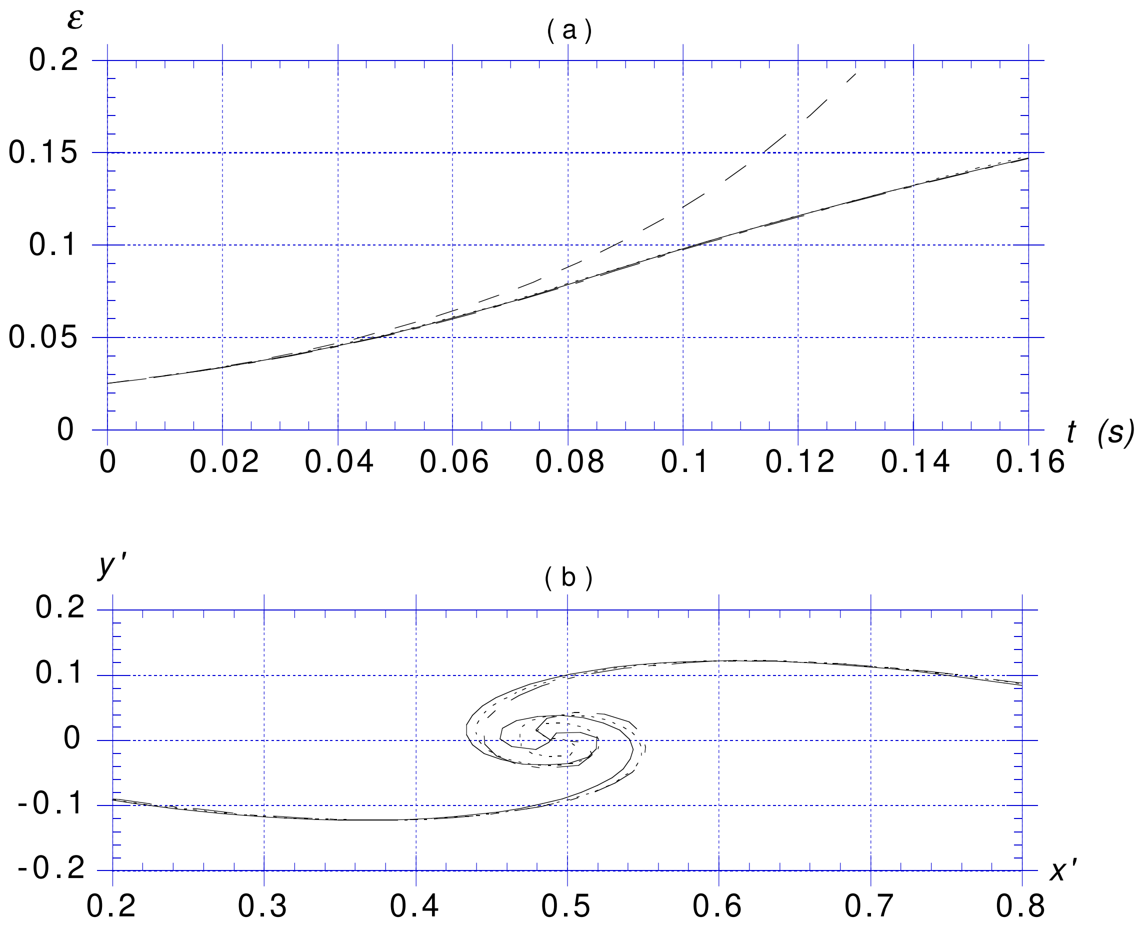

Figure 2.7: *Convergence with refinement of spatial discretization.* Computations of KH instability in a set-up similar to Fig. 2.3 with $\Delta U = 0.50$ m/s, $\varphi = 1$ (same fluid), $\lambda = 0.1$ m, and no gravity and surface tension. The time step is $\Delta\tau = 0.0001$ and the initial perturbation is a sinusoidal wave with amplitude $\varepsilon = 0.025$ and vorticity distribution according to Eq. (2.28). Initial numbers of PCVS elements $N =$ (—- - —-) 45, (——) 60, (- - - - -) 75. (a) Maximum amplitude of interfacial disturbance compared to (— —) the linear growth rate (Lamb [26]). (b) Interfacial shape at $t = 0.128$ s.

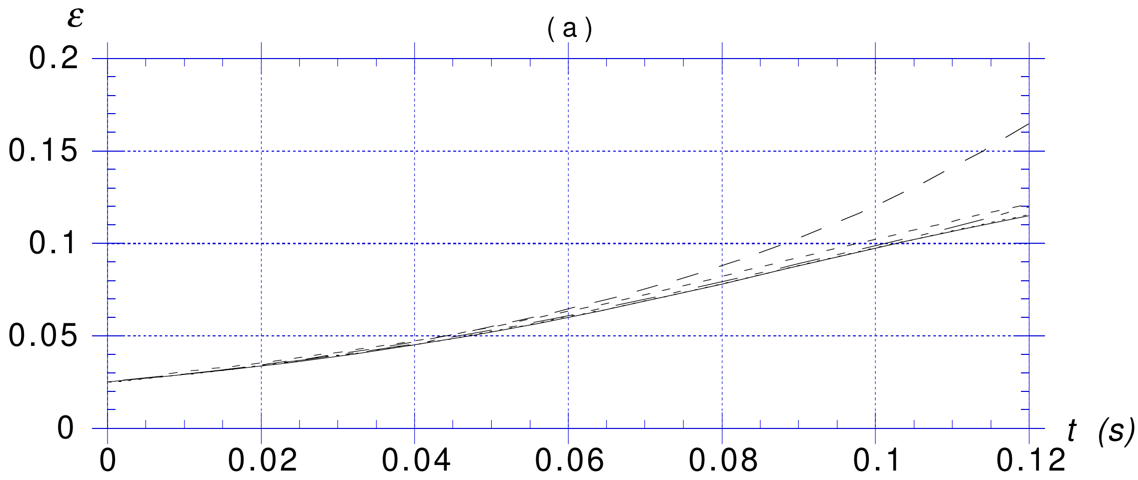

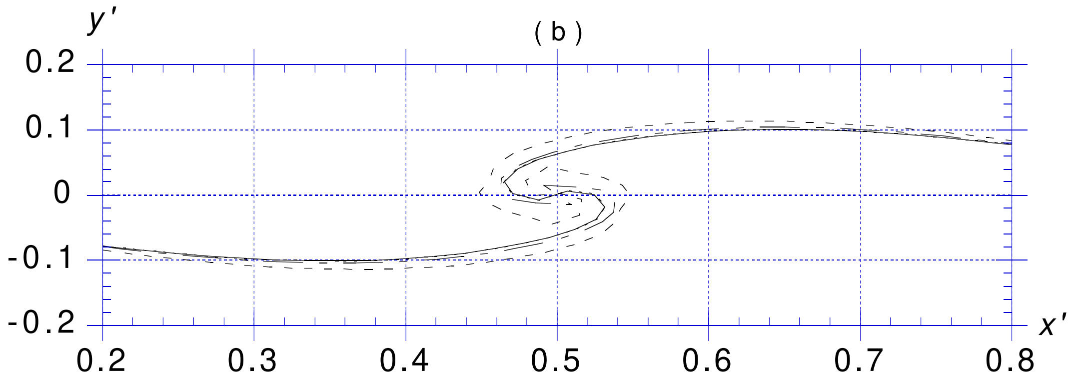

Figure 2.8: *Stability with increasing time step.* Same physical case as in Fig. 2.7 with $N = 45$ and time steps $\Delta\tau =$ (———) 0.0001, (- - - - - -) 0.001, (— - —) 0.01, (– – –) 0.04. (a) Maximum amplitude of interfacial disturbance compared to (— —) the linear growth rate (Lamb [26]). (b) Interfacial shape at $t = 0.108$ s.

step size. Although no absolute measure of accuracy is available for an arbitrary non-conservative case, the convergence of the solution with the discretization must be achieved if the model is to be recognized as stable and accurate. Hence, in this first application, the numerical convergence of the PCVS model numerical algorithms is tested by varying both the time step size and the number of discretized PCVS elements, within certain ranges. Since almost identical numerical methods are used for both the periodic and non-periodic PCVS models, convergence and stability are studied using the simpler periodic PCVS model and studying a case of KH instability on a periodic interface, as illustrated in Fig. 2.3.

For simplicity, the case solved with the periodic PCVS model is a pure shear instability case, with two identical fluids of unit density ($\varphi = \rho_o/\rho_1 = 1$) and hence no gravity, surface tension, and density difference effects. For such a case, circulation is conservative ($D\Gamma_i/Dt = 0$ in Eq. (2.7)) and, since there are no stabilizing effects, the linear analysis shows unconditional instability for $\mid \Delta U \mid > 0$, with a growth rate, $\propto \exp{(\pi \Delta U t/\lambda)}$ (Lamb [26]).

The physical parameters selected for this case are $\Delta U = 0.5$ m/s and $\lambda = 0.1$ m. The initial disturbance on the free surface is sinusoidal with nondimensional amplitude $\varepsilon = 0.025$ and the initial circulation distribution is specified according to Eq. (2.28). A very small non-dimensional time step $\Delta\tau = 0.0001$ was first used and the initial number of PCVS elements on the interface was set to N =45, 60, and 75, in three successive computations. Regridding was used throughout the computations, to maintain a more or less constant node density along the interface as time progresses (maximum accepted PCVS element length variation over one time step was 1.5 %). Thus, in the three present cases, the number of PCVS elements at $t = 0.128$ s (Fig. 2.7b) reached 77, 106, and 128, respectively. The predicted evolutions of maximum nondimensional interfacial amplitudes are compared in Fig. 2.7a, and one can see differences between computations with different node resolution are very small. Also, note the initial agreement for $t < 0.04$ s and the subsequent differences shown in the figure between the amplitude growth rates obtained with the present nonlinear model and the rate predicted by linear theory. Clearly, for sufficiently large time, nonlinearity increases due to larger amplitudes on the interface and the instability grows slower in the nonlinear model than predicted by linear theory. This confirms earlier findings [43, 33] that nonlinearity provides stabilizing effects for the KH instability. In Fig. 2.7b, free surface shapes are compared for $t = 0.128$s, at a time where strong roll-up of the interface has occurred. Again, differences between the three cases are not significant, except in the small roll-up region where jet resolution is more dependent on the number of PCVS elements.

Computations were then performed for the same physical case, initially discretized with $N = 45$, using four constant time step sizes varying between $\Delta\tau = 0.0001$ and 0.04. [Due to regridding, at $t = 0.108$ s, the number of nodes increased to 61 and 75, for the first two and last two time steps, respectively.] Results for the maximum amplitude evolution and for the free surface shape at $t = 0.108$ s are given as a function of the time step size, in Figs. 2.8a and b. Amplitude growth rates and free surface shape slightly change as the time step increases but differences are not very significant until $\Delta\tau > 0.01$. For $\Delta\tau = 0.04$, computations rapidly become divergent for $t > 0.12$ s.

These two applications of the periodic PCVS model, hence, first show the good convergence of results with refined discretization (a feat rarely achieved in earlier published models, likely due to inadequate CPV integrations) and the stability of model results over a wide range of nondimensional time step size covering two orders of magnitude, from 0.0001 to 0.01.

2.5.2 Application of the periodic PCVS model to KH instability

After assessing the convergence and stability of the PCVS model numerical algorithms, the periodic model is now used to study the KH instability itself as a function of the physical factors known from the literature to influence the growth rate of instability, namely the interfacial velocity jump ΔU, the presence of gravity g (i.e., whether the two-dimensional instability occurs in a horizontal plane (no gravity), or in a vertical plane), the fluid density difference or ratio $\varphi = \rho_o/\rho_1$, the interfacial tension σ_{o1}.

Based on the literature review and the physical analysis of the linear KH problem presented earlier, for velocity jump values beyond the critical value, we expect an increase in ΔU to intensify the growth rate of instability and gravity to provide a stabilizing effect, we expect a decrease in φ to reduce the instability, and an increase in σ_{o1} to also reduce the instability. Numerical tests are carried out in the following, with the periodic PCVS model, to both confirm and quantify these expected behaviors.

Influence of velocity jump on growth rate of instability

In a linear sense [26], according to Eq. (2.30), when the velocity jump at the interface is greater than the critical value, $\Delta U > \Delta U_{cr}$, the interface amplitude ε will grow exponentially with time, as $\varepsilon(t) \propto \exp \omega t$ and, all other factors being equal (i.e., k, φ, and σ_{o1}), the growth rate ω will increase with ΔU (see Eqs. (2.29) and (2.32)). For sufficiently large interfacial amplitude, however, due to increased nonlinearity, one should expect the linear solution to fail to predict the actual growth rate. In fact, nonlinearity should provide additional stabilizing effects reducing the growth rate.

The following numerical experiments were carried out with the periodic PCVS model to assess the effects of the velocity jump on the growth rate of KH instability. In all cases, the maximum interfacial wave amplitude ε was calculated as a function of time and compared to Lamb's [26] linear solution for the same parameter values.

Physical parameter values selected for this case were : a density ratio corresponding to a case with water and an average oil, $\varphi = 0.9$ (with $\rho_1 = 1000$ kg/m^3), a standard surface tension coefficient for a water-oil interface, $\sigma_{o1} = 0.0237$ N/m, and gravity $g = 9.8$ m/s^2. In the numerical model, $N = 45$ PCVS elements were specified on the initial free surface and more were added through adaptive regridding, up to $t = 0.168$ s. The time step interval was set to $\Delta\tau = 0.0001$. The initial sinusoidal disturbance on the free surface had an initial amplitude $\varepsilon = 0.025$ and the initial circulation distribution was specified according to Eq. (2.28).

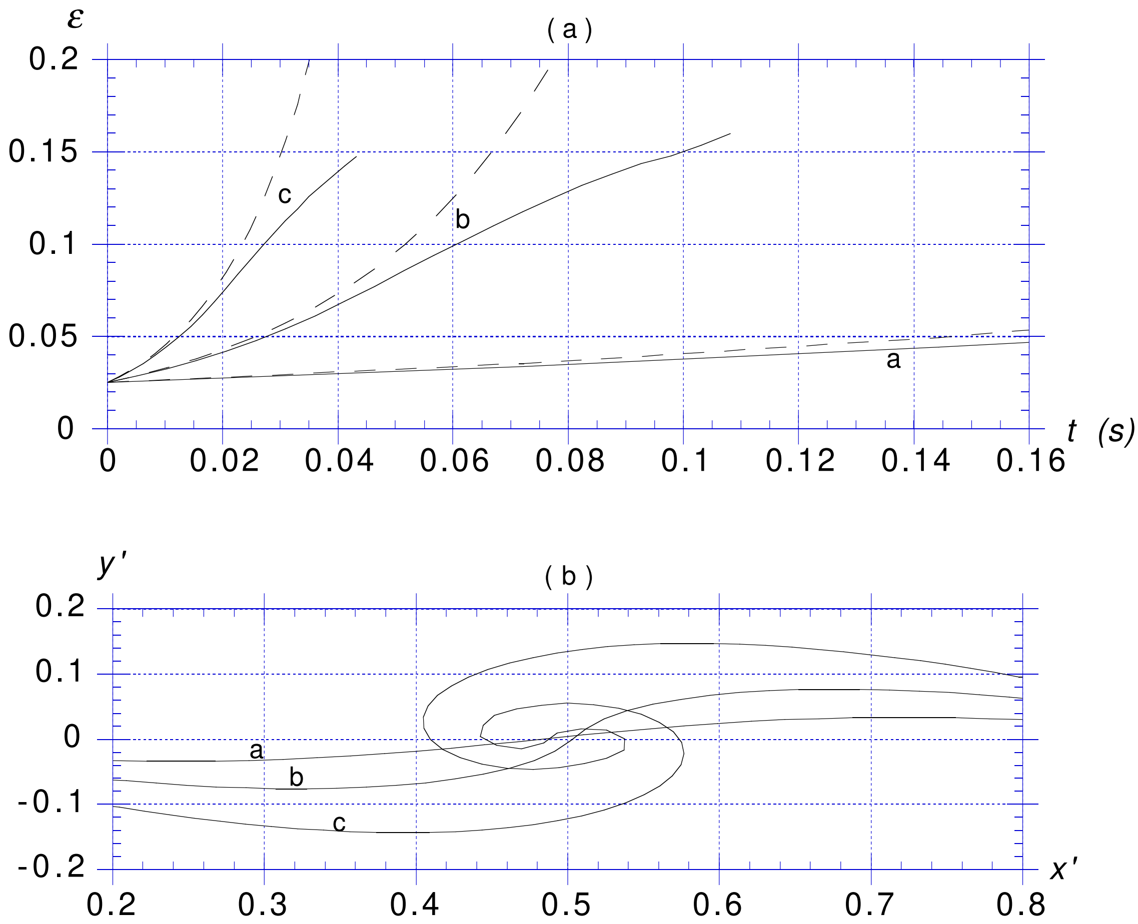

Figure 2.9: *Influence of velocity jump.* Computations of KH instability in a set-up similar to Fig. 2.3 with ΔU = a : 0.15 ; b : 0.30; and c : 0.60 m/s, $\lambda = 0.0309$ m, $\varphi = 0.9$, $\sigma_{o1} = 0.0237$ N/m, $N = 45$, time step $\Delta\tau = 0.0001$, and $g = 9.8$ m/s^2. The initial perturbation is a sinusoidal wave with amplitude $\varepsilon = 0.025$ and vorticity distribution according to Eq. (2.28). (a) Maximum amplitude of interfacial disturbance compared to (— —) the linear growth rate (Lamb [26]). (b) Interfacial shape at $t = 0.045$ s.

According to Eq. (2.34), the interfacial wavelength leading to maximum growth rate of instability for this case is, $\lambda^{min} = 0.0309$ m (i.e., $k = 203.34$ m^{-1}); hence this minimum wavelength is in the ripple wave range. This wavelength will be used in the present computations and, hence, $\lambda = \lambda^{min}$. According to Eq. (2.33), the corresponding linear critical velocity jump for the parameters selected in this case is, $\Delta U_{cr} = \Delta U_{cr}^{min} = 0.143$ m/s. Hence, in the following experiments, the velocity jump ΔU will be set to successive values larger than ΔU_{cr}^{min}, equal to 0.15, 0,30, and 0.60 m/s. [Due to regridding, at time $t = 0.045$ s, the number of nodes has increased to 46, 54, and 108, for each case, respectively.]

Results are given in Fig. 2.9. Fig. 2.9a confirms the expected result that the growth rate of instability increases with ΔU (i.e., the slope of curves a, b, and c increases with ΔU), in both the linear and nonlinear cases (PCVS model). In all cases, the linear and nonlinear growth rates are nearly identical for small time, confirming the good behavior of model equations. In the first case (a), the velocity jump is only slightly larger than the critical value and the initial instability is very slow to develop. Hence, the nonlinear growth rate is just slightly lower than the linear one up to $t = 0.16$ s. When computing this case for a longer time, however, one would see that nonlinearity eventually stabilizes the interface shape and that the amplitude stops growing for $t \geq 0.35$ s, and then starts decreasing, whereas the linear instability keeps developing. Therefore, in the nonlinear regime, case a is physically stable, although the amplitude will be seen to oscillate (i.e., beat) between a maximum and minimum value as time increases. In the other two cases (b and c), the velocity jump is more than twice and four times the linear critical value, which makes the interfacial amplitude grow much faster than in case a (where $\Delta U = 1.05\Delta U_{cr}$) and quickly leads to larger nonlinear effects. As a result, nonlinear PCVS results rapidly deviate from the linear prediction and, as expected, show significantly smaller growth rates than linear results; hence, case b and c, although unstable, correspond to physically more stable cases than predicted by linear theory. In Fig. 2.9b, one further sees that interfacial shapes at $t = 0.045$ s (a time for which intense VS roll-up has already occurred for case c) are very different for the three cases : almost no change in shape has occurred for case a whereas, for cases b and c, the interface has grown steeper and has even rolled up for case c.

Influence of gravity on growth rate of instability

Rangel and Sirignano [33] studied the KH instability problem without including gravity effects. They also used a numerical point vortex method that was likely less accurate than the present method (both due to lack of CPV integrals in BS equations and a cruder geometric representation of the interface). The following numerical experiments were carried out for a case similar to one of the cases solved in [33], to assess the effects of gravity on the growth rate of KH instability represented by the maximum interfacial wave amplitude ε as a function of time. Physical parameter values for this case were : a velocity jump $\Delta U = 0.5$ m/s, $\lambda = 0.1$ m, a density ratio $\varphi = 0.9$ (as for a case with water and an average oil of density 0.9), a surface tension coefficient $\sigma_{o1} = 0.0237$ N/m (water-oil standard value). Numerical

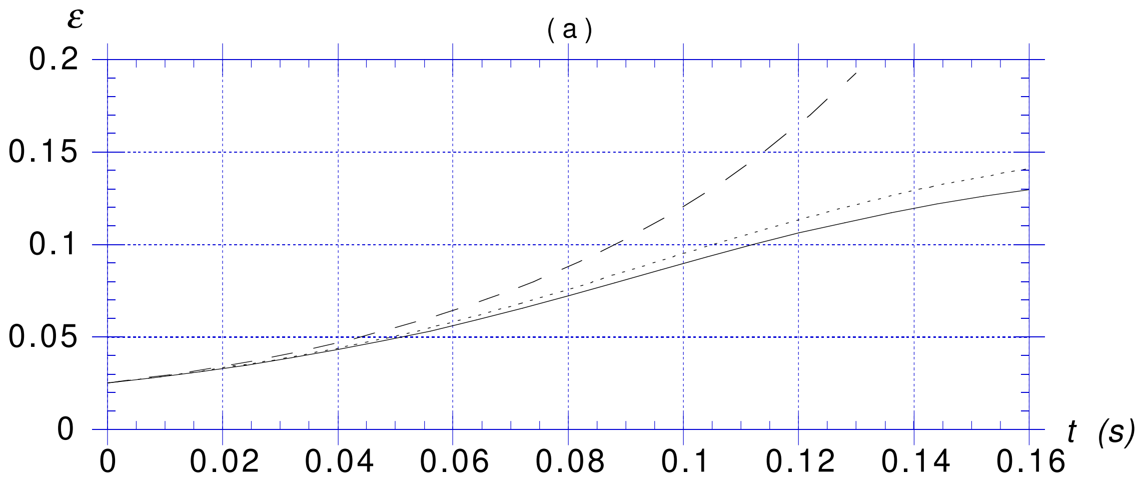

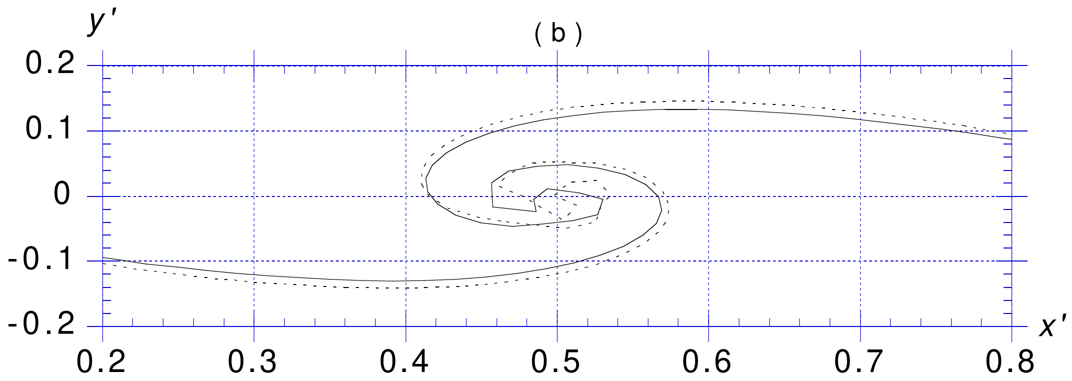

Figure 2.10: *Influence of gravity.* Computations of KH instability in a set-up similar to Fig. 2.3 with $\Delta U = 0.50$ m/s, $\lambda = 0.1$ m, $\varphi = 0.9$, $\sigma_{o1} = 0.0237$ N/m, $N = 45$, time step $\Delta\tau = 0.0001$, and g = (———) 9.8 m/s^2, (- - - - - -) 0. m/s^2. The initial perturbation is a sinusoidal wave with amplitude $\varepsilon = 0.025$ and vorticity distribution according to Eq. (2.28). (a) Maximum amplitude of interfacial disturbance compared to (— —) the linear growth rate (Lamb [26]). (b) Interfacial shape at $t = 0.168$ s.

parameters are the same as for the cases in the previous section. [Due to regridding, at time $t = 0.168$ s, the number of nodes has increased to 87 and 88, with and without gravity, respectively.]

For the above data, the linear critical velocity is $\Delta U_{cr} = 0.19$ m/s. Hence the present case is strongly unstable.

When including gravity effects in the model, the interface evolution is affected by additional inertial forces. Hence, the momentum of particles on the interface must slightly change to balance the vertical accelerations resulting from gravity effects. Thus, less momentum is available for further deforming the interface, which should lead the growth rate of instability to be smaller with gravity than without gravity. Numerical results reported in Fig. 2.10a confirm this analysis. Moreover, whether gravity is included or not, one can also see that, as compared to the linear growth rate, as expected, nonlinear PCVS results are more stable. In Fig. 2.10b, one further sees that interfacial shapes at $t = 0.168$ s (a time for which intense VS roll-up has occurred) are different, with and without gravity. In addition to reducing the maximum amplitude, gravity also slows down the roll-up process.

Influence of fluid density difference on growth rate of instability

The influence of the fluid density ratio $\varphi = \rho_o/\rho_1$ is tested next. In practice, for initially statically stable cases (i.e., those for which the lighter fluid lies above the heavier fluid), φ can vary within the whole range [0,1]. For instance, the first case corresponds to ocean surface waves for which the upper fluid is air and thus $\varphi \simeq 0$, and the second case corresponds to a stratified system with two nearly identical fluids moving at different velocities, as in the case of a stratified ocean.

The physical cases solved here with the numerical PCVS model have parameter values similar to the oil-water cases solved in the previous sections, with gravity $g = 9.8$ m/s^2 and density ratios first corresponding to a water-water case (1.00), and then to cases with increasingly lighter oils of successive density 0.95, 0.90, and 0.85. The numerical parameter values are identical to those used before. [Due to regridding, at time $t = 0.168$ s, the number of nodes has increased to 97, 86, 87 and 79, for each of the four cases, respectively.] For the parameter values of the last three cases, the linear critical velocity jumps are, ΔU_{cr} =0.14, 0.19, and 0.23 m/s, respectively. Hence, all three cases are expected to be strongly unstable for $\Delta U = 0.5$ m/s, the selected velocity jump in these experiments.

The effects of the density ratio on the KH instability are also related to inertial effects of momentum transfer from one fluid to the other, through the interface. From the linear theory predictions, it is expected that, as the density ratio φ decreases (i.e. as the density difference between both fluids increases), the interfacial instability growth rate should be reduced. For the nonlinear problems solved with the PCVS model, growth rates are also expected to be lower than for the corresponding linear cases. Knowing the exact magnitudes of growth rates as oil density changes is of interest in the larger context of studying the failure of oil containment by a boom as KH instability growth is closely related to the growth of the headwave region in front of the slick.

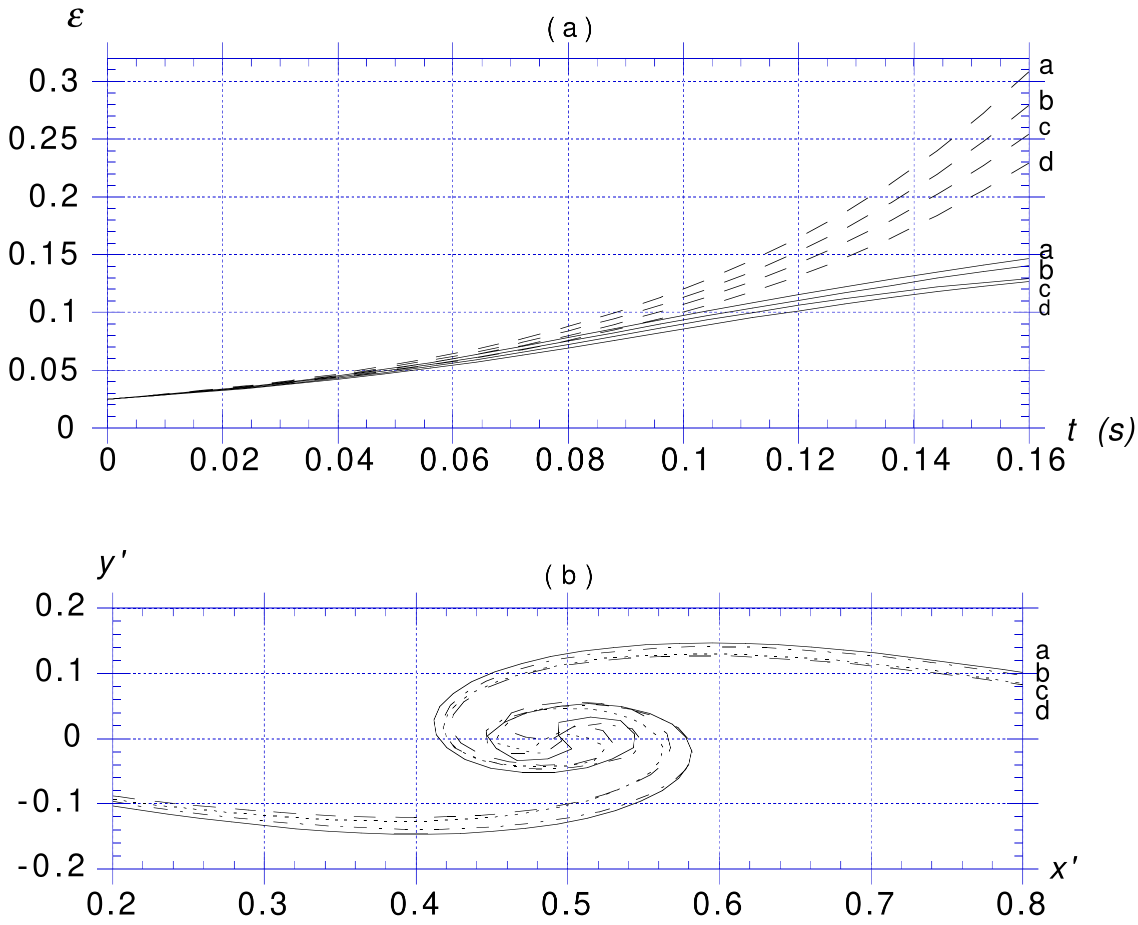

Figure 2.11: *Influence of density difference.* Computations of KH instability in a set-up similar to Fig. 2.3 with $\Delta U = 0.50$ m/s, $\lambda = 0.1$ m, $\sigma_{o1} = 0.0237$ N/m, $N = 45$, time step $\Delta\tau = 0.0001$, $g = 9.8$ m/s^2, and φ = a (———) 1.0; b (— - —) 0.95; c (- - - - -) 0.90; d (– – – –) 0.85. The initial perturbation is a sinusoidal wave with amplitude $\varepsilon = 0.025$ and vorticity distribution according to Eq. (2.28). (a) Maximum amplitude of interfacial disturbance compared to (— —) the linear growth rate (Lamb [26]). (b) Interfacial shape at $t = 0.168$ s.

Fig. 2.11 shows the numerical results. As expected, all model results in Fig. 2.11a show growth rates lower than predicted by linear theory. Further, as expected, the growth rate decreases for decreasing density ratios. In Fig. 2.11b, which compares free surface profiles at $t = 0.168$ s, one also sees that, in addition to the amplitude difference, the VS roll-up gradually slows as φ decreases.

Influence of interfacial tension on growth rate of instability

For an interface between two fluids, two boundary conditions have to be simultaneously satisfied. The first is that material fluid particles on both sides of the interface must stay in contact, and the second is that pressure on both sides of the interface must be identical. The former condition is kinematic and is automatically satisfied by the PCVS model governing equations. The second equation is dynamic and is also implicitly included in governing equations such as the vorticity updating Eq. (2.7). If surface tension effects are included in the computations, however, the pressure equilibrium equation is changed, as compared to a case with no surface tension. These effects indeed result in an additional term representing an equivalent pressure jump across the interface, expressed by, $\Delta p(s) = -\sigma_{o1}/R(s)$, where R denotes the radius of curvature along the interface, described by parameter s.

From this relation, it is seen that when the interface shape is concave upward (i.e. with a positive curvature), the pressure jump across the interface is negative, while for a concave downward interface, the pressure jump is positive. Hence, theoretically, surface tension is expected to flatten out fluctuations on the interface and thus to reduce the growth rate of KH instability. In the computational model, as soon as the interface starts rolling-up, the local interface curvature rapidly increases, which results in dramatic variations of local circulation, through surface tension effects in the vorticity updating Eq. (2.7). These variations, in turn, tend to limit the growth of interfacial waves. The computational tests in this section confirm these theoretical predictions.

As in the previous sections, the selected physical cases have parameter values corresponding to a realistic case with water and, in this case, a heavy oil of density 0.95, with the exception of successive values of the interfacial tension set to, $\sigma_{o1} = 0.0237$ N/m (standard oil-water value), 0.237 N/m (10 times this value), and 1.185 N/m (50 times this value). The numerical parameter values are identical to those used before. [Due to regridding, at time $t = 0.168$ s, the number of nodes has increased to 92, 78 and 64, for each of the three cases, respectively.] The numerical parameter values are identical to those used before. The numerical parameter values are identical to those used before. For the parameter values of the three cases tested, the linear critical velocity jumps are, ΔU_{cr} =0.14, 0.21, and 0.41 m/s, respectively. Hence, all three cases are expected to be unstable for the specified velocity jump, $\Delta U = 0.5$ m/s, although the third case with the largest interfacial tension, for which $\Delta U = 1.22\Delta U_{cr}$ should only have a fairly slow growth rate, particularly in the nonlinear regime.

Results in Fig. 2.12a confirm the expected dramatic effects of a large increase in interfacial tension on the growth rate of the instability. When surface tension is increased

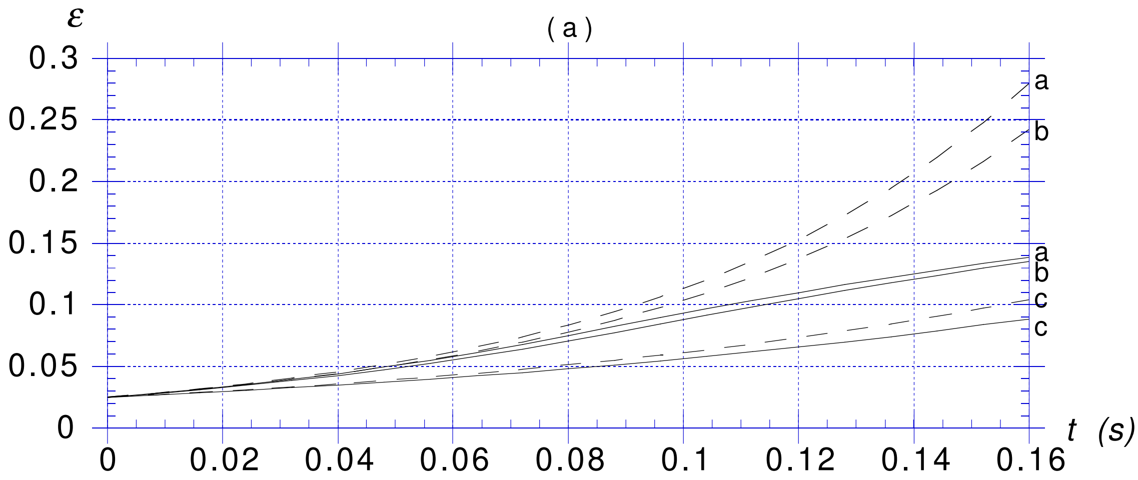

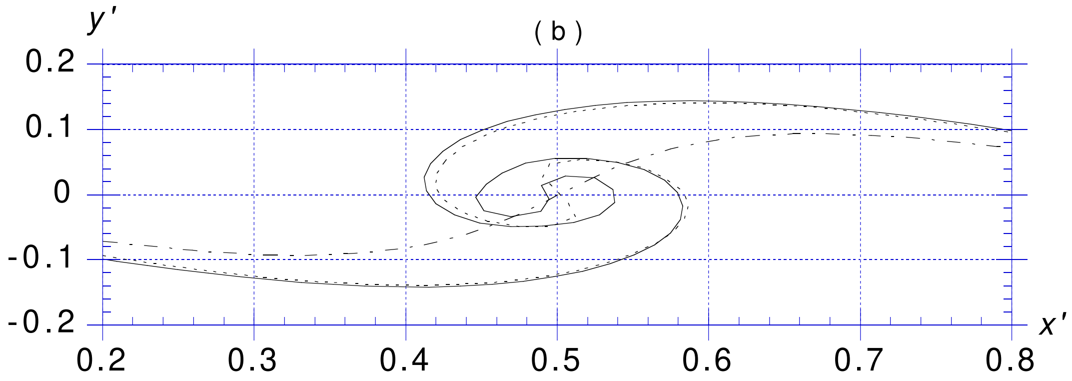

Figure 2.12: *Influence of interfacial tension.* Computations of KH instability in a set-up similar to Fig. 2.3 with $\Delta U = 0.50$ m/s, $\lambda = 0.1$ m, $\varphi = 0.95$, $N = 45$, time step $\Delta\tau = 0.0001$, $g = 9.8$ m/s^2, and σ_{o1} = a (———) 0.0237 N/m; b (- - - - -) 0.237 N/m; c (— - —) 1.185 N/m. The initial perturbation is a sinusoidal wave with amplitude $\varepsilon = 0.025$ and vorticity distribution according to Eq. (2.28). (a) Maximum amplitude of interfacial disturbance compared to (— —) the linear growth rate (Lamb [26]). (b) Interfacial shape at $t = 0.168$ s.

by a factor 50 (case c), the growth rate is almost reduced by half. Fig. 2.12b also shows the significant influence of surface tension on interfacial shape as calculated at time $t = 0.168$ s. An increase in surface tension, in addition to reducing the amplitude, strongly delays the development of KH instabilities.

It should be pointed out that, due to an insufficiently accurate geometric representation of the interface, such computations could not be performed with the Phase I model. In the present Phase II model, curvature and its derivatives are much more accurately calculated and the numerical instabilities experienced with Phase I model are thus eliminated.

Conclusions of KH instability studies

The preceding computations of interface evolution during KH instability clearly demonstrated and quantified how the interface amplitude growth depends on fluid properties and flow conditions. Throughout these computations, the improved Phase II periodic PCVS model performed very well and was thus validated as a tool for predicting interfacial behavior during KH instability. More specifically, using the PCVS model, it was found,

(i) in the presence of gravity, the interface is subjected to stabilizing effects from buoyancy forces and the disturbance growth is slowed as compared to an identical case when gravity effects are not included;

(ii) an increase in fluid density difference across the interface will result in reducing and slowing down the disturbance growth on the interface; the most unstable case is thus a case with two identical fluids ($\varphi = 1$) or, in the present case, the heavier oil;

(iii) and an increase in surface tension at the interface also results in reducing and slowing down the disturbance growth on the interface; this is because surface tension, to some extent, balances the circulation accumulation in the highly curved regions of the interface.

Based on the result in (ii), one can thus postulate that, for an oil slick contained by a boom, the headwave instability growth rate will be smaller and the instability will be delayed when using a lighter oil, compared to the case of a heavier (or weathered) oil. In laboratory experiments with oil/boom systems, it is observed that the oil-water interface, at first, rolls-up in the headwave region before pieces of the interface are torn off (e.g., Delvigne [9]). Therefore, based on the results in (iii), it is theoretically expected that, if surface tension is naturally (e.g., through weathering) or artificially (e.g., through chemicals) increased, the disturbance growth on the interface will be reduced and the interface break up and resulting containment failure will be accordingly delayed (or eliminated), hence, providing additional time for collecting oil at a given (unstable) relative velocity.

In the light of the above results, in subsequent studies, particularly during Phase III, the quantitative influence of density difference and surface tension on the oil-water interface evolution, will be studied for complete oil-boom systems.

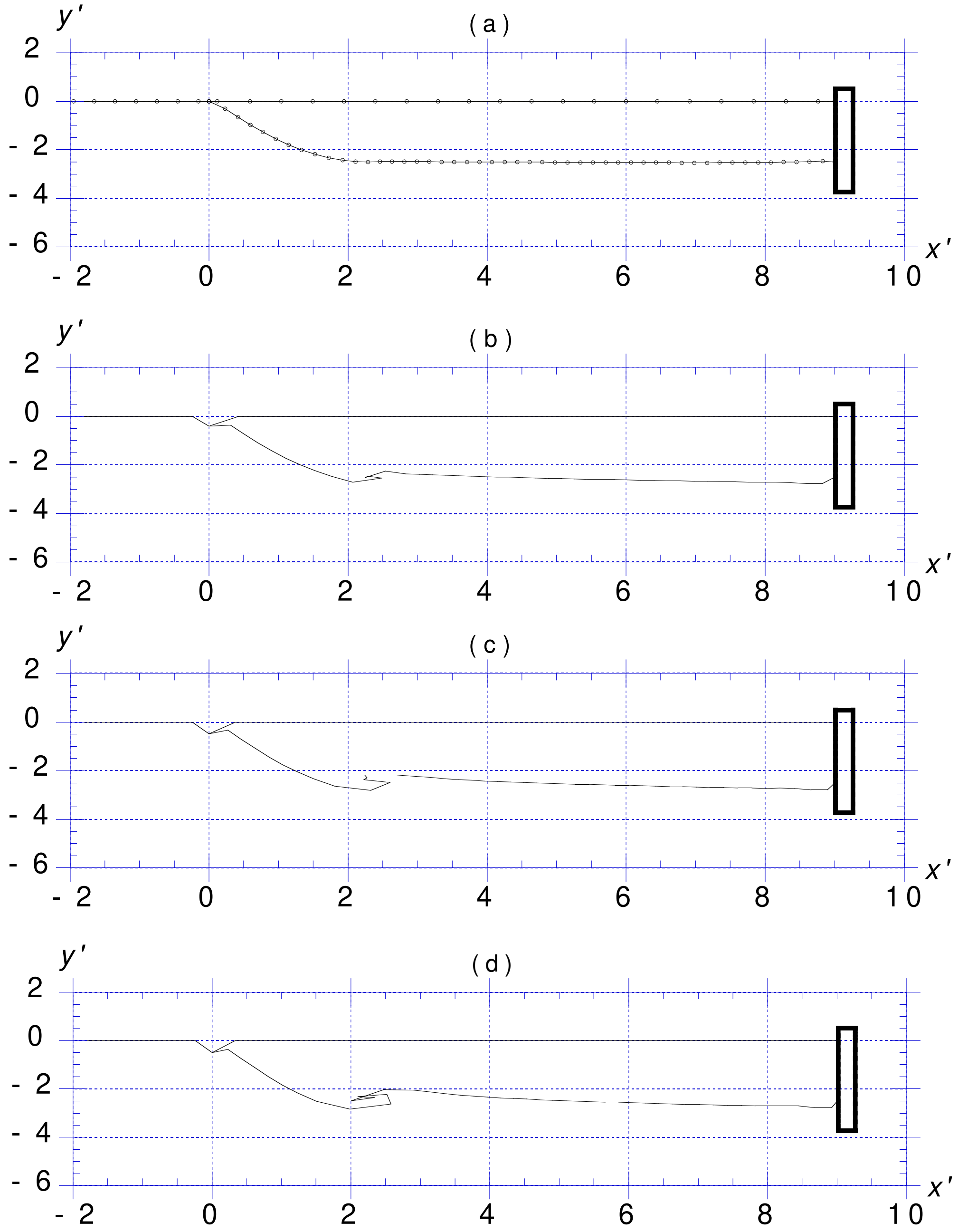

Figure 2.13: Computational results for oil/boom containment failure due to *headwave instability*, in a set-up similar to Fig. 2.4, with U_w = 0.14 m/s, $\varphi = 0.8$, $\lambda = 0.002$ m, and $\sigma_{ow} = 0.0237$ N/m (water-oil). Initial slick shape is computed using Eq. (2.43) and (2.44) : $H' = 2.5, L' = 9.08$. Three semi-infinite sheets and five PCVS's were used in the numerical model, with $N_1 = 10$, $N_2 = 50$, $N_3 = 20$, $N_4 = 21$, and $N_5 = 18$ vortex elements on each sheet, respectively. Shape of the slick at $\tau =$: (a) 0.18 ; (b) 0.67; (c) 0.75; and (d) 0.77; corresponding to 1, 61, 91, and 136 varying computational time steps, respectively. Boom draft is $d' = 1.5H'$.

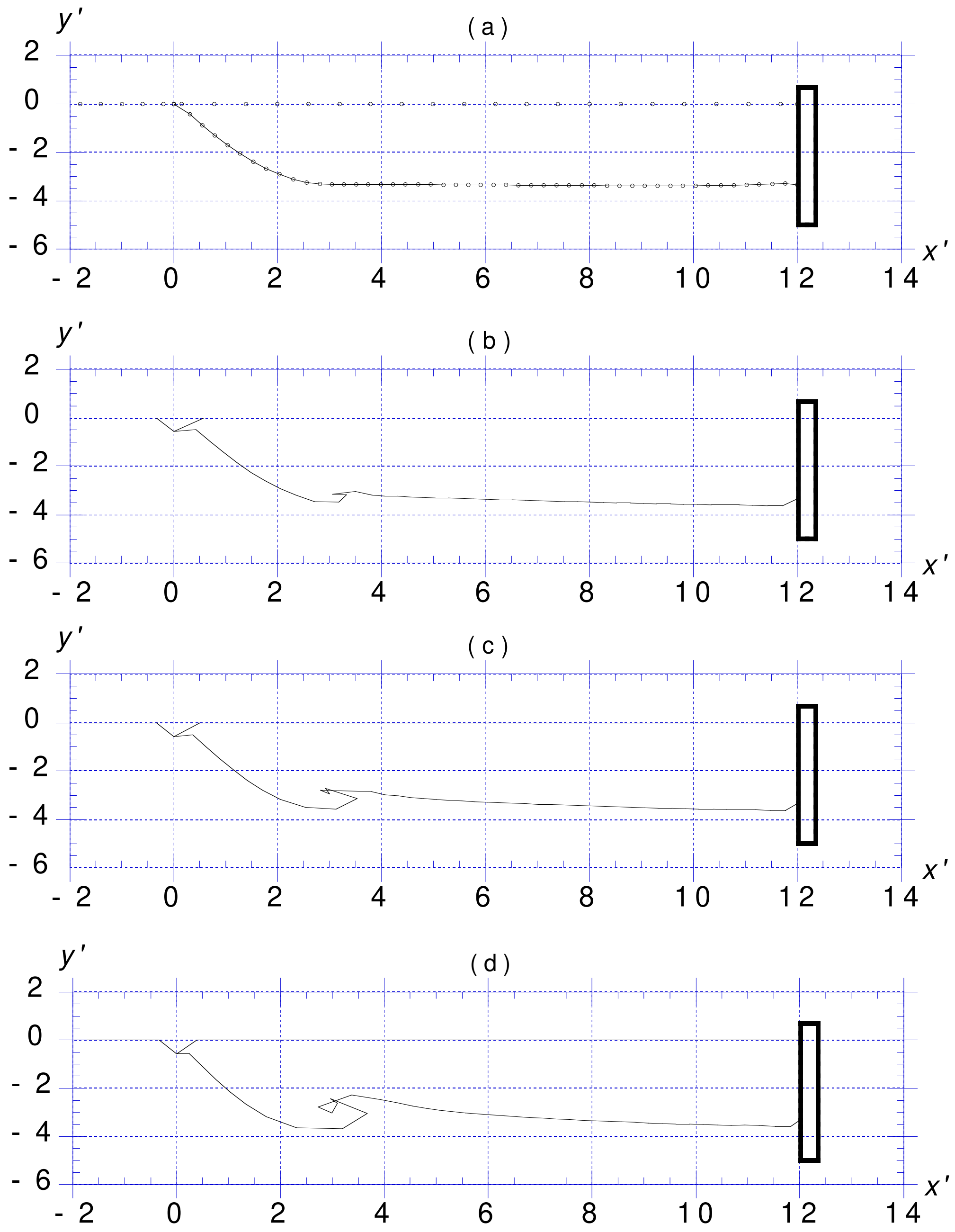

Figure 2.14: Same computations as in Fig. 2.13, with $\varphi = 0.85$, $H' = 3.33$, $L' = 12.1$. Shape of the slick at $\tau =$: (a) 0.24 ; (b) 0.87; (c) 0.92; and (d) 0.98; corresponding to 1, 46, 76, and 136 varying computational time steps, respectively.

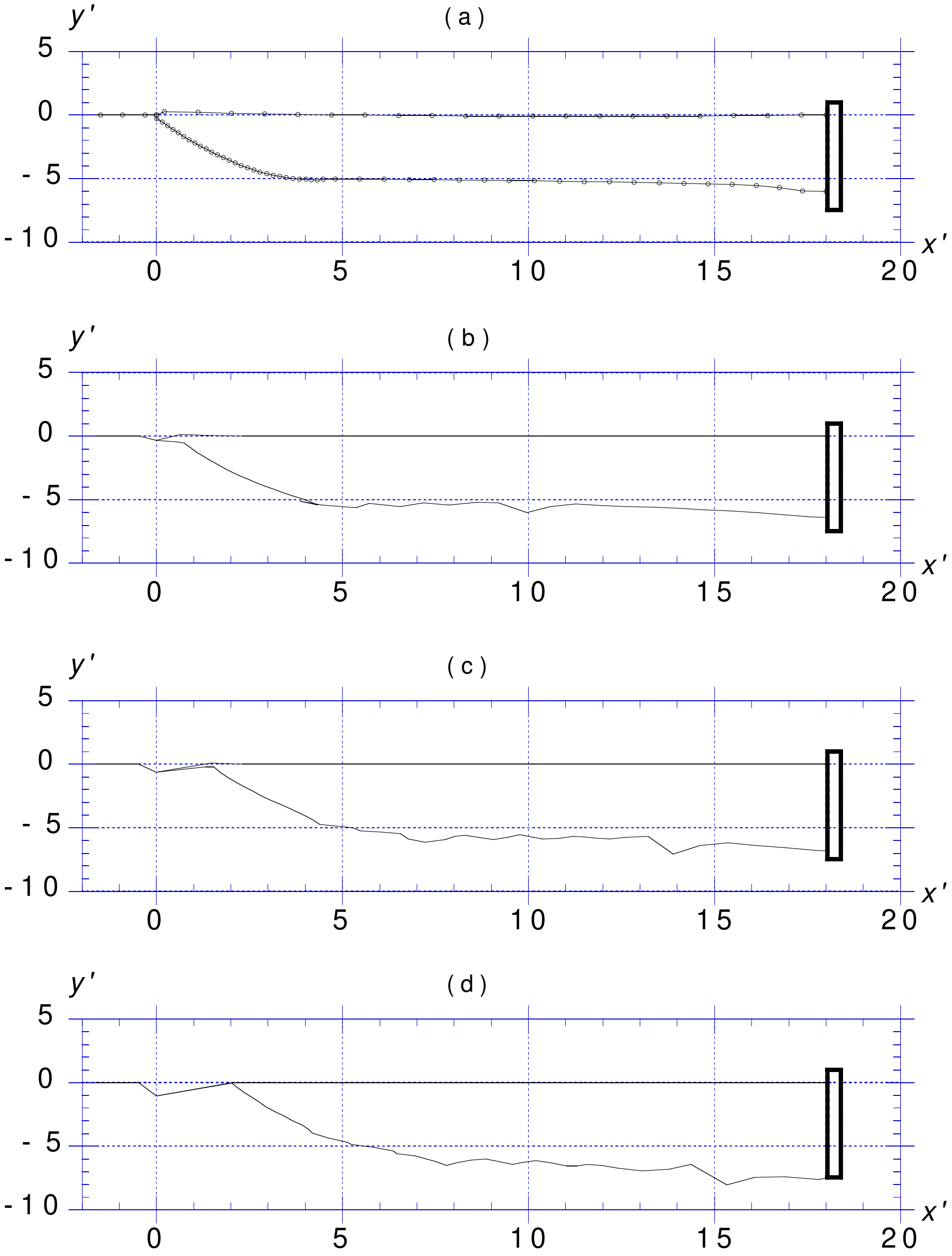

Figure 2.15: Unstable contained slick, with $\varphi = 0.90$, $U_w = 0.25$ m/s, $H' = 5.00$, and $L' = 18.2$. Shape of the slick at $\tau =$: (a) 0.36 ; (b) 2.12; (c) 3.35; and (d) 4.44; corresponding to 1, 226, 376, and 501 varying computational time steps, respectively. Numerical data are similar to cases in Figs. 2.13 and 2.14.

2.5.3 Application of the non-periodic PCVS model to oil containment by a boom

This case corresponds to the problem illustrated in Fig. 2.4. Two cases were first solved, for $\varphi = 0.8$ and 0.85, and U_w = 0.14 m/s, which gave a length scale $\lambda = U_w^2/g = 0.002$ m. The surface tension coefficient was specified to the oil-water value, $\sigma_{ow} = 0.0237$ N/m. The initial shape of the slick was calculated using Eqs. (2.43) and (2.44), which gave : H' =2.5, 3.33, the slick thickness; and L' =9.08, 12.1, the slick length, for each case, respectively (dashes denote nondimensional variables). The boom draft was set to $d' = 1.5H'$. The circulation at the oil-water interface was initialized using Eq. (2.45).

In the model, three semi-infinite sheets and five PCVS's were used, with $N_1 = 10$, $N_2 = 50$, $N_3 = 20$, $N_4 = 21$, and $N_5 = 18$ vortex elements on each discretized sheet, respectively (see Figs. 2.13a and 2.14a for a sketch of the initial discretizations and slick shape after one time step, for each case). No node regridding was used in these calculations. The initial time step was selected based on a mesh Courant number $\mathcal{C}_o = 0.5$. The time step was subsequently adjusted according to the relationship,

$$\Delta t = \mathcal{C}_o \frac{\text{Min} \mid \Delta s_i \mid}{\text{Max} \mid \Delta \boldsymbol{u}_i \mid} \tag{2.49}$$

where Min $\mid \Delta s_i \mid$ denotes the minimum length and Max $\mid \Delta \boldsymbol{u}_i \mid$ denotes the maximum velocity, of PCVS's on the oil-water interface. After experimenting with the model, it was found that, in order to preserve the stability of numerical results when headwave instability occurred on the oil-water interface, the Courant number had to be gradually reduced to 0.06.

Figs. 2.13 and 2.14 show, for both cases, the calculated shapes of the slick at various times, the first one corresponding to one time step (Figs. 2.13a, 2.14a). The specified velocity, for both cases, is slightly smaller than the linear critical velocity of KH instability, $\Delta U_{cr}^{min} = 0.17$ and 0.16 m/s, respectively. In both cases, as time increases, an instability develops in the front of the slick, and propagates downstream as a headwave which overturns and rolls-up on itself, in a way similar to KH instability waves calculated in Section 2.5.2. The slight trough observed in experiments at the front of the slick is well reproduced in the computations (e.g., Milgram and Van Houten [29]). As expected from the KH instability studies, the second case (Fig. 2.14) which has a heavier oil shows a more intense, larger relative size, headwave instability than the first case which has a lighter oil (Fig. 2.13). Both of these cases would physically correspond to containment failure by *oil entrainment*. Indeed, as the headwave rolls up, pieces of oil can be detached and entrained in the flow under the boom. This mechanism and the rate of oil entrainment was studied by Zalosh [42], on a semi-empirical basis, for a semi-infinite slick.

A third case is calculated in Fig. 2.15, for $\varphi = 0.9$ and a relative velocity $U = 0.25$ m/s, much larger than the linear critical velocity for the KH problem, $\Delta U_{cr}^{min} = 0.14$ m/s. In this case with a higher-speed relative velocity, the instability at the oil-slick interface starts just behind the front part of the slick, as a series of small scale waves (Fig. 2.15b) which propagate downstream towards the boom. In these waves, the leading oscillation is somewhat larger and grows even larger as it approaches the boom (Fig. 2.15c). As time increases and interfacial waves grow, the slick length decreases and the slick thickness increases. Eventually, at the end of the computations reported in the figure (Fig. 2.15d), the slick thickness at the boom is equal to the boom draft and oil is about to be entrained/drained under the boom. To calculate further than this stage with the model, the separation of vortex sheets from the boom leading edge should be implemented. This has not been done at the present stage. The results in Fig. 2.15, in which KH instabilities at the interface combined to the blockage effect at the boom lead to the unstable shortening and thickening of the slick, are typical of the oil containment failure mode referred to as *critical accumulation*.

These results show the ability of the PCVS model to predict the unstable shape of a contained oil slick. Although they appear to be qualitatively correct, they still use the empirical method by Zalosh [42] to estimate the *initial shape* of the slick, and also do not include *interfacial friction* effects which have an important influence on slick geometry and thickness. After integrating in this model the initialization of the slick shape, presented in Chapter 4, and the inclusion of frictional effects in the vorticity updating equation, presented in Chapter 5, more quantitatively realistic similar computations will be performed during Phase III, using the more accurate CVS model, presented in Chapter 3 for the velocity calculations. Model parameters will then be calibrated based on newly obtained experimental data.

Chapter 3

Periodic Continuous Vortex Sheet (CVS) model and applications to KH instability

In this chapter, a new more accurate model is proposed to compute the time evolution of the interface between two inviscid fluids moving with uniform velocity, subjected to instabilities of the Kelvin-Helmholtz (KH) type. In this model, the interface is represented by a Continuous Vortex Sheet (CVS), which both preserves the full nonlinearity of interfacial boundary conditions and provides a higher-order representation of the geometry and field variables than in the previously proposed models, like the PCVS models developed in Phase I and refined in Phase II, as presented in Chapter 2.

As in the PCVS models, time updating of CVS's geometry and circulation is calculated as a function of gravity, interfacial surface tension, and fluid density difference. To deal with the *hyper-singularities* occurring in Biot-Savart integrals Eqs. (2.1), describing CVS's velocity, when the observation point belongs to the vortex sheet, a new *intrinsic variable expansion* technique is proposed, which leads to an exact representation of CPV contributions to the BS equations.

The CVS model is applied to predicting the nonlinear growth of periodic KH instabilities in a two-fluid stratified system. Results demonstrate that the periodic CVS model provides both higher numerical accuracy and stability and gives a more accurate physical picture of the disturbance evolution than obtained when using the less accurate PCVS periodic model.

Based on these promising results, in future work to be conducted in Phase III, the CVS modeling approach will be applied to the oil/boom containment problem described in Section 2.4. As discussed in Chapter 1, however, to obtain a correct model of oil/boom containment, it will be necessary to first initialize the problem using the correct steady state slick shape, including friction effects (see Chapter 4), and using a vorticity updating equation that also includes interfacial friction effects in the CVS model (i.e., an additional term representing these effects will be added to Eq. (2.7) or (2.13); see Chapter 5).

In the following, Section 3.1 first gives an introduction to the numerical modeling of the KH problem, justifying the need for a more accurate and stable approach. Section 3.2 gives governing equations and Section 3.3 summarizes numerical procedures for the periodic CVS model. Finally, Section 3.4 gives numerical results for model validation and applications to the KH problem.

3.1 Introduction

Over the past few decades, many attempts were made to model the velocity of continuous VS's using Biot-Savart (BS) integral equations (2.1). In such studies, one conventional approximation has often been to discretize continuous VS's by a finite number of point vortices (e.g., Rosenhead [35]). Moore [31] thus developed a point-vortex method and successfully calculated roll-up of VS's. For stratified flows, Zalosh [43] similarly studied interfacial instabilities with a method that included effects of buoyancy and surface tension. Using a similar method, Rangel and Serignano [33] predicted the evolution of initially small periodic disturbances at the interface between two fluids of different density and velocity, including surface tension, but not gravity, effects.

Despite some success, such calculations usually resulted, after a large number of time steps, in non-physical chaotic motion of point vortices. Regridding methods, introduced for instance in [33], could reduce but not totally eliminate such instabilities. Problems experienced by point-vortex approximations of VS's can be categorized as follows :

(i) the numerical evaluation of singular CPV terms in BS integrals (2.1) is not properly handled by standard (regular) numerical integration techniques;

(ii) the VS evolution is improperly modeled at extremity points of the computational domain, defining either periodic boundaries or the intersection between the computational domain and infinite VS's or solid boundaries;

(iii) the geometric representation of VS's and of higher-order interfacial tangential derivatives, based on discretized points, is not sufficiently accurate as time develops;

(iv) results converge poorly or even diverge when the VS discretization is refined and/or when non-uniform point-vortex distributions are used.

All of the above problems are numerical, not physical, in nature and are related to specific aspects of discretization methods and calculation of BS integrals. Moore [31], in fact, showed that point vortex, and even PCVS approximations methods such as presented in Chapter 2, rapidly cause roundoff and truncation errors to amplify and lead to the reported chaotic motion which ruins practical calculations[1].

By a careful analysis of work published to date, Fink and Soh [14] showed that a point vortex representation implicitly neglects logarithmic terms representing local contributions (i.e., vortex self-induced velocity) to the BS integrals. Moore [32] further showed that a weak singularity does form, after a critical time, on the discretized VS. Accordingly,

[1]Note that both of these approximations have identical physical assumptions except that, in the latter, singular terms in the integrals are calculated for local constant VS elements.

the point-vortex approximation only converges up to this critical time. In agreement with Moore, Meiron *et al.* [30], solving a pure shear flow problem, found a curvature singularity of the VS. Krasny [24], using discrete Fourier analysis, proved that numerical perturbations due to roundoff errors are responsible for the observed irregular motion of point vortices. Baker and Shelley [3] examined the behavior of layered VS's, with regard to local sheet circulation induced by density and thickness changes, and showed that, beyond the critical time, the behavior of VS layers becomes irregular.

Due to the problems experienced by classical point-vortex approaches, many researchers pointed out the need for using higher-order VS representations that would reduce numerical errors and allow to better identify the physical mechanisms governing VS evolution.

In Phase I and II of this project, we addressed the four problems (i)-(iv) mentioned above, within the realm of a PCVS approximation (Chapter 2) and were able to successfully solve KH instability problems, for a wide range of parameter values (Section 2.5.2). To do so : (i) we accounted for the CPV integral contributions in Eq. (2.1); (ii) we both improved and extended periodicity conditions; (iii) we introduced a new stable and accurate higher-order representation of the geometry and tangential derivatives on the interface (parity mapping method); and (iv) we controlled model resolution by using an adaptive node regridding method, in combination with the parity mapping method. Despite the success of computations with both the periodic and non-periodic PCVS models, however, the piecewise constant approximation of vorticity that was made over VS elements in the model was shown to clearly limit both the accuracy and the time extension of computations, particularly in the most interesting case of oil containment by a boom (Section 2.5.3). This motivated the development and implementation of a more accurate model in which both the geometry and the circulation of VS are approximated by higher-order continuous polynomials. This model is hereafter referred to as the Continuous Vortex Sheet (CVS) model and its preliminary development and validation are presented in this chapter, by calculating periodic KH instabilities of a vertically stratified two-fluid system (as done in Section 2.5.2 for the periodic PCVS model).

3.2 Governing equation for the periodic CVS model

General equations governing the dynamic and rate of change of vorticity of VS's, due to gravity, surface tension, and density difference effects, were presented in Section 2.2. These equations are still applicable and will be used in the CVS model. General equations relative to the periodic KH instability problem presented in Section 2.3.1 are also applicable to the periodic CVS model. The governing BS integral equation for the velocity field and the time updating in the CVS model is given by Eqs. (2.35) and (2.36). In the present case, however, Eq. (2.36) will be integrated assuming a *higher-order spatial discretization* of both the VS geometry and circulation, based on isoparametric boundary elements (BEM; Brebbia, [6]).

As in the PCVS model, the CVS geometry over one wavelength λ is divided into M locally continuous elements, defined using a set of N discretization points. To optimize computations, each of these elements is mapped onto a single reference element, with intrinsic coordinate μ varying between -1 and 1. Summing up element contributions, the velocity induced at time τ, for points $i = 1, ..., N$ of coordinates (ξ_i, η_i), is obtained from Eq. (2.36) as (nondimensional variables (2.9)-(2.12) have been used),

$$\begin{aligned}
\mathrm{u}(\xi_i, \eta_i) &= \frac{1}{2} \sum_{k=1}^{M} \int_{-1}^{+1} \frac{\gamma(\mathrm{s}'(\mu)) \sinh 2\pi(\eta_i - \eta'(\mu))}{\cosh 2\pi(\eta_i - \eta'(\mu)) - \cos 2\pi(\xi_i - \xi'(\mu))} \frac{d\mathrm{s}^k}{d\mu}(\mu)\, d\mu \\
\mathrm{v}(\xi_i, \eta_i) &= -\frac{1}{2} \sum_{k=1}^{M} \int_{-1}^{+1} \frac{\gamma(\mathrm{s}'(\mu)) \sin 2\pi(\xi_i - \xi'(\mu))}{\cosh 2\pi(\eta_i - \eta'(\mu)) - \cos 2\pi(\xi_i - \xi'(\mu))} \frac{d\mathrm{s}^k}{d\mu}(\mu)\, d\mu
\end{aligned} \tag{3.1}$$

where γ, here, denotes the nondimensional circulation (with $d\mathrm{g} = \gamma d\mathrm{s}$), $d\mathrm{s}^k/d\mu$ is the (nondimensional) Jacobian of the transformation from element k to the reference element, and the time variable τ has been omitted for simplicity. Integrals in (3.1) will be calculated by numerical integration (see next Section).

3.3 Numerical methods for the periodic CVS model

In the present applications of the periodic CVS model, a cubic representation of both the geometry and circulation is used. At a given time t, BS Eqs. (3.1) are numerically integrated to calculate velocities along CVS's, using standard Gauss quadrature for the regular integrals (i.e., when point i does not belong to element k), and an intrinsic variable expansion technique is used to deal with the strong CPV singularities occurring in these integrals, as a result of self-induced velocity terms (i.e., when point i belongs to element k).

An explicit time stepping method, based on 2nd-order Lagrangian Taylor series expansions similar to those presented in Chapter 2 for the PCVS model (Eq. (2.18)), is used to calculate CVS's time evolution using velocities, accelerations, and rate of change of circulations calculated in the CVS model (the latter two being calculated as for the PCVS model).

General numerical procedures used in the periodic CVS model are identical to those given in Section 2.2 for the geometric modeling using the parity mapping method, the specification of end-point periodicity conditions, and the adaptive regridding in the PCVS models. The treatment of singular integrations in the BS Eqs. (3.1) is detailed in the following.

Singular integrations

The kernel of BS integrals (3.1) becomes strongly singular, for each element, when the observation node i coincides with one node of the integrated element k. The CPV of this integral must thus be properly evaluated. For a two-dimensional problem, as indicated by Eq. (2.1) or (2.35), the singularity is $\mathcal{O}(1/r_i)$, where r_i denotes the distance to point i.

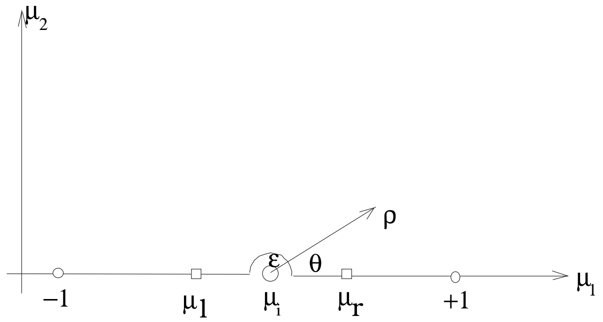

Figure 3.1: Sketch for the singular integration at point i of the reference element.

The integrand of BS Eqs. (3.1) can be defined as, $F(\mu) = N_j(\mu)J^k(\mu)f_i^{u,v}(\mu)$, where $f_i^{u,v}$ denotes one or the other kernels of the BS integral for u or v, $N_j(\mu)$ denotes shape functions (2.26) used to discretize the geometry and the circulation $\gamma = N_j\gamma_j$ on element k, and $J^k = s_\mu^k(\mu)$, the Jacobian. For each element, the strong singularity in the integrand can be represented by means of a Laurent series expansion around the singular point (x_i, y_i), of the form (Guiggiani *et* al. [15]),

$$F(\rho,\theta) = \frac{F_{-1}(\theta)}{\rho} + F_0(\theta) \tag{3.2}$$

where (ρ,θ) denote polar coordinates centered at point i in the reference element (Fig. 3.1), and $F_0(\theta)$ and $F_{-1}(\theta)$ are $\mathcal{O}(1)$ functions of the VS geometry around point i. The integrals in Eq. (3.1) for element k can now be expressed as (Fig. 3.1),

$$\begin{aligned} I^k &= \int_{-1}^{\mu_\ell} F(\rho(\mu),\theta(\mu))\,d\mu + \int_{\mu_\ell}^{\mu_r} F(\rho(\mu),\theta(\mu))\,d\mu + \int_{\mu_r}^{+1} F(\rho(\mu),\theta(\mu))\,d\mu \\ &= I_1^k + I_2^k + I_3^k \end{aligned} \tag{3.3}$$

where (μ_ℓ, μ_r) denotes an interval containing the singular point, located at μ_i. With this definition, only the middle integral, I_2^k is singular in Eq. (3.3). The first and last integral can thus be calculated using regular Gauss quadrature rule, after transformation of their respective intervals into [-1,+1].

When using the polar coordinates (ρ,θ), I_2^k, can be divided into three parts, by defining a semi-circular boundary of vanishing radius ϵ centered on the singular point, as,

$$\begin{aligned} I_2^k &= \lim_{\epsilon\to 0}\Big\{ -\int_{\mu_i-\mu_\ell}^{\epsilon} [\,\frac{F_{-1}(\pi)}{\rho} + F_0(\pi)\,]\,d\rho - \int_{\pi}^{0} [\,\frac{F_{-1}(\theta)}{\epsilon} + F_0(\theta)\,]\,\epsilon\sin\theta\,d\theta \\ &+ \int_{\epsilon}^{-\mu_i+\mu_r} [\,\frac{F_{-1}(0)}{\rho} + F_0(0)\,]\,d\rho \Big\} \\ &= F_{-1}(0)\ \ln\frac{\mu_r-\mu_i}{\mu_i-\mu_\ell} + \int_0^{\pi} F_{-1}(\theta)\ \sin\theta\,d\theta + (\mu_i-\mu_\ell)F_0(\pi) + (\mu_r-\mu_i)F_0(0) \end{aligned} \tag{3.4}$$

where, by definition of the geometry on the intrinsic element, $\mu = \mu_i + \rho\cos\theta$, and the property, $F_{-1}(\theta) = -F_{-1}(\theta+\pi)$ (which is a consequence of the residue theorem) has been used to combine the first (singular) terms in the first and last integrals [15]. If μ_ℓ and μ_r are selected symmetrically around point i, we further have,

$$\mu_i - \mu_\ell = \mu_r - \mu_i = \frac{\Delta\mu}{2} \tag{3.5}$$

with $\Delta\mu = \mu_r - \mu_l$, and, in this case, Eq. (3.4) simplifies into,

$$I_2^k = \int_0^\pi F_{-1}(\theta)\,\sin\theta\,d\theta + \frac{\Delta\mu}{2}\,[\,F_0(\pi) + F_0(0)\,] \tag{3.6}$$

The calculation of $F_0(\theta)$, $F_{-1}(\theta)$ in Eq. (3.6) first requires defining a local intrinsic coordinate expansion for, $\boldsymbol{x} - \boldsymbol{x}_i$, in the neighborhood of the singular point $\boldsymbol{x}_i$ (i.e., for small ρ), where $\boldsymbol{x}$ denotes another point of element k. Using the same polar coordinates system as above, we get,

$$\boldsymbol{x}(\mu) - \boldsymbol{x}_i(\mu) = \rho(\mu)\mathbf{A}(\theta(\mu)) + \rho^2(\mu)\mathbf{B}(\theta(\mu)) + \mathcal{O}(\rho^3) \tag{3.7}$$

with,

$$\mathbf{A}(\theta) = \frac{\partial\boldsymbol{x}}{\partial\mu}(\mu_i)\,C(\theta) \quad \text{with} \quad C(\theta) = \cos\theta - \tan\theta\sin\theta + \frac{\tan^2\theta}{2}\,[\,\frac{d\rho}{d\mu} - \frac{1}{\cos\theta}] \tag{3.8}$$

and,

$$\mathbf{B}(\theta) = \frac{\partial^2\boldsymbol{x}}{\partial\mu^2}(\mu_i)\,[\,\frac{\cos^2\theta}{2} + \sin^2\theta\,(\frac{\tan^2\theta}{2} - 1)\,] \tag{3.9}$$

where the first and second components of $\mathbf{A}(\theta)$ and $\mathbf{B}(\theta)$ refer to x and y coordinates, respectively.

Using Eqs. (3.7)-(3.9), we can express various parts of the kernel $F(\mu)$ of BS Eqs. (3.1) and put them in the form of expansion (3.2). After calculations, we get,

$$F_0^{u,v}(\theta) = a_o S_0^{u,v}(\theta) + a_1(\theta) S_{-1}^{u,v}(\theta) \quad ; \quad F_{-1}^{u,v}(\theta) = a_o S_{-1}^{u,v}(\theta) \tag{3.10}$$

where subscripts u and v indicate which of the two BS integrals (3.1) is being considered, and,

$$S_{-1}^{u,v}(\theta) = \frac{A_{2,1}(\theta)}{\pi(A_1^2(\theta) + A_2^2(\theta))} \quad ; \quad S_0^{u,v}(\theta) = \frac{B_{2,1}(\theta) - D(\theta)A_{2,1}(\theta)}{\pi(A_1^2(\theta) + A_2^2(\theta))} \tag{3.11}$$

where A_1, A_2, B_1 and B_2 are given by Eqs. (3.8) and (3.9), and

$$D(\theta) = 2\frac{A_1(\theta)B_1(\theta) + A_2(\theta)B_2(\theta)}{A_1(\theta)^2 + A_2(\theta)^2} \tag{3.12}$$

and,

$$a_o = s^k_\mu(\mu_i)\, N_j(\mu_i) \quad ; \quad a_1(\theta) = C(\theta)\,\{\, s^k_\mu(\mu_i)\, N'_j(\mu_i) + s^k_{\mu\mu}(\mu_i)\, N_j(\mu_i)\,\} \tag{3.13}$$

where μ indices and dashes indicate derivatives.

Accounting for relationships between odd and even functions of θ at 0 and π, the second term in Eq. (3.6) can now be calculated, using Eqs. (3.8)-(3.13) as,

$$\frac{\Delta\mu}{2}\,[\, F^{u,v}_0(\pi) \;+\; F^{u,v}_0(0)\,] = \Delta\mu\,[\, a_o S^{u,v}_0(0) + a_1(0) S^{u,v}_{-1}(0)\,] \tag{3.14}$$

with $\mathbf{A}(0) = \boldsymbol{x}_\mu$, $\mathbf{B}(0) = \frac{\boldsymbol{x}_{\mu\mu}}{2}$, $C(0) = 1$, and,

$$D(0) = \frac{x_\mu x_{\mu\mu} + y_\mu y_{\mu\mu}}{(s^k_\mu)^2} \tag{3.15}$$

and, hence,

$$S^{u,v}_0(0) = \frac{(y,x)_{\mu\mu}(s^k_\mu)^2 - 2(y,x)_\mu\,(x_\mu x_{\mu\mu} + y_\mu y_{\mu\mu})}{2\pi\,(s^k_\mu)^4} \quad ; \quad S^{u,v}_{-1}(0) = \frac{(y,x)_\mu}{\pi(s^k_\mu)^2} \tag{3.16}$$

Using Eqs. (3.10), (3.13) and (3.16), one can analytically calculate the integral in Eq. (3.6) and see that it vanishes. Using Eqs. (3.6) and (3.14), together with Eq. (3.16), one can then, after some transformations, calculate the singular part of Eq. (3.3) as,

$$I^k_2 = \frac{1}{2\pi\, s^k_\mu(\mu_i)}\,[\, N_j(\mu_i)\,(y(\mu_i), x(\mu_i))_{\mu\mu} + 2N'_j(\mu_i)\,(y(\mu_i), x(\mu_i))_\mu\,] \tag{3.17}$$

for the first and the second BS integrals, respectively.

Finally, all terms are expressed as a function of element shape functions and nodal values, using Eqs. (2.19)-(2.21).

3.4 Applications of the periodic CVS model

3.4.1 Validation with a uniform flow

To validate the new integration methods developed for the CVS model, a steady-state case was first solved, with a simple uniform flow U between two impermeable boundaries separated by a distance h (Fig. 3.2). Two CVS's with zero amplitude ($\varepsilon = 0$) were discretized over a length equal to $\alpha = 10$, 100, or 1000 times their spacing, $\lambda = \alpha h$. Since this problem was solved with the periodic model, no semi-infinite sheets were needed at the CVS's extremities. The number of nodes on the sheets was kept constant equal to 45. To model a uniform velocity U, circulation was set to $\pm U$ on each CVS, respectively. Twenty Gauss integration points per element were used in the CVS model. Velocity was calculated with the model, using BS Eqs. (3.1), first on the VS's nodes themselves, then for 30 equally

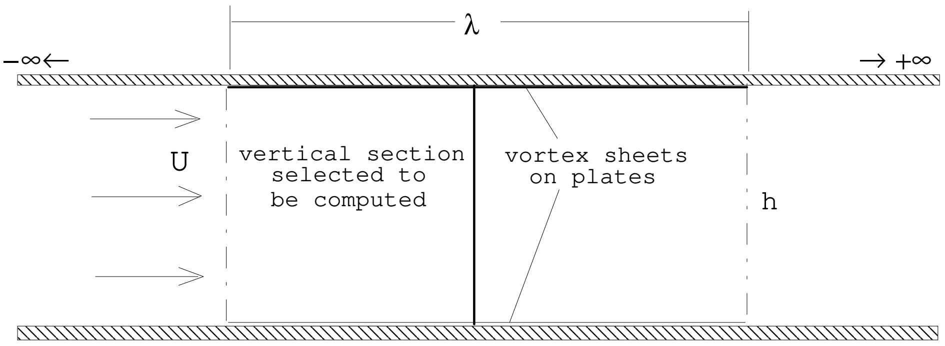

Figure 3.2: Sketch of computational domain for uniform flow between two plates

spaced points in between the VS's (Fig. 3.2). For comparison, similar computations were also performed using the PCVS periodic model described in Chapter 2.

On the VS's themselves, using the CVS model, the velocity was recalculated to within 4, 6.8, and 52.6 10^{-6}% of the exact value U, for $\alpha = 10$, 100, and 1000, respectively. Using the PCVS method, maximum errors were 3.8 10^{-4}, 12.6, and 612 %, respectively. In all cases, maximum errors occurred at the VS's extremities. The very accurate results obtained with the CVS model validate the singular numerical integration procedures developed for this model. In between the sheets, errors were significantly larger, with a maximum for the points closer to the VS's. For the CVS method, maximum errors reached 1.4 10^{-6}, 3.6 10^{-2}, and 6.3 % of the exact value U, for $\alpha = 10$, 100, and 1000, respectively. As for calculating the velocity on the sheets, in these calculations, (regular) integrations over vortex sheet elements were performed using 20 Gauss points. As internal points get increasingly closer to the VS's, however, BS integrals (3.1), though still regular, become almost singular (i.e., *quasi-singular integrals*, Grilli and Subramanya [19]). When increasing the number of Gauss points in these integrals, by subdividing the elements, as in [19], an accuracy similar to the first case ($\alpha = 10$) could be reached for the last two cases with the larger aspect ratio α. By contrast, using the PCVS method, accuracy stayed very poor in all cases, with errors of 32, 665, and 7448 %, respectively.

These results show the need for the more accurate CVS model when computational nodes get very close to each other and/or aspect ratios are large. As this will be the case for contained oil slicks, it is expected that more accurate and stable results will be obtained when using the CVS method, as compared to the PCVS method.

As a further validation of the CVS method, in the next section, an unsteady KH instability case is presented.

3.4.2 Periodic KH instability

The periodic KH instability of a two fluid vertically stratified system will be solved with the CVS model, in a set up similar to Fig. 2.3. A sinusoidal perturbation with small nondimensional amplitude ε is prescribed on the interface, and the initial circulation $\gamma(x)$ is specified using Eq. (2.28).

A (very unstable) pure shear flow problem is first considered, with a velocity jump $\Delta U = 0.5$ m/s applied between two layers of an identical inviscid fluid of uniform density ρ (whose absolute value has no influence in the present case), i.e., $\varphi = 1$. The amplitude of perturbation is $a = 0.0025$ m and the wavelength is selected to $\lambda = 0.1$ m, corresponding to an instability at the ripple scale; the wavelength however does not matter in this problem and results would be self-similar for another wavelength. Thus, with these data, $\varepsilon = a/\lambda = 0.025$ (as for the PCVS applications in Section 2.5.2). For, $W = \kappa = \sigma_{o1} = 0$, Eq. (2.32) shows that the linear growth rate of instability for this case is $\omega = k\Delta U/2$ and, in Eq. (2.7), we see that $d\gamma/dt = 0$. Hence, as expected for this case, the CVS system is conservative.

The initial discretization in the computations has $N = 45$ equally spaced nodes per wavelength and nodes are added and regridded at each time step, in order to maintain the node resolution constant to within 1.5%, as the CVS length increases when the instability develops. In order to ensure high accuracy in these very unstable computations, the initial time step is selected as a small value, $\Delta\tau = 0.001$ (note, in this case, $\tau = \Delta t\,\Delta U/\lambda = 5t$), which corresponds to a mesh Courant number of 0.023. Since the spatial resolution is maintained constant through regridding, the time step also stays constant throughout computations. Model results for the time evolution of the interface for 3,000 time steps are given in Fig. 3.3. At the end of computations, the number of nodes has increased to $N = 328$ (Fig. 3.3.g, curve h).

Overall, results show reasonable predictions of VS evolution. Fig. 3.3a shows that, for small time, the interface perturbation slowly grows up while more or less preserving its initial shape; hence, this is referred to as a *quasi-linear* regime. At the same time, a relative motion of crests is observed; this phenomenon, which is not observed in point-vortex or PCVS models (e.g., Rangel and Serignano [33]; Section 2.5.2), indicates that, as the instability develops, interfacial waves travel at a modified phase velocity. In Fig. 3.3b it is seen that, after the quasi-linear initial growth, the larger nonlinearity in the flow field leads to both increased wave amplitude and skewness and, eventually, to a crest overturning similar to surface wave breaking; this is referred to as the *nonlinear* regime. Comparing Figs. 3.3a and 3.3b, it is apparent that, for the same time interval of 0.6, the amplitude growth is much larger in the nonlinear regime than in the quasi-linear one. In Fig. 3.3c, the similarity of results with surface waves disappears as the interface VS starts *rolling -up*. In Figs. 3.3d-f, as time further increases, the interface roll-up becomes more pronounced. It is worth pointing out that PCVS computations such as those presented in Section 2.5.2 usually fail around the stage of Fig. 3.3d, whereas the more accurate CVS model provides very stable results for the full stages of development of VS roll-up.

After reaching a maximum value in Fig. 3.3f, Figs. 3.3g and 3.3h show that the amplitude of disturbance starts gradually decreasing, as the "roll-up cells" become more elongated. At this stage, however, it should be pointed out that different fluid regions in the roll-up cells are quite close to each other. Although not creating actual singularities in the flow, such situations lead to highly varying kernels in the BS integrals that standard Gauss quadrature rules fail to properly integrate unless a prohibitive number of integration points is used. Such integrals, referred to as *quasi-singular*, thus require more accurate integration methods, usually, as the distance between an observation node i and an element k becomes smaller than, say, 10% of the element length (Grilli and Subramanya [19]). Quasi-singular integration methods have not yet been implemented in our model but will be implemented as part of Phase III studies. Hence, although no particular instability is observed, one might start questioning model accuracy at and beyond the stage of Fig. 3.3h.

A second application was carried out for a case with two fluids of different density, $\rho_1 = 0.9$ and $\rho_2 = 1.0$, with surface tension coefficient equal to $\sigma_{o1} = 0.0237$ N/m (the value for water and oil). The gravitational acceleration was $g = 9.81$ m/s^2. Other parameters, both physical and numerical, remained as before. Fig. 3.4 shows that the disturbance amplitude, ε, growths as a function of time, for both applications, compared to predictions of linear theory from Eq. (2.32). For both cases, as also observed in earlier studies, linear theory greatly overpredicts the growth rate of the instability. As expected from PCVS computations in Section 2.5.2, an increase in interfacial surface tension and a decrease in the upper layer density both reduce the growth rate of nonlinear instabilities. In Fig. 3.4, one can also see that, for $\varphi = 0.9$, the interface amplitude eventually stops growing and oscillates around a more or less stable shape of amplitude $\varepsilon \simeq 0.05$. Hence, this case is not unstable in long term computations.

A comparison of the CVS growth rates with those predicted by the PCVS model for the same case (Fig. 2.11 curves a and c) show that the CVS model predicts smaller growth rates than the PCVS model. Fig. 3.5 in fact shows a comparison of interface shapes obtained in the PCVS and in the CVS model for the same case as in Fig. 3.3, and $t = 0.21$ s. [Beyond this time, PCVS results in Section 2.5.2 became unstable.] It is seen that the PCVS model predicts a faster growth of instability than the CVS model. Reasons for the observed differences reside in both a more accurate computation of BS integrals and a better geometric representation in the CVS model. A more detailed understanding of these results, however, still needs to be achieved.

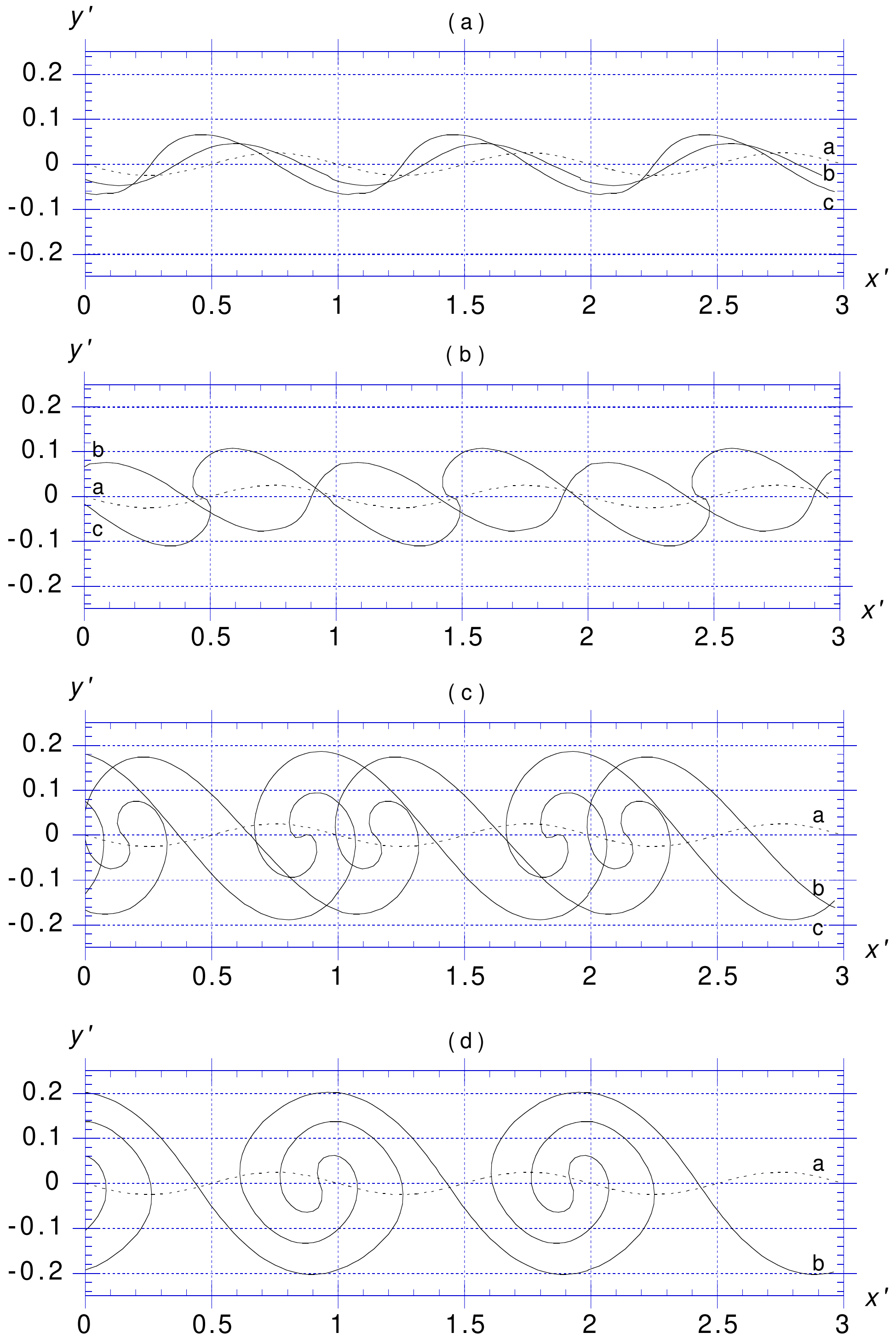
(a)
(b)
(c)
(d)
y'
x'
0.2
0.1
0
-0.1
-0.2
0
0.5
1
1.5
2
2.5
3
a
b
c

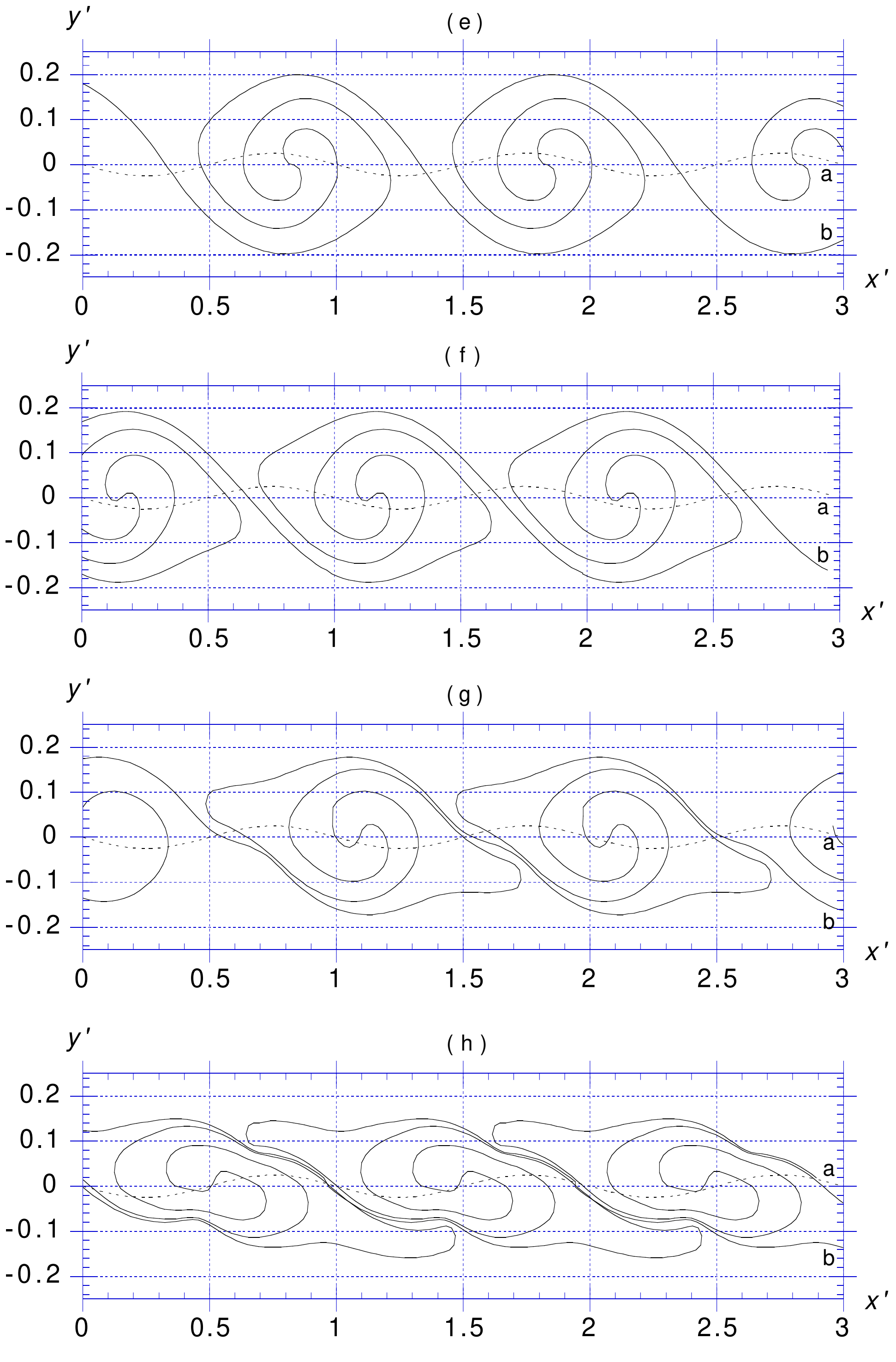

Figure 3.3: Results for periodic KH instability with wavelength $\lambda = 0.1$m, $|\ \Delta U\ | = 0.5$m/s, $\varphi = 1$, and $\sigma_{o1} = 0$. curves show interfacial shape at time t (s) = (a) a : 0.0002, b : 0.060, c : 0.120; (b) a : 0.0002, b : 0.150, c : 0.240; (c) a : 0.0002, b : 0.330, c : 0.390; (d) a : 0.0002, b : 0.480; (e) a : 0.0002, b : 0.510; (f) a : 0.0002, b : 0.540; (g) a : 0.0002, b : 0.570; (h) a : 0.0002, b : 0.600.

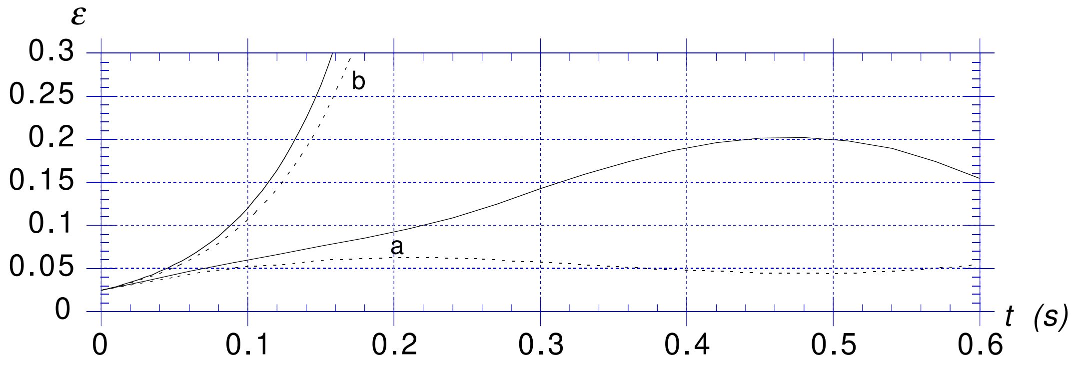

Figure 3.4: Periodic KH instability with wavelength $\lambda = 0.1$m and $\mid \Delta U \mid = 0.5$m/s : (——) $\varphi = 1$, $\sigma_{o1} = 0$; (- - - - -) $\varphi = 0.9$, $\sigma_{o1} = 0.0237$ N/m. Curves show the maximum dimensionless amplitude of the interface ε as a function of time t for : (a) CVS model; and (b) linear theory (Lamb, 1932).

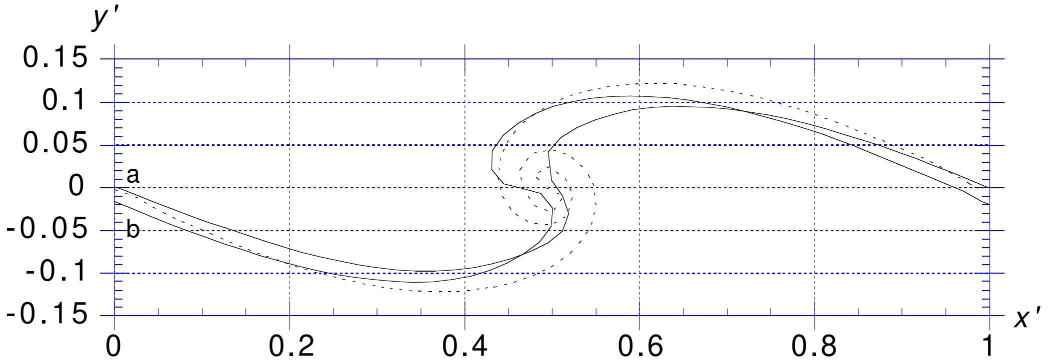

Figure 3.5: Same case as Fig. 3.3 : (——) CVS results for (a) $t = 0.210$ s, (b) $t = 0.240$ s; (- - - - -) PCVS results for $t = 0.210$ s.

3.5 Conclusions of CVS computations

A continuous CVS model was proposed for calculating the nonlinear motion of the interface between two inviscid stratified fluids. A BEM methodology was followed to develop higher-order representations of the discretized geometry and circulation in the CVS, which were used to calculate BS integrals for the velocity field. To optimize computations, local integrations of CVS elements were performed in a single reference element. The parity mapping transformation of Section 2.2.1 was used to more accurately calculate tangential derivatives in roll-up regions of the CVS. Hypersingular integrations were performed in the reference element, through a newly developed Laurent series expansion method. After testing the model for a simple uniform flow, the classical periodic Kelvin-Helmholtz instability problem was calculated to validate the new CVS model. Numerical results indicate that : (i) the CVS approximation provides a more accurate and stable numerical solution of the interface time evolution than when using the PCVS model; (ii) the CVS model eliminates the chaotic motion of interface points observed in classical point vortex or piecewise constant VS models, when computations are pushed beyond a critical time. We believe that such chaotic motions may be caused by both inaccuracies in the calculation of BS integrals and improper modeling of VS roll-up when using point vortices; (iii) the time evolution of CVS's significantly differs from the one calculated with point vortices or PCVS's. Besides a different growth rate of instability, disturbance waves in the CVS move with a specific phase velocity, larger than the VS's average velocity. Hence these waves are traveling rather than standing waves, with respect to the VS. The importance of both of these differences depends on fluid physical properties, velocity, and density difference; (iv) computations of the later stages of CVS evolution indicate that the KH disturbance growth levels up and then decreases. This is likely due to larger deformations in the roll-up regions of the VS, which start tightly spiraling and tilting to the downstream direction, implying that, after this stage, nonlinearity begins to play a more dominant role and prevents further disturbance growth. Instead, energy exchange and redistribution will occur by splitting or reuniting of roll-up sections, inside the VS itself.

During Phase III studies, the CVS model will be applied to the non-periodic oil/boom containment problem.

Chapter 4

Computation of quasi steady-state slick shape

4.1 Introduction

In the few computations of headwave instability published earlier, the initial shape of the oil slick was selected rather arbitrarily. Zalosh [42] for instance used part of a sine function to define the initial slick shape in his computations. This was also the method used in our Phase I model to initialize the shape of the oil slick (see Grilli *et al.* [16] for detail).

Based on the analysis of the oil containment problem done during Phase I of these studies, we concluded that such an arbitrary choice of initial slick shape (and dynamics) in the numerical model could induce non-physical (numerical) instabilities of the slick. An arbitrary (initial) geometry selected to represent the interface between oil and water, indeed, is not likely to satisfy both the kinematic and dynamic boundary conditions along the interface. Such a violation of the kinematic and dynamic equilibrium conditions is similar to creating an initial perturbation on the interface which, when introduced in a time dependent dynamic model, readily tries to adjust its shape to satisfy the equilibrium conditions. It is likely that such adjustments do not match actual instabilities occurring along an initially stable interface, for which the underlying current velocity is increased beyond the instability threshold U_{cr}.

In the Phase I studies, only simple cases were solved in order to qualitatively validate model equations and numerical procedures (i.e., Kelvin-Helmholtz and headwave instabilities). In those computations, the initial shape of interfaces was quite arbitrarily selected the same as in Zalosh's studies.

In the more sophisticated applications of the model to oil containment by a boom that we started to perform in Phase II of this study and for those currently taking place in Phase III, before interfacial instability can be studied in the VS model, it is necessary to calculate an initially stable shape of the oil slick interface. This shape must correspond to a small underlying current velocity, below the instability threshold $U < U_{cr}$. After this initialization stage, current velocity will then be increased beyond the instability threshold

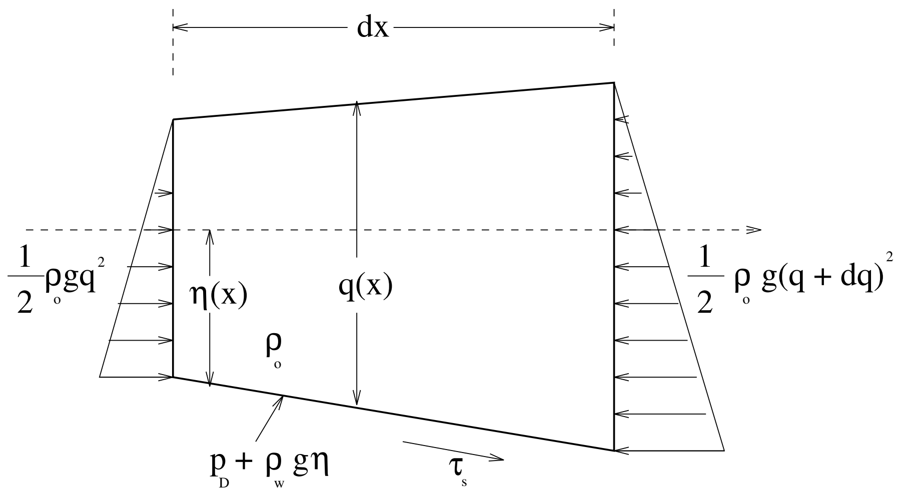

Figure 4.1: Sketch of forces acting on a differential element of length dx of the oil slick as in Milgram and Van Houten's [29] quasi-hydrostatic model.

and development of interfacial waves will be calculated as a function of time using the numerical VS model.

Initialization thus consists in finding the initial quasi-static shape of the slick interface $\eta(x)$ (measured from still water level; Fig. 4.1) that satisfies both the dynamic and kinematic conditions on the interface. In Phase I studies, Grilli *et al.* [16], following Milgram and Van Houten [29], proposed to use a quasi-hydrostatic approach within the slick to express equations for the initialization of the slick. This led to a numerical procedure to iteratively calculate the initial slick shape. No model, however, was developed at that time and no numerical results were presented.

During Phase II, the equations and numerical procedures proposed during Phase I to calculate the initial slick shape were further developed and implemented as a numerical Boundary Element Model (BEM) coupled to a finite difference iterative solver. These developments, as well as numerical applications of the BEM model, are presented in the following.

No integration of this model with the VS model, however, has been done during Phase II. Indeed, to fully integrate both BEM and VS models, it is necessary to first include interfacial friction effects in the VS time updating equations. Friction effects were theoretically worked out during Phase II (see Chapter 5), but will only be implemented as part of the calibration studies being carried out during Phase III. Integration of both models will then take place (see Fig. 1.5).

4.2 Principle of slick shape initialization

The basic quasi-hydrostatic equations for the slick shape initialization are first summarized.

Following [29], the oil slick is assumed not to significantly move and, hence, to be in quasi-hydrostatic equilibrium. Accordingly, a Bernoulli equation can be expressed between the front of the slick and any point on the slick interface, which provides the dynamic pressure p_D as (Fig. 4.1),

$$p_D = \frac{1}{2}\rho_w \left(U^2 - U_{ws}^2\right) \tag{4.1}$$

where ρ_w denotes the water density and U_{ws} is the water tangential velocity along the slick interface.

Expressing the horizontal force equilibrium along the interface we get, limiting terms to first-order,

$$\left(p_D + \rho_w g\, \eta\right)\frac{\partial \eta}{\partial x} + \tau_s = \rho_o g\, q\, \frac{\partial q}{\partial x} \tag{4.2}$$

where τ_s is the shear stress along the slick, q is the the total slick thickness (i.e., η plus the part above still water level; see Fig. 4.1). Expressing the vertical force equilibrium along the interface, we also get, limiting terms to first-order,

$$p_D + \rho_w g\, \eta = \rho_o g\, q \tag{4.3}$$

The shear stress along the slick is classically represented using a simple drag formula as (e.g., Batchelor, 1967),

$$\tau_s = \frac{1}{2}\rho_w\, C_f\, U_{ws}^2 \tag{4.4}$$

where C_f is a global non-dimensional friction coefficient, and a function of flow characteristics in the water and roughness along the interface.

In Milgram and Van Houten's study, the interface shape $\eta(x)$ and slick thickness $q(x)$ were experimentally measured and the tangential velocity of the underlying flow was calculated using ideal flow theory, assuming a uniform velocity U for the incident flow ahead of the slick. The friction coefficient (the only "unknown" left in the equations) was then calculated along the interface using Eqs. (4.1)-(4.4).

During Phase II of the studies, we developed a model based on the above equations and used it in reverse mode, i.e. : the friction coefficient C_f was calculated along the interface using boundary layer semi-empirical theories and the quasi-steady slick shape was then predicted. Since C_f is a function of *a priori* unknown flow characteristics (e.g., Reynolds number), an iterative method was used :

(i) an initial slick shape was assumed following Zalosh's [42] approximation;

(ii) the tangential velocity along the interface was calculated for the external water flow, based on ideal flow theory;

(iii) the friction coefficient was calculated for this external flow; and

(iv) a corrected slick shape was estimated using the quasi-hydrostatic equilibrium equations.

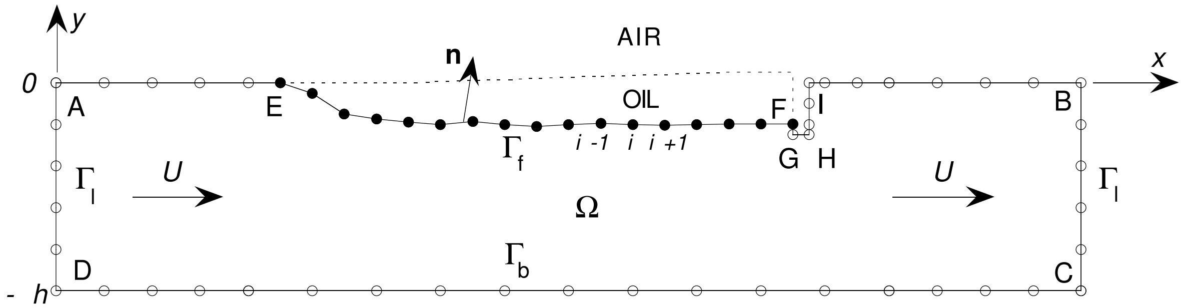

Figure 4.2: Sketch of computational domain Ω and boundaries Γ_f, Γ_l and Γ_b for the external water flow computation using streamfunction theory and the BEM model. Boundaries Γ_f and Γ_b are rigid no-flow boundaries and a uniform flow U is specified on Γ_l boundary. Discretization nodes ($\circ$) and ($\bullet$) are used in the BEM solution of the water flow and locations of nodes ($\bullet$) on the slick interface are iteratively calculated to satisfy equilibrium equations. Nodes A-I are double nodes in the BEM computations. Nodes marked as $i-1, i, i+1$, illustrate the finite difference iterative method.

These steps were repeated until convergence was reached on the slick geometry.

More details are provided in the following Sections for stages (ii) to (iv) of the iterative method. Results from this iterative method are presented in the last section and compared to experimental results [29].

4.3 External flow calculation

In the slick quasi-hydrostatic equilibrium equations presented above, the effect of the underlying water flow is transmitted through both the dynamic pressure and the shear stress at the interface. Both of these, essentially, depend on the water flow velocity at the interface represented by the tangential velocity U_{ws}, and on the interface geometry.

Since the slick is assumed not to move, the water flow is considered as an external flow past an obstacle having the slick/boom geometry. Hence, the free surface in front of the slick and behind the boom, together with the water/slick interface and the boom, are assumed to be rigid walls (i.e. streamlines) (Fig. 4.2). Due to the slenderness of the slick geometry, an ideal flow approximation, implying no flow separation, is made for the water flow. This will create some errors downstream of the boom where flow separation occurs but should not influence the slick shape too much, particularly in the headwave region.

Hence, using a streamfunction representation in the water domain Ω (e.g., Batchelor, 1967), continuity equation reads (Fig. 4.2),

$$\nabla^2 \psi = 0 \quad ; \text{in } \Omega \tag{4.5}$$

where ψ is the streamfunction defined such that,

$$u_w = -\frac{\partial \psi}{\partial y} \qquad ; \ v_w = \frac{\partial \psi}{\partial x} \qquad ; \ U_{ws} = -\frac{\partial \psi}{\partial n} \tag{4.6}$$

where (u_w, v_w) are velocity components in the water and $\boldsymbol{n}$ denotes the normal direction along the slick interface pointing outwards from the water (Fig. 4.2). Eq. (4.5) is solved using a Boundary Integral Equation representation (BIE),

$$\alpha(\boldsymbol{x}_l)\psi(\boldsymbol{x}_l) = \int_{\Gamma(\boldsymbol{x})} [\frac{\partial \psi}{\partial n} G(\boldsymbol{x}, \boldsymbol{x}_l) - \psi \frac{\partial G(\boldsymbol{x}, \boldsymbol{x}_l)}{\partial n}] \, d\Gamma(\boldsymbol{x}) \tag{4.7}$$

in which,

$$G(\boldsymbol{x}, \boldsymbol{x}_l) = -(1/2\pi) \log \mid \boldsymbol{x} - \boldsymbol{x}_l \mid \tag{4.8}$$

is the free space Green's function, $\boldsymbol{x} = (x, y)$ and $\boldsymbol{x}_l = (x_l, y_l)$ represent position vectors for points on the boundary Γ, and $\alpha(\boldsymbol{x}_l)$ is a geometric coefficient.

The BIE (4.7) is solved using a higher-order Boundary Element Method (BEM) (Grilli and Subramanya 1995, 1996), together with boundary conditions expressing no-flow on the bottom boundary Γ_b and on the free surface, slick interface and boom Γ_f; and uniform incoming and outgoing flows on lateral boundaries Γ_l (see, Fig. 4.2). Note that, the present method was developed for (and thus requires) domains with boundaries located at finite distance. Hence, a bottom boundary is always needed to make sure Γ is a closed boundary. If one wishes to solve for the flow under a slick in very deep water, one just has to locate the bottom boundary far enough below the slick for this boundary not to influence the flow close to the slick interface. In practical computations, we found that, when the bottom boundary was located at least ten times deeper than the boom draft, no significant influence of the bottom boundary could be found on the tangential velocity at the slick interface.

In a streamfunction representation, no-flow conditions correspond to specifying streamlines with $\overline{\psi}$ =constant. In the present case, we set $\overline{\psi} = 0$ on Γ_b and $\overline{\psi} = h\,U$ on Γ_f and uniform flow conditions correspond are specified as $\overline{\psi_n} = 0$ on Γ_l, where indices n indicates partial n-derivative.

A linearly varying streamfunction in the vertical direction should be obtained on Γ_l as the solution of Eq. (4.7), i.e., $\psi = \mid y \mid U$, provided no significant influence of the slick and boom occurs for the uniform flow. The solution on Γ_f directly provides, $U_{ws} = -\psi_n$, along the slick interface, to be used in Eqs. (4.1)-(4.4). Hence, the ideal flow solution allows one to calculate the dynamic pressure and the shear stress (provided C_f variation is known) along the slick, for any assumed slick shape.

Practical numerical solution of Eq. (4.7), with relevant boundary conditions, is done using a higher-order BEM method in which discretization nodes are specified on boundary $\Gamma = \Gamma_b + \Gamma_f + \Gamma_l$ and quadratic isoparametric elements are used to interpolate in between discretization nodes. Both regular and singular integrals in Eq. (4.7) are performed numerically, using Gauss quadrature methods for the regular integrals, and a similar method for the singular integral, well-suited to logarithmic singularities. An algebraic system of equations is thus assembled and solved for the unknowns at the discretization nodes, i.e., ψ or ψ_n, whichever is not set by boundary conditions. Details of the BEM method and numerical integrations can be found in Grilli *et al.* [18, 20, 21].

Additional difficulties arise in the numerical solution of the present problem in relation to the proper representation of BIE's for corners located at the intersection between boundaries having different types of boundary conditions and normal directions (points A, B, C, D in Fig. 4.2). To address corner problems in the BEM algorithm, double-node representations and corner compatibility equations are used (Grilli and Svendsen [21]). Within boundary Γ_f, there are also points with discontinuities in the tangential direction for which, physically, the velocity must be zero. These are the corners points E,F,G,H,I. Due to the two normal directions, double-nodes are also used to represent these points but care must be taken to ensure that the numerical solution satisfies the physical requirement of zero velocity on both sides of these points.

4.4 Iterative calculation of slick shape using a finite difference method

Non-dimensional variables are introduced in Eqs. (4.1)-(4.4), based on a length scale U^2/g, a velocity scale U, and a stress scale $\rho_w U^2$ (note that for the oil-water interface, since the oil does not move, $U = \Delta U$). We thus get,

$$x' = \frac{gx}{U^2} \quad ; \quad q' = \frac{gq}{U^2} \quad ; \quad \eta' = \frac{g\eta}{U^2} \tag{4.9}$$

$$p'_D = \frac{p_D}{\rho_w U^2} \quad ; \quad \tau'_s = \frac{\tau_s}{\frac{1}{2}\rho_w U^2} \quad ; \quad C'_f = C_f \frac{U_{ws}^2}{U^2} \tag{4.10}$$

where primes denote non-dimensional variables.

Using definitions (4.9),(4.10), Eqs. (4.1)-(4.4) transform into,

$$p'_D \;=\; \frac{1}{2}(1 - U'^2_{ws}) \tag{4.11}$$

where $U'_{ws} = U_{ws}/U$.

$$(p'_D + \eta')\,\eta_{x'} \;+\; \frac{1}{2}\tau'_s \;=\; \varphi\, q'\, q'_{x'} \tag{4.12}$$

where x' indices denote derivatives with respect to x', and $\varphi = \rho_o/\rho_w$.

$$p'_D \;+\; \eta' \;=\; \varphi\, q' \tag{4.13}$$

$$\tau'_s \;=\; C'_f \tag{4.14}$$

Combining Eqs. (4.12) to (4.14), we further get,

$$(p'_D \;+\; \eta')\left((1-\varphi)\,\eta'_{x'} \;+\; p'_{Dx'}\right) = \frac{\varphi}{2}\, C'_f \tag{4.15}$$

The set of differential equations (4.11)-(4.15) will now be transformed into Finite Difference Equations (FDE) expressed for N_{ow} nodes i along the slick interface (segment E-F in Fig. 4.2). Equation (4.15) is first developed into,

$$\eta'\,\eta'_{x'} + p'_D\,\eta'_{x'} + \frac{\eta'\,p'_{Dx'}}{1-\varphi} + \frac{p'_D\,p'_{Dx'}}{1-\varphi} = \frac{\varphi}{2(1-\varphi)}\, C'_f \tag{4.16}$$

To derive a FDE representation of Eq. (4.16), we will integrate the equation between a fictitious intermediate location defined in between points $(i-1)$ and i (i.e., point $(i-1/2)$; *central difference method*), and we will assume that values of all calculated functions, η', p'_D, and C'_f (hereafter denoted by $\mathcal{F}$) will be calculated at $(i-1/2)$ as,

$$\mathcal{F}_{i-1/2} = \frac{1}{2}\left[\,\mathcal{F}_{i-1} + \mathcal{F}_i\,\right] \tag{4.17}$$

We will also assume that, for the second and third terms in the left-hand-side and for the right-hand-side of Eq. (4.16), η', p'_D, and C'_f, respectively, are approximated by their values at point i (*upwind scheme*). Doing so, Eq. (4.16) can be transformed into,

$$\begin{aligned}&\frac{1}{2}\left(\eta_i'^2 - \frac{(\eta_i' + \eta_{i-1}')^2}{4}\right) + p'_{D_i}\left(\eta_i' - \frac{\eta_i' + \eta_{i-1}'}{2}\right) + \frac{\eta_i'}{1-\varphi}\left(p'_{D_i} - \frac{p'_{D_i} + p'_{D_{i-1}}}{2}\right)\\&+\frac{1}{2(1-\varphi)}\left(p'^2_{D_i} - \frac{(p'_{D_i} + p'_{D_{i-1}})^2}{4}\right) = \frac{\varphi}{4(1-\varphi)}\,C'_{f_i}\,(x_i' - x_{i-1}')\end{aligned} \tag{4.18}$$

Rearranging terms in Eq. (4.18), we get,

$$\begin{aligned}&\frac{3}{4}\eta_i'^2 + \eta_i'\left(\frac{(2-\varphi)p'_{D_i} - p'_{D_{i-1}}}{1-\varphi} - \frac{\eta_{i-1}'}{2}\right) = p'_{D_i}\eta_{i-1}'\\&-\frac{3p'^2_{D_i} - 2p'_{D_i}p'_{D_{i-1}} - p'^2_{D_{i-1}}}{4(1-\varphi)} + \frac{\eta'^2_{i-1}}{4} + \frac{\varphi}{2(1-\varphi)}\,C'_{f_i}\,(x_i' - x_{i-1}')\end{aligned} \tag{4.19}$$

Eq. (4.19) is a quadratic equation for predicting η_i', i.e., the slick elevation at point i, based on values of the slick elevation at point $(i-1)$, the dynamic pressure at points i and $(i-1)$ and the friction coefficient at point i. The dynamic pressure is calculated as a function of the tangential velocity of the external flow, using Eq. (4.11), and the friction coefficient similarly depends on the flow in the boundary layer close to the slick interface (see next Section for details). Thus, assuming an approximate initial shape for the slick, say $\eta_i'^o = \eta'^o(x_i')$ (e.g. as in Zalosh [42]), a first BEM solution can be calculated for the underlying flow, as explained in the previous Section, providing $\psi'^o_{n_i} = -U'^o_{ws_i}$ along the slick interface.

At stage k of the iterations, the dynamic pressure is thus found, for $(i = 1, \ldots, N_{ow})$ as,

$$p'^k_{D_i} = \frac{1}{2}(1 - \psi'^{k^2}_{no_i}) \tag{4.20}$$

and an improved slick shape $\eta_i'^{k+1}$ can be obtained by solving Eq. (4.19) for successive points $(i = 1, \ldots, N_{ow})$. A new underlying flow is then computed for the new slick interface, providing $\psi'^{k+1}_{n_i}$, and the whole process can then be repeated until convergence is reached on the slick shape between two given stages k and $k+1$, according to the criterion,

$$\mathrm{MAX}_{(i=1,\ldots,N_{ow})}\ \left|\ \frac{\eta_i'^{k+1} - \eta_i'^k}{\eta_i'^k}\ \right| \leq \epsilon \tag{4.21}$$

where ϵ is an *a priori* selected small number.

To eliminate sawtooth oscillations of the slick shape during the iterative process, it was found necessary to further transform Eq. (4.19) by replacing $\eta_i'^2$ in the left-hand-side by $\eta_i'^{k+1}\eta_i'^k$, i.e., combining the new updated values of η' at iteration $k+1$ with the old calculated values at iteration k. Furthermore, to accelerate the convergence, as soon as recalculated, $\eta_i'^k$ values are replaced by $\eta_i'^{k+1}$ values. The final equation used for the FDE iterative calculation of slick shape thus reads, for $(i = 1, ..., N_{ow})$,

$$\eta_i'^{k+1} = \frac{4(1-\varphi)p_{D_i}'^k\eta_{i-1}'^k - 3p_{D_i}'^{k^2} + 2p_{D_i}'^k p_{D_{i-1}}'^k + p_{D_{i-1}}'^{k^2} + (1-\varphi)\eta_{i-1}'^{k^2} + 2\varphi C_{f_i}'^k\,(x_i' - x_{i-1}')}{3(1-\varphi)\,\eta_i'^k + 4(2-\varphi)\,p_{D_i}'^k - 4p_{D_{i-1}}'^k - 2(1-\varphi)\,\eta_{i-1}'^k} \tag{4.22}$$

4.5 Friction coefficient calculation

According to the classical laminar Boundary Layer (BL) theory (e.g., Batchelor, 1967) applicable to smooth slender bodies like plates, the friction coefficient is a simple function of a Reynolds number **Re** based on the tangential velocity and the (arclength) distance s from the leading edge of the flow,

$$\mathbf{Re} = \frac{U_{ws}\,s}{\nu_w} \tag{4.23}$$

where ν_w denotes the water kinematic viscosity. We have,

$$C_f = \frac{0.73}{\sqrt{\mathbf{Re}}} = \varepsilon\,(U_{ws}(s)\,s)^{-1/2} \qquad \text{with } \varepsilon = 0.73\sqrt{\nu_w} \simeq 0.00073 \tag{4.24}$$

For turbulent BL's, the literature gives the following forms for C_f,

$$C_f = 0.0592\,\mathbf{Re}^{-\frac{1}{5}} \qquad \text{or} \qquad C_f = 0.027\,\mathbf{Re}^{-\frac{1}{7}} \tag{4.25}$$

Note that the latter equations do not exhibit a functional variation significantly different from Eq. (4.24).

First, assuming a very thin slick (hence $U_{ws} \simeq U$) and a small current velocity U, one can neglect dynamic effects along the slick (i.e., $U_{ws}' = 1$ and by Eq. (4.11), $p_D' = 0$). Hence, the slick shape due to pure friction can simply be found by integrating Eq. (4.16) as,

$$\eta'(x') = \left\{ \frac{\varphi}{1-\varphi} \int_0^{x'} C_f'(\xi)\,d\xi \right\}^{1/2} \tag{4.26}$$

Assuming $s \simeq x$ in Eq. (4.24), we further get,

$$\eta'(x') = \frac{\varphi}{1-\varphi}\sqrt{2\varepsilon}\,x'^{1/4} \quad \text{and} \quad \eta_{x'}'(x') = \frac{\varphi}{1-\varphi}\sqrt{\frac{\varepsilon}{8}}\,x'^{-3/4} \tag{4.27}$$

Eq. (4.27) predicts a slick shape which is both unbounded for large x' and has a vertical tangent at the leading edge ($x' = 0$).

Such results for the slick shape, however, are not realistic when compared to experiments. Furthermore, comparing the general variation of C_f given by Eq. (4.24), when $U'_{ws} = 1$, i.e. $C_f \propto s^{-1/2}$, to results calculated by Milgram and Van Houten [29] based on experiments, one can see that the true variation of C_f is much more complex along the slick, particularly in the headwave region, than predicted by this simplified (purely frictional) equation. In particular, in the experiments, C_f shows a sharp increase in front of the headwave, followed by a gradual decrease in the back of the headwave. Therefore, as concluded in [29], dynamic pressure does play an important role in determining slick shape in the headwave region. As will be shown from the computational results, U_{ws} exhibits significant variations in the headwave region and, hence, so does p'_D. This justifies using the complete iterative procedure Eqs. (4.20) -(4.22) to calculate the initial slick shape in the model, together with a representation of C_f better suited to the actual slick problem.

A more accurate prediction of C_f could be obtained by introducing a physical representation of the BL along the slick, including both laminar and turbulent regimes. This, however, would require a detailed solution of the Navier-Stokes equations in the BL, down to the scale of small geometric perturbations along the slick, together with some turbulent closure model. Due to the difficulties and uncertainties of such computations, however, at the end, one would not be guaranteed that the final values of C_f be closer to experimental values than the prediction of simple equations such as (4.24) or (4.25). Another approach is to define a semi-empirical representation of C_f along the slick, together with coefficients estimated based on experiments. The variation $C_f \propto x^{-1/2}$ obtained from above indicates that C_f should decrease from a large initial value, as x increases, and asymptotically tend to zero. This result, however, corresponds to a smooth flat boundary (like a plate), and one should expect, for a rough boundary, C_f to eventually reach a small but non-zero value, say C_{fo}, at the back of the slick. At the front of the slick, experiments show that C_f values are bounded and drop to zero at the slick leading edge. Combining these observations, the following equation is proposed for representing the variation of C_f along the slick,

$$\text{For } x \leq x_o : \quad C_f = \alpha\, x\, \exp\left(-\beta\, x^{\gamma}\right) \quad ; \quad \text{For } x \geq x_o : \quad C_f = C_{fo} \qquad (4.28)$$

where coefficients α, β, γ, and C'_{fo} should be estimated based on experiments.

In Phase II, the only experiments giving details of the slick shape that could be found were those by Milgram and Van Houten [29]. Hence, these experiments were used to estimate values of the coefficients in Eq. (4.28) leading, after iterative computations, to a final slick shape $\eta(x)$ close to the experimentally measured shape. One such case is presented in the next section. In Phase III, however, new laboratory experiments will be carried out and will be used to better calibrate the present model. A deeper physical analysis of the functional variation of C_f along the slick will also be carried out to relate the coefficients in Eq. (4.28) to flow and slick geometry characteristics.

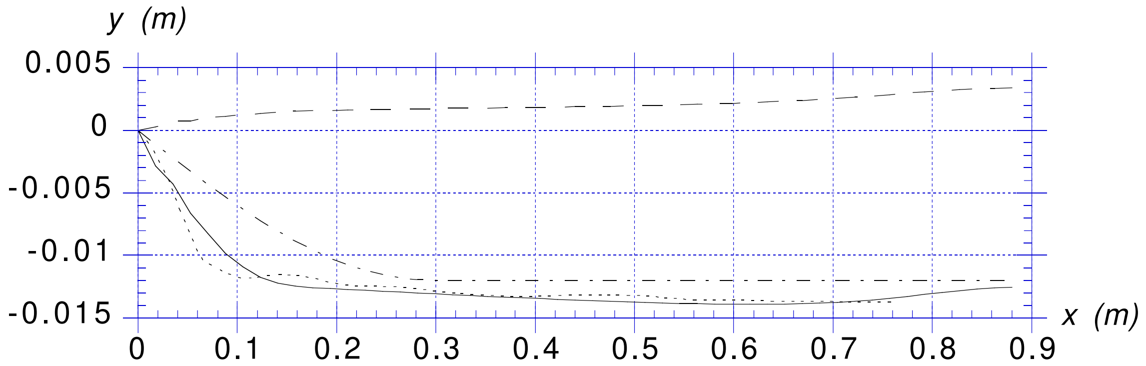

Figure 4.3: Computation of the quasi-steady shape of an oil slick with the BEM/FDE iterative method. The water density is $\rho_1 = 1000$ kg/m^3, the oil density ratio is $\varphi = 0.88$ and the current upstream velocity is $U = 0.17$ m/s. The friction coefficient is empirically modeled by Eq. (4.28), with $\alpha = 1.259$, $\beta = 250.0$, $\gamma = 2.5$, and $C_{fo} = 0.005$, for $x_o \simeq 0.18$ m. The boom draft is $d = 0.175$ m, the boom width is $w = 0.03$ m, the water depth is $h = 0.53$ m and the slick length is $l = 0.88$ m. The slick interface E-F was discretized in both the BEM and the FDE using $N_{ow} = 51$ nodes with initial uniform density. Convergence was reached after 150 iterations for $\epsilon = 10^{-8}$. Results show the interface $\eta(x)$: (— - —) initial shape based on Zalosh [42]; (———) final calculated shape; and (- - - - -) experimental shape measured by Milgram and Van Houten [29]. Results also show the free surface shape (– – – –) $q(x) - \eta(x)$.

4.6 Numerical results

Milgram and Van Houten [29] reported laboratory experiments for the geometry of slick contained by booms subjected to water currents of different intensity U (Fig. 4.2). Measuring the slick shape and using equations (4.1)-(4.4), they calculated the variation of the friction coefficient $C_f(x)$ along the slick.

In the present application, in order to validate the BEM/FDE procedure developed for iteratively calculating the initial quasi-steady shape of contained a oil slick, we selected a case in Milgram and Van Houten's experiments for which the current velocity was just slightly super-critical and the slick interface geometry was quite smooth. Unfortunately, no result for lower velocities were reported in their study. Using Eq. (4.28) together with the iterative procedure Eqs. (4.20)-(4.22), we then estimated the best values of coefficients α, β, γ, and C_{fo}, that led to a slick shape close to the measured one.

Physical parameters for the selected case were : the water density $\rho_1 = 1000$ kg/m^3, the oil density ratio $\varphi = 0.88$, and the current upstream velocity is $U = 0.17$ m/s. For these values, using the standard value of the interfacial tension, the linear analysis reported above (Eqs. (2.33) and (2.34)) leads to a critical wavelength of instability $\lambda^{min} = 0.028$ m and a corresponding critical velocity $U_{cr}^{min} = 0.15$ m/s. Hence, in this case, the KH instability on the slick interface should start developing at a very slow growth rate. The laboratory experiments were conducted with a boom draft $d = 0.175$ m, a boom width $w = 0.03$ m, a

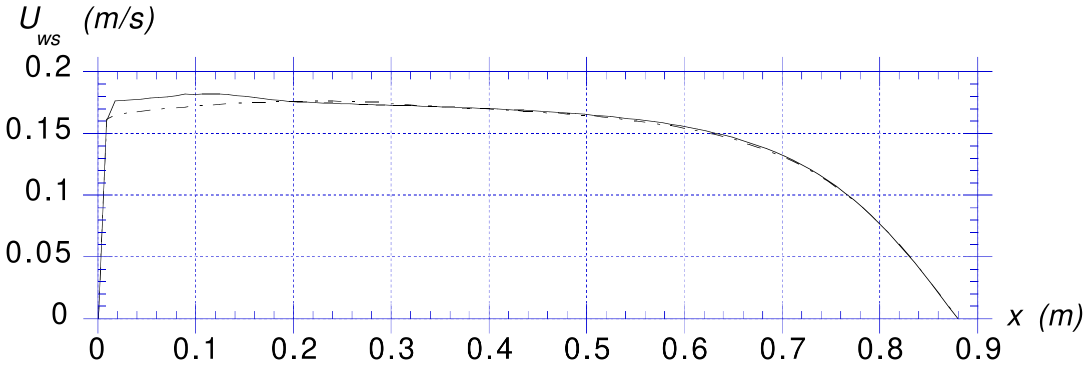

Figure 4.4: Same computations as in Fig. 4.3. Results show the interface tangential velocity $U_{ws}(x)$ computed with the BEM method for : (— - —) the initial shape based on Zalosh [42]; (———) the final calculated shape.

water depth $h = 0.53$ m, and a slick length $l \simeq 0.88$ m.

These dimensions and the above physical parameters were closely reproduced in the present computations. In the BEM/FDE procedure, $N_{ow} = 51$ nodes with initial uniform density were defined along the slick interface E-F (Fig. 4.2). In the BEM calculations, more nodes were used along the rest of the boundary and quadratic isoparametric elements were used for the interpolation. The initial slick shape $\eta^o(x)$ was selected following a method similar to Zalosh's and is given in Fig. 4.3.

Many different computations were performed in order to calculate the best values of the coefficients in Eq. (4.28). The final values found for these coefficients were : $\alpha = 1.259$, $\beta = 250.0$, $\gamma = 2.5$, and $C_{fo} = 0.005$. [Note that the location x_o was simply selected such that C_f take the value C_{fo} in the first part of Eq. (4.28); this led to $x_o \simeq 0.18$ m.] For an accuracy $\epsilon = 10^{-8}$, the final BEM/FDE run converged after 150 iterations. The converged slick shape is given in Fig. 4.3, as compared to the experiments. With the selected coefficients, the overall agreement between experiments and computations is quite good, although the experimental slick shape exhibits small fluctuations, particularly in the headwave region, likely indicating the initiation of an instability. Note the low value $C_f = C_{fo}$ in the back of the slick, indicating that friction is quite small and thus confirming that the interface shape is very smooth in this region. Experimental results were not available close to the boom. In the computations, however, due to the stagnation point for the flow at the boom, leading to a zero tangential velocity, friction along the interface gradually drops to zero and the dynamic pressure increases, which leads to a reduction of the slick thickness at the boom. As a further indication of this, Fig. 4.4 gives the variation of the tangential velocity computed along the slick and one can see that the largest differences between velocities calculated for the first and last iterations occur in the headwave region, for $x < x_o$. Finally, as a result of the quasi-hydrostatic force balance within the slick, the free surface location $[q(x) - \eta(x)]$, calculated by Eqs. (4.3) or (4.13), gradually raises up from the slick leading edge to the boom (see Fig. 4.3).

Chapter 5

Effects of interfacial friction on vorticity updating equation

5.1 Introduction

In the inviscid VS models presented in Chapters 2 and 3 (i.e., PCVS and CVS models), the interface between two fluids of density (ρ_o, ρ_1) and velocity (u_o, u_1) was treated as a continuous thin layer separating two potential flows, and the entire vorticity originated from the velocity jump $\mid u_o - u_1 \mid$ across this interface was concentrated within the thin region in vortex sheet (Fig. 5.1).

In the models, the equations used to derive the vorticity updating Eq. (2.7), assumed that the interface itself satisfied both kinematic and dynamic conditions, the former representing the compatibility of motions of the sheet with respect to each fluid and the latter expressed as a pressure equilibrium on both sides of the interface/VS (i.e., in each ideal fluid), with correction for the interfacial tension induced pressure jump. Thus, all external forces and flow parameters, such as velocity, buoyancy, density difference, and surface tension, were expressed in terms of circulation change on the right-hand side of Eq. (2.7).

Experimental observations, however, show that interfacial friction plays a key role in determining the quasi-static geometry of the interface and its time evolution (e.g., Milgram and Van Houten [29]), especially in the headwave region. In Chapter 4, we presented a method to calculate the initial quasi-steady state shape of a contained oil slick, that includes friction effects. To correctly study the time evolution of such an interface, it is thus necessary to also include friction effects in the vorticity updating Eq. (2.7).

In the present Chapter, we show how this can be done. Actual implementation, test, and use of the new equation, however, will take place during Phase III studies.

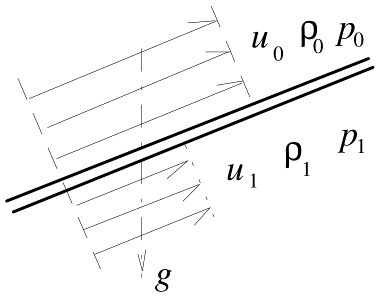

Figure 5.1: Sketch of inviscid interface/VS equilibrium

5.2 Governing equations

Friction will affect the balance of forces at the interface/VS. In our model, friction effects will be represented by equivalent tangential interfacial shear stresses (τ_o, τ_1), acting in the fluids on either side of the interface. Combined to pressures (p_o, p_1), these stresses will have to satisfy the dynamic equilibrium equation at the interface.

Following classical Boundary Layer (BL) theory, friction will be assumed to be important only in two small regions (i.e. BL's), on either side of the interface, in which viscosity dominates and velocity profiles have smooth tapered transitions. Outside of these BL regions, the fluids will still be assumed to behave as inviscid irrotational fluids. This is sketched in Fig. 5.2, where the velocity diagrams have been tapered in (thicker) BL regions on both sides of the thin interface. In these two BL's vorticity diffusion is assumed to occur in the normal direction across the interface and vorticity convection to occur in the tangential direction, both contributing to the equivalent shear stresses (τ_o, τ_1) acting on each side of the interface.

Note that friction becomes an external force acting on the interface only when a velocity jump still occurs at the interface, as sketched in Fig. 5.2, and the potential flows in fluids 0 and 1 are kept slightly away from the interface by the BL's thickness. Taking control volume elements on both sides of the interface (Zalosh [43], Rottman and Olfe [36], Grilli *et al.* [16, 17]), the rate of change of circulation on the VS can be derived under the combined action of gravity, surface tension, and friction effects at the interface between two fluids. This will first be done for a vortex sheet represented by piecewise constant vorticity elements.

Taking the material time derivative of equation (2.5), in which circulation is defined as a function of the tangential velocity jump at the VS, we get, for a VS element of length Δs_i over which velocity is assumed constant and the geometry to be smoothly varying,

$$\frac{D\,\Gamma}{D\,t}(s_i) \equiv \frac{D\,\Gamma_i}{D\,t} = \int_{s_i-\Delta s_i/2}^{s_i+\Delta s_i/2} \left(\frac{D\,u_{os}}{D\,t} - \frac{D\,u_{1s}}{D\,t} \right) ds \simeq \left(\frac{D\,u_{os}}{D\,t} - \frac{D\,u_{1s}}{D\,t} \right)_i \Delta s_i \qquad (5.1)$$

For Newtonian fluids, tangential accelerations in (5.1) can be expressed, for both fluids

0 and 1, using Navier-Stokes' equations as,

$$\frac{D\,\boldsymbol{u}_{o,1}}{D\,t} = -\frac{1}{\rho_{o,1}}\boldsymbol{\nabla} p_{o,1} \;-\; g\boldsymbol{\nabla} y + \frac{1}{\rho_{o,1}}\boldsymbol{\nabla}\cdot\left(\mu_{o,1}\boldsymbol{\nabla}\boldsymbol{u}_{o,1}\right) \tag{5.2}$$

in which p is the fluid pressure (discontinuous across the interface due to surface tension), g is the acceleration of gravity (vertical pointing in the downward y direction), and μ denotes the dynamic molecular velocity, with the last term in parenthesis representing the fluid stress tensor.

Taking the dot product of Eq. (5.2) with the tangential vector $\boldsymbol{s}$ (defined as in Eq. (2.4)), we get,

$$\frac{D\,u_{os,1s}}{D\,t} = -\frac{1}{\rho_{o,1}}\frac{\partial p_{o,1}}{\partial s} \;-\; g\sin\beta + \frac{1}{\rho_{o,1}}\boldsymbol{\nabla}\cdot\left(\mu\boldsymbol{\nabla} u_{os,1s}\right) \tag{5.3}$$

Now, in the BL's on both sides of the VS (sketched in Fig. 5.2), we assume velocity changes in the normal direction to be dominant over changes in the tangential direction. Hence, defining the Newtonian interfacial shear stresses as,

$$\tau_{os,1s} = -\mu_{o,1}\frac{\partial u_{os,1s}}{\partial n} \tag{5.4}$$

with n denoting the normal direction at the interface pointing outside of each fluid region, we get,

$$\frac{D\,u_{os,1s}}{D\,t} \simeq -\frac{1}{\rho_{o,1}}\frac{\partial p_{o,1}}{\partial s} \;-\; g\sin\beta - \frac{1}{\rho_{o,1}}\frac{\partial \tau_{os,1s}}{\partial n} \tag{5.5}$$

The normal gradients of shear stresses at the interface in Eq. (5.5) will be approximated using equivalent interfacial shear stresses defined, within each BL region, with opposite directions on each side of the interface (Fig. 5.2) as,

$$\tau_{o,1} = \mp h_{o,1}\,\frac{\partial \tau_{os,1s}}{\partial n} \tag{5.6}$$

where h_o and h_1 denote vorticity diffusion thicknesses. [Note that this corresponds to assuming shear stresses go to zero at distances $h_{o,1}$ on either side of the interface.] We thus get,

$$\frac{D\,u_{os,1s}}{D\,t} \simeq -\frac{1}{\rho_{o,1}}\frac{\partial p_{o,1}}{\partial s} \;-\; g\sin\beta \pm \frac{\tau_{o,1}}{\rho_{o,1}\,h_{o,1}} \tag{5.7}$$

Replacing tangential accelerations from Eq. (5.7) into Eq. (5.1), we get,

$$\frac{D\,\Gamma_i}{D\,t} = \left(\frac{1}{\rho_1}\frac{\partial p_1}{\partial s} - \frac{1}{\rho_o}\frac{\partial p_o}{\partial s} + \frac{\tau_o}{\rho_o\,h_o} + \frac{\tau_1}{\rho_1 h_1}\right)_i \Delta s_i \tag{5.8}$$

From the definition of the *sheet velocity*, $\boldsymbol{u}$, the tangential acceleration following the vortex sheet motion is obtained as,

$$\frac{du_{si}}{dt} = \frac{1}{2}\left(\frac{du_{os}}{dt} + \frac{du_{1s}}{dt}\right)_i \tag{5.9}$$

with, according to the definitions of different material derivatives,

$$\frac{d}{dt} = \frac{D}{Dt} \pm \frac{1}{2}(\boldsymbol{u}_o - \boldsymbol{u}_1) \cdot \boldsymbol{\nabla} \tag{5.10}$$

with the plus sign being taken in fluid 1 and the minus sign in fluid 0. Replacing Eq. (5.10) in (5.9), we get,

$$\frac{du_{si}}{dt} = \frac{1}{2}(\frac{D\,u_{os}}{D\,t} + \frac{D\,u_{1s}}{D\,t})_i - \frac{1}{4}(u_{os} - u_{1s})_i\,(\frac{\partial u_{os}}{\partial s} - \frac{\partial u_{1s}}{\partial s})_i \tag{5.11}$$

Using Navier-Stokes equations (5.7) to express tangential velocities and Eq. (2.3) to express the vortex sheet strength, we get,

$$\frac{du_{si}}{dt} = -\frac{1}{2}(\frac{1}{\rho_o}\frac{\partial p_o}{\partial s} + \frac{1}{\rho_1}\frac{\partial p_1}{\partial s} + 2g\,\sin\beta + \frac{\tau_1}{\rho_1 h_1} - \frac{\tau_o}{\rho_o h_o})_i - \frac{1}{4}\gamma_i\frac{\partial \gamma_i}{\partial s} \tag{5.12}$$

From the expression of surface tension effects at the interface between two fluids (Batchelor, 1967), the pressure jump across the vortex sheet is given by,

$$p_o - p_1 = \sigma_{o1}\frac{1}{\mathcal{R}} \tag{5.13}$$

in which $1/\mathcal{R}(s)$ is the sheet curvature. In curvilinear coordinates, it can easily be shown that the curvature is identical to, $\partial\beta/\partial s$. Hence, taking the tangential derivative of (5.13), we get,

$$\frac{\partial p_o}{\partial s} - \frac{\partial p_1}{\partial s} = \sigma_{o1}\frac{\partial^2 \beta}{\partial s^2} \tag{5.14}$$

Eliminating the pressure between equations (5.8),(5.12), and (5.14), we finally get the rate of change of circulation at point s_i of the sheet as,

$$\begin{aligned}\frac{D\,\Gamma_i}{D\,t} &= 2\Delta s_i\left(\kappa\,[\frac{du_{si}}{dt} + g\,\sin\beta_i + \frac{1}{4}\gamma_i\frac{\partial\gamma_i}{\partial s} + \frac{1}{\rho_1(1-\varphi)}(\frac{\tau_{oi}}{h_o} + \frac{\tau_{1i}}{h_1})]\right.\\ &\quad \left. - \frac{\sigma'_{o1}}{1+\varphi}\frac{\partial^2\beta_i}{\partial s^2}\right)\end{aligned} \tag{5.15}$$

where $\sigma'_{o1} = \sigma_{o1}/\rho_1$, $\varphi = \rho_o/\rho_1 \leq 1$, $\kappa = (1-\varphi)/(1+\varphi)$ is the Atwood number and, by (2.4),

$$\frac{du_{si}}{dt} = \frac{du_i}{dt}\cos\beta_i + \frac{dv_i}{dt}\sin\beta_i \tag{5.16}$$

is the tangential acceleration at point i.

Various approaches can be pursued to model the interfacial shear stresses in Eq. (5.15) as a function of the flow kinematics and, ultimately, of the circulation on the VS. Laminar or turbulent BL theories, for instance, can provide a representation of shear stresses based on a combination of diffusion and convection in the BL's. The simplest global approach, however, consists in representing the turbulent shear stresses using a semi-empirical friction coefficient, on a way similar to Eq. (4.4). In the present case, this method would give,

$$\tau_{o,1} = \frac{1}{2}\rho_{o,1}\, C_{fo,f1}\,(u_{os,1s} - u_s)\ \mid u_{os,1s} - u_s \mid \tag{5.17}$$

in which the relative velocity between the tangential flow velocity in each fluid $u_{os,1s}$ and the VS's tangential velocity u_s has been used. Using the definition of the VS's velocity u_s and Eq. (2.3), Eq. (5.17), for vortex element i, transforms into,

$$\tau_{oi,1i} = \pm\frac{1}{2}\rho_{o,1}\, C_{fo,f1}\,\gamma_i^2 \tag{5.18}$$

Now, with the above definition, the *effect of interfacial friction* on the rate of change of vorticity in Eq. (5.15) reads,

$$\frac{1}{\rho_1(1-\varphi)}\,(\frac{\tau_{1i}}{h_1} + \frac{\tau_{oi}}{h_o}) = \frac{1}{8\,(1-\varphi)}\,\gamma_i^2\,(\varphi\frac{C_{fo}}{h_o} - \frac{C_{f1}}{h_1}\,) \tag{5.19}$$

Hence, the final equation for the rate of change of vorticity reads,

$$\begin{aligned}\frac{D\,\Gamma_i}{D\,t} \;&=\; 2\Delta s_i \left(\kappa\,[\,\frac{du_{si}}{dt} \,+\, g\,\sin\beta_i \,+\, \frac{1}{4}\gamma_i\frac{\partial\gamma_i}{\partial s} \,+\, C_f\,\gamma_i^2\,]\right.\\ &\left.\quad -\,\frac{\sigma'_{o1}}{1+\varphi}\,\frac{\partial^2\beta_i}{\partial s^2}\right)\end{aligned} \tag{5.20}$$

in which we have defined as,

$$C_f = \frac{1}{8\,(1-\varphi)}\,(\varphi\frac{C_{fo}}{h_o} - \frac{C_{f1}}{h_1}\,) \tag{5.21}$$

the global friction coefficient between fluid 0 and 1 at the VS interface.

During Phase III studies, this and other models of representation of friction at the oil-water interface will be developed, validated, and tested. In particular, using newly obtained experimental data, computations with the model will be calibrated to represent experimental measurements at best, for the geometry of a contained oil-slick as a function of time. Such calibrations will take place through the semi-empirical representation of the friction coefficient C_f along the oil-water interface (see also Chapter 4 for more discussions on this subject).

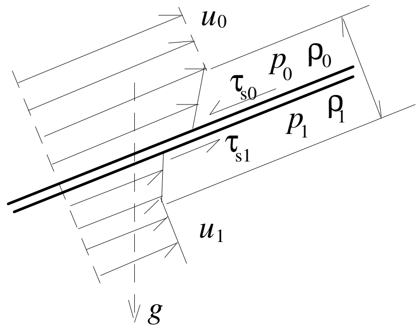

Figure 5.2: Sketch of interface/VS equilibrium including friction effects

Chapter 6

Conclusions

Following initial studies and model developments reported for Phase I studies (Grilli *et al.* [16]), model developments in Phase II studies have focused on three major aspects : (i) improving and complementing the models developed in Phase I, namely both periodic and non-periodic Piecewise Constant Vortex Sheet (PCVS) models (Chapter 2); (ii) provide a better representation of hydrodynamic instabilities in the oil containment problem by developing and implementing a more accurate model based on Continuous Vortex Sheets (CVS) (Chapter 3); and (iii) both implementing and validating a numerical method for calculating the quasi-steady equilibrium shape of an oil-slick including the effects of interfacial friction (Chapter 4), and developing a formalism to include interfacial friction effects in the Vortex Sheets (VS) time updating equations (which were ignored in Phase I model) (Chapter 5).

As a result of such model development/improvements, model applications carried out during Phase II provided more quantitative analyses and predictions than the qualitative descriptions of the oil containment behavior achieved during Phase I.

More specifically, in Chapter 2, we presented the development/improvements of PCVS periodic and non-periodic models and their application to *periodic KH instability* and *oil containment by a boom*, respectively. Figs. 2.9-2.12, for instance, show the quantitative influence of interfacial velocity jump ΔU, gravity g, fluid density ratio φ, and surface tension coefficient σ_{o1}, on the growth rate of *KH interfacial instability*, as computed with the periodic PCVS model. Throughout these computations, the improved Phase II periodic PCVS model performed very well and was thus validated as a tool for predicting interfacial behavior during KH instability. More specifically, using the PCVS model, it was found,

(i) in the presence of gravity, the interface is subjected to stabilizing effects from buoyancy forces and the disturbance growth is slowed as compared to an identical case when gravity effects are not included;

(ii) an increase in fluid density difference across the interface will result in reducing and slowing down the disturbance growth on the interface; the most unstable case is thus a case with two identical fluids ($\varphi = 1$) or, in the present case, the heavier oil;

(iii) and an increase in surface tension at the interface also results in reducing and slowing down the disturbance growth on the interface; this is because surface tension, to some extent, balances the circulation accumulation in the highly curved regions of the interface.

Based on the result in (ii), one can thus postulate that, for an oil slick contained by a boom, the headwave instability growth rate will be smaller and the instability will be delayed when using a lighter oil, compared to the case of a heavier (or weathered) oil. In laboratory experiments with oil/boom systems, it is observed that the oil-water interface, at first, rolls-up in the headwave region before pieces of the interface are torn off (e.g., Delvigne [9]). Therefore, based on the results in (iii), it is theoretically expected that, if surface tension is naturally (e.g., through weathering) or artificially (e.g., through chemicals) increased, the disturbance growth on the interface will be reduced and the interface break up and resulting containment failure will be accordingly delayed (or eliminated), hence, providing additional time for collecting oil at a given (unstable) relative velocity.

In the light of the above results, in subsequent studies, particularly during Phase III, the quantitative influence of density difference and surface tension on the oil-water interface evolution, will be studied for complete oil-boom systems. Along this line, Figs. 2.13, 2.14, and 2.15, for instance, showed computational results of the non-periodic PCVS model for the *entrainment and critical accumulation* failure modes of contained oil slicks. Despite their realism, at this stage, however, such results only show the ability of the PCVS model to capture the underlying physics and predict the unstable shape of a contained oil slick. Indeed, these results still use the empirical method by Zalosh [42] to estimate the *initial shape* of the slick, and also do not include *interfacial friction* effects which have an important influence on slick geometry and thickness. After integrating in this model the initialization of the slick shape, presented in Chapter 4, and the inclusion of frictional effects in the vorticity updating equation, presented in Chapter 5, more quantitatively realistic similar computations will be performed during Phase III, using the more accurate CVS model, presented in Chapter 3 for the velocity calculations. Model parameters will then be calibrated based on newly obtained experimental data.

In Chapter 3, we presented the development, validation, and application of a *new CVS model*. By contrast with the PCVS model, in order to achieve better accuracy and stability, this model uses higher-order spatial discretizations (cubic) for both the geometry and the computational fields along the oil-water interface. As a result, integrals in Biot-Savart equations (2.1) must be calculated numerically. This required the development of accurate integration methods for hypersingular integrals. Looking at Fig. 3.3, for instance, it can be seen that, with the CVS model, the periodic Kelvin-Helmholtz instability at an oil-water interface and the subsequent roll-up of Vortex Sheets were very accurately modeled, and for a much longer time, than when using the PCVS model. Validation cases for a simple uniform flow also showed that the CVS model provides much more accurate results for the velocities than the PCVS model, particularly for domain geometries with very high aspect ratio (as in containment of oil by a boom). This, hence, justifies the development of the CVS model. This model will be more extensively used during Phase III studies.

In Chapter 4, we presented a model and applications for calculating the *quasi-steady-*

state initial shape of a contained oil slick. Quasi-hydrostatic equilibrium was assumed in the oil slick and the external water flow velocity was computed for a specified geometry of the oil-water interface. An iterative method was used to calculate the interface shape satisfying interfacial equilibrium equations. The interfacial friction coefficient C_f was semi-empirically modeled. Looking at Fig. 4.3, for instance, it can be seen that the initial stable shape of an oil slick, measured by Milgram and Van Houten [29] in their laboratory experiments, was correctly recalculated using the PCVS model. This model will be used during Phase III studies to calculate the initial stable shape of contained oil slicks, for low tow velocities, which will then be used to initialize the VS model(s) calculating the interfacial instabilities and slick containment failures occurring for larger tow velocities.

Finally, in Chapter 5, we developed modified vorticity updating equations (5.20) and (5.21), including the effects of interfacial friction. These equations will be implemented and tested during Phase III studies in order to more accurately and quantitatively calculate the containment failure of an oil slick, whose shape will have been initialized using the model developed in Chapter 4.

Bibliography

[1] Agrawal, R.K. and Hale, L.A. 'A new criteria for predicting head wave instability of an oil slick by a barrier', *Proc. Offshore Tech. Conf.,* Dallas, Texas, pps. 461-466, 1974.

[2] Bai, K.J. and Kim, J.W. 'A computational model for flow around an oil boom', *Proc. Workshop on Tidal and Oil Spill Modeling,* 5-17, 1993.

[3] Baker, G.R. and M.J., Shelley 'On the connection between thin vortex layers and vortex sheets.' *J. Fluid Mech.*, **215**, 161-194, 1990.

[4] Batchelor, G. K., *An introduction to fluid dynamics* Cambridge University Press, 1967.

[5] Benjamin, T.B. 'Gravity currents and related phenomena', *J. Fluid Mech.,* **31** (2), 209-248, 1968.

[6] Brebbia, C.A., *The Boundary Elements for Engineers* John Wiley and Sons, 1978.

[7] Clavelle, E.J. and Rowe, R.D. 'Numerical simulation of oil–boom failure by critical accumulation', *Arctic Marine Oil Spill Prog. Tech. Seminar,* 409-418, 1993.

[8] Cross, R.H. and Hoult, D.P. 'Oil booms in tidal currents', *J. Waterways, Port. Coastal Ocean Engng.,* **98**, 1745-1758, 1972.

[9] Delvigne, G.A.L. 'Barrier failure by critical accumulation of viscous oil', *Proc. Oil Spill Conf.,* USEPA, USCG, and Amer. Petrol. Inst., pps. 143-148, 1989.

[10] Di Pietro, N. D. and Cox, R. G. 'The containment of an oil slick by a boom placed across a uniform stream', *J. Fluid Mech.,* **96,** 613-640, 1980.

[11] Drazin, P.G. 'Kelvin-Helmholtz instability of finite amplitude', *J. Fluid Mech.,* **42,** 321-335, 1970.

[12] Drazin, P.G. and Howard, L.N. 'Hydrodynamic stability of parallel flow of inviscid fluid', *Advanc. Applied Mech.,* **9,** 1, 1966.

[13] Ertekin, R.C. and Sundararaghavan, H. 'The calculation of the instability criterion for a uniform viscous flow past a boom', *J. Offshore Mech. Artic Engng.,* **117,** 24-29, 1995.

[14] Fink, P.T. and Soh, W.K. 'Calculation of vortex sheets in unsteady flow and application in ship hydrodynamics', *Proc. 10th Symp. on Naval Hydrodynamics,* Office of Naval Res., Washington, D.C., 463-491, 1974.

[15] Guiggiani, M., Krishnasamy, G., Rudolphi, T.J., and F.J. Rizzo 'A general algorithm for the numerical solution of hypersingular boundary integral equations.' *Trans. ASME*, **59**, 604-614, 1992.

[16] Grilli, S.T., Hu, Z., and Spaulding, M.L. 'A hydrodynamic model of oil containment by a boom : Phase I', *Final Technical Report for DOT Grant No. DTRS57-94-G-00076*, Dept. Ocean Engng., Univ. of Rhode Island, 70pps, 1996.

[17] Grilli, S.T., Hu, Z., and Spaulding, M.L. 'Numerical modeling of oil containment by a boom', *Proc. 19th Arctic and Marine Oilspill Program Technical Seminar* (AMOP), 6/96, Calgary, Alberta, Canada, pps. 343-376. Environment Canada, 1996.

[18] Grilli, S.T. and Subramanya, R. 'Recent advances in the BEM modelling of nonlinear water waves'. Chapter 4 in *Boundary Element Applications in Fluid Mechanics* (ed. H. Power), pps. 91-122. Advances in Fluid Mechanics Series. Computational Mechanics Publication, Southampton, UK, 1995.

[19] Grilli, S.T. and Subramanya, R. 'Quasi-singular Integrations in the Modelling of Nonlinear Water Waves.' *Engng. Analys. with Boundary Elements,* **13**(2), 181-191, 1994.

[20] Grilli, S.T. and Subramanya, R. 'Numerical modeling of wave breaking induced by fixed or moving boundaries.' *Computational Mechanics* **17**(6), 374-391, 1996.

[21] Grilli, S.T. and I.A., Svendsen 'Corner Problems and Global Accuracy in the Boundary Element Solution of Nonlinear Wave Flows.' *Engng. Analys. with Boundary Elements*, **7**(4), 178-195, 1990.

[22] Johnston, A.J., Fitzmaurice, M.R. and Watt, R.G. 'Oil spill containment : viscous oils', *Proc. Oil Spill Conf. (USEPA, USCG),* Amer. Petrol. Inst., pps. 89-94, 1993.

[23] Jones, W. T. 'Instability at an interface between oil and flowing water', *J. of Basic Engng.,* **94,** 874-878, 1972.

[24] Krasny, R. 'A study of singularity formation in a vortex sheet by the point-vortex approximation.' *J. Fluid Mech.*, **167**, 65-93, 1986.

[25] Kelvin, Lord *Mathematical and Physical Papers* **4** 76-100, Cambridge University Press, 6th edition, 1910.

[26] Lamb, H. *Hydrodynamics* Cambridge University Press, 6th edition, 1932.

[27] Lau, Y.L. and Kirchifer, S.A. 'A review of the dynamics of contained oil slicks in flowing water', *J. Hydraulics Div.,* 1974.

[28] Leibovich, S. 'Oil slick instability and the entrainment failure of oil containment booms', *J. Fluids Engng.,* **98,** 98-105, 1976.

[29] Milgram, J.H. and Van Houten, R.J. 'Mechanics of a restrained layer of floating oil above a water current', *J. Hydronautics,* **12** (3), 93-108, 1978.

[30] Meiron, D.I., Baker, G.R., and S.A. Orszag 'Analytic structure of vortex sheet dynamics. Part 1. Kelvin-Helmholtz Instability.' *J. Fluid Mech.*, **114**, 283-298, 1982.

[31] Moore, D.W. 'A numerical study of the roll-up of a finite vortex sheet.' *J. Fluid Mech.*, **63**(2), 225-235, 1974.

[32] Moore, D.W. 'The spontaneous appearance of a singularity in the shape of an evolving vortex sheet.' *Proc. Roy. Soc. London*, **A365**, 105, 1979.

[33] Rangel, R.H. and Sirignano, W.A. 'Nonlinear growth of Kelvin-Helmholtz instability : Effect of surface tension and density ratio', *Phys. of Fluids,* **31** (7),1845-1855, 1988.

[34] Rangel, R.H. and Sirignano, W.A. 'The linear and nonlinear shear instability of a fluid sheet', *Phys. of Fluids.* **A3** (10), 2392-2400, 1991.

[35] Rosenhead, L. 'The formation of vortices from a surface of discontinuity.' *Proc. Roy. Soc. London*, **A134**, 170-192, 1931.

[36] Rottman, J. W. and Olfe, D.B. 'Comment on "discretized simulation of vortex sheet evolution with buoyancy and surface tension effects" ', *J. AIAA* **15**, 1214-1215, 1977.

[37] Van de Vooren, A.I. 'Numerical investigation of the rolling-up of vortex sheets', *Proc. R. Soc. Lond.,* **A 373**, 67-91, 1980.

[38] Von Karman T., 'The engineer grapples in the nonlinear problems', *Bull. Am. Math. Soc.* **46**, 615-586, 1940.

[39] Wicks, M. 'Fluid dynamics of floating oil containment by mechanical barriers in the presence of water currents', *Proc. API-FWPCA Joint Conf. on Prevention and Control of Oil Spills,* New York, Dec 15-17, Amer. Petrol. Inst., pps. 55-106, 1969.

[40] Wilkinson, D. L. 'Dynamics of contained oil slicks', *J. Hydraulics Div.,* **98,** 1013-1031, 1972.

[41] Wilkinson, D. L. 'Limitations to length of contained oil slicks', *J. Hydraulic Div.,* **99,** 701-713, 1973.

[42] Zalosh, R.G. 'A numerical model of droplet entrainment from a contained oil slick', *Report No.* **CG-D-65-75**, DOT/USCG, 1974.

[43] Zalosh, R.G. 'Discretized simulation of vortex sheet evolution with buoyancy and surface tension effects', *J. AIAA,* **14**, 1517-1523, 1976.

[44] Zalosh, R.G. and Jensen, D.S. 'A numerical model of droplet entrainment from a contained oil slick', *Proc. Fluid Mech. in Petrol. Indus.,* ASME, 17-27, 1975.

[45] Zaroodny, S.J. and Greenberg, M.D. 'On a vortex sheet approach to the numerical calculation of water waves', *J. Comp. Phys.,* **11**, 440-446, 1973.